UNIVERSITY OF CALIFORNIA, SAN DIEGO

Development of Microscopy Ambient Ionization Top-down Mass Spectrometry

A dissertation submitted in partial satisfaction of the requirements for the degree Doctor of Philosophy

in

Chemistry

by

Cheng-Chih Hsu

Committee in charge:

Professor Pieter C. Dorrestein, Chair
Professor Michael Galperin
Professor Eduardo R. Macagno
Professor Ulrich F. Müller
Professor Amitabha Sinha

2014

The dissertation of Cheng-Chih Hsu is approved, and it is acceptable in quality and form for publication on microfilm and electronically:

Chair

University of California, San Diego

2014

TABLE OF CONTENTS

LIST OF FIGURES

LIST OF TABLES

ACKNOWLEDGEMENTS

I would like to acknowledge those individuals without whom this thesis is not possible.

First and foremost, I would like to express my sincere gratitude to my committee chair, Prof. Pieter C. Dorrestein, for his support and advisory over the course of my doctoral research. I particular thank him for leading me to the world of mass spectrometry. I would also like to thank Michael J. Meehan, Jeramie D. Watrous, Vanessa V. Phelan, Laura M. Sanchez, Theodore Alexander, Don D. Nguyen, Yao Peng, Yi J. Zeng, Jinshu J. Fang, Samantha J. Mascuch, Wilna Moree, Wei-Ting Liu, Yu-Liang Yang, Kathleen Dorrestein, and all the other Dorrestein group members past and present for a wonderful teamwork. It has been a great pleasure and an honor working with them.

Next I would like to thank all my committee members, Prof. Macagno, Prof. Sinha, Prof. Galperin, and Prof. Müller for their time and wisdom.

I must thank Prof. Eduardo R. Macagno, whose contributions were critical to the success of the microscopy ambient mass spectrometry project. I sincerely thank Prof. Sameul L. Pfaff, Nicolas M. White, Tiffany Poon, and Marito Hayashi for great collaboration on preparation of embryo sections which are essential to the project, Prof. Ju Chen and Indroneal Banerjee for the materials from gene knockout mice, my roommate Eugene C. Lin for computational input. Without their support my scientific findings would have not progressed to a level suitable for a doctorate degree.

I also thank Mariam S. ElNaggar for her technical supports, and Maria Månsson, Amalie Møller, Xueting Liu, Robert A. Quinn and all the other collaborators in real-time microbial metabolomics project, for their efforts in microbial collections from every

corner of the world. I also appreciate the collaborations in the project of white-nose syndrome. I am grateful to Prof. Forest Rohwer, Jeremy Barr, Michael Baker, and Terry Gaasterland for providing samples and insightful comments. Also I appreciate experimental helps from Brendan M. Duggan. My special thank is to Prof. Michael J. Tauber and Prof. Judy E. Kim for their indispensable advices.

I am also grateful to all of the agencies that contributed funding towards this work. I was supported by National Institutes of Health Grant GM094802.

I could not express more gratitude to my dearest partner, Chih-Chiao Lai, for her unconditional support and encouragement along the way. Without Chih-Chiao's efforts on taking care of the family and our little daughter Zoey Hsu, I would have not been here.

I honestly thank all my friends especially Li-Chih Hu, Liang-Yan Hsu, Chen Wang, Wei Lin, Eugene Lin, Wei-Ting Liu and many others for continuing support.

Chapter 1 is a modified reprint of the material as it appears in the manuscript of the perspective article invited for publication in Current Opinion in Biotechnology: Analytical Biotechnology 2014 by Cheng-Chih Hsu and Pieter C. Dorrestein. The thesis author is the primary author of the article.

Chapter 2 is a full reprint of the material as it appears in the published article of PNAS 2013, vol. 110, pp.14855-14860 by Cheng-Chih Hsu, Nicolas M. White, Marito Hayashi, Eugene C. Lin, Tiffany Poon, Indroneal Banerjee, Ju Chen, Samuel L, Pfaff, Eduardo. R. Macagno and Pieter C. Dorrestein. The thesis author was the primary author and investigator.

Chapter 3 is a full reprint of the material as it appears in the published article of Analytical Chemistry 2013, vol. 85, pp.7014-7018 by Cheng-Chih Hsu, Mariam S. ElNaggar, Yao Peng, Jinshu Fang, Laura M. Sanchez, Samantha J. Mascuch, Kirsten A. Møller, Emad K. Alazzeh, Jiri Pikula, Robert A. Quinn, Yi Zeng, Benjamin E. Wolfe, Rachel J. Dutton, Lena Gerwick, Lixin Zhang, Xueting Liu, Maria Månsson, and Pieter C. Dorrestein. The thesis author was the primary author and investigator.

Chapter 4 is a modified reprint of the material as it appears in the manuscript prepared to submitted to PLOS ONE 2014 by Samantha J. Mascuch, Wilna J. Moree, Cheng-Chih Hsu, Gregory G. Turner, Tina L. Cheng, David S. Blehert, A. Marm Kilpatrick, Winifred F. Frick, Michael J. Meehan, Lena Gerwick, and Pieter C. Dorrestein. The thesis author is the primary investigator and author of the experimental aspects of this manuscript.

VITA

2001-2005	B.S. in Chemistry, National Taiwan University
2005-2007	M.S. in Chemistry, National Taiwan University
2007-2008	Republic of China Army
2008-2009	Research Assistant, Department of Chemistry, National Taiwan University
2009-2014	Ph.D. in Chemistry, University of California at San Diego

PUBLICATIONS

1. **Cheng-Chih Hsu**, Nicholas M. White, Marito Hayashi, Eugene C. Lin, Tiffany Poon, Indroneal Banerjee, Ju Chen, Samuel L. Pfaff, Eduardo R. Macagno, and Pieter C. Dorrestein, "Microscopy Ambient Ionization Top-Down Mass Spectrometry Reveals Developmental Pattering." ***Proc. Natl. Acad. Sci. USA*. 2013**, 110(37), 14855-14860.

2. **Cheng-Chih Hsu**, Mariam S. ElNaggar, Yao Peng, Jinshu Fang, Laura M. Sanchez, Samantha J. Mascuch, Kirsten A. Møller, Emad K. Alazzeh, Jiri Pikula, Robert A. Quinn, Yi Zeng, Benjamin E. Wolfe, Rachel J. Dutton, Lena Gerwick, Lixin Zhang, Xueting Liu, Maria Månsson, and Pieter C. Dorrestein, "Real-Time Metabolomics on Living Microorganisms Using Ambient Electrospray Ionization Flow-Probe." ***Anal. Chem.***, **2013**, 85(15), 7014-7018.

3. **Cheng-Chih Hsu** and Pieter C. Dorrestein, "Visualize Life by Ambient Mass Spectrometry." ***Curr. Opin. Biotechnol.***, *submitted*.

4. Jeramie Watrous,[†] Vanessa Phelan,[†] **Cheng-Chih Hsu**,[†] ([†]contribute equally) Theodore Alexandrov and Pieter C. Dorrestein, "Microbial Metabolic Exchange in 3D." ***ISME. J.***, **2013**, 7, 770-780.

5. **Cheng-Chih Hsu**, Chao-Chen Lin, Pi-Tai Chou, Chin-Hung Lai, Yun Chi, Chien-Wei Hsu and Chen-Huey Lin, "Harvesting Highly Electronically Excited Energy to Triplet Manifolds: State-Dependent Intersystem Crossing Rate in Os(II) and Ag(I) Complexes." ***J. Am. Chem. Soc.***, **2012**, 134(18), 7715.

6. Ameya Phadke, Chao Zhang, Bedri Arman, **Cheng-Chih Hsu**, Raghunath A. Mashelkar, Ashish K. Lele, Michael J. Tauber, Gaurav Arya, Shyni Varghese, "Rapid Self-healing Hydrogels." ***Proc. Natl. Acad. Sci. USA***, **2012**, 109(12), 4383.

7. Wang Chen, Christopher J. Berg, **Cheng-Chih Hsu**, Brittany A. Merrill, and Michael J. Tauber, "Characterization of Carotenoid Aggregates by Steady-State Optical Spectrometry." ***J. Phys. Chem. B.***, **2012**, 116(35), 10617.

8. Yu-Ching Huang, Wei-Che Yen, Yu-Chia Liao, Ya-Chien Yu, **Cheng-Chih Hsu**, Mei-Lin Ho, Pi-Tai Chou, and Wei-Fang Su, "Band gap aligned conducting interface modifier enhances the performance of thermal stable polymer-TiO_2 nanorod solar cell." ***Appl. Phys. Lett.***, **2010**, 96(12), 123501.

9. Chih-Wei Lai, Yu-Hsiu Wang, Yu-Chun Chen, Cheng-Chih Hsieh, Borade Prajakta Uttam, Jong-Kai Hsiao, **Cheng-Chih Hsu** and Pi-Tai Chou, "Homogenous, far-reaching tuning and highly emissive QD-silica core-shell nanocomposite synthesized via a delay photoactive procedure; their applications in two-photon imaging of human mesenchymal stem cells." ***J. Mater. Chem.***, **2009**, 19(44), 8314-8319.

10. Hsin-Sheng Duan, Pi-Tai Chou, **Cheng-Chih Hsu**, Jui-Yi Hung and Yun Chi, "Photophysics of Heteroleptic Iridium(III) Complexes of Current Interest; a Closer Look on Relaxation Dynamics." ***Inorg. Chem.***, **2009**, 48(14), 6501-6508.

11. Kew-Yu Chen, Yi-Ming Cheng, Cheng- Hsuan Lai, **Cheng-Chih Hsu**, Mei-Lin, Ho, Gene-Hsiang Lee, Pi-Tai Chou, "ortho-GFP Synthetic Chromophore; Excited State Intramolecular Proton Transfer via a Seven-membered Ring Hydrogen Bonding System." ***J. Am. Chem. Soc.***, **2007**, 129(15), 4534-4535.

12. Fang-Chi Hsu, Yung-Liang Tung, Yun Chi; **Cheng-Chih Hsu**, Yi-Ming Cheng, Mei-Lin Ho, Pi-Tai Chou, Shie-Ming Peng, "En Route to the Formation of High Efficiency, Osmium (II) Based Phosphorescent Materials." ***Inorg. Chem.***, **2006**, 45(25), 10188-10196.

13. Shih-Chieh Pu, Meng-Ru Yang, **Cheng-Chih Hsu**, Cheng-Chih Hsieh, Pi-Tai Chou, Sheng-Hsien Lin and Yi-Ming Cheng, "The Empirical Correlation between Size and Two-photon Absorption Cross Section on CdSe and CdTe Quantum Dots." ***Small***, **2006**, 2(11), 1308-1313.

14. Elise Y. Li, Yi-Ming Cheng, Cheng-Chih Hsu, Pi-Tai Chou, and Gene-Hsiang Lee, "Neutral Ru(II)-Based Emitting Materials: A Prototypical Study on Factors Governing Radiationless Transition in Phosphorescent Metal Complexes." ***Inorg. Chem.***, **2006**, 45(20), 8041-8051.

15. Shih-Wen Li, Yi-Ming Cheng, Yu-Shan Yeh, **Cheng-Chih Hsu**, Pi-Tai Chou, Shie-Ming Peng, Gene-Hsiang Lee, Yung-Liang Tung, Pei-Chi Wu, Yun Chi,* Fang-Iy Wu, Ching-Fong Shu, "Interplay between Intra- and Interligand Charge Transfer with Variation of the Axial N-Heterocyclic Ligand in Osmium(II) Pyridylpyrazolate Complexes: Extensive Color Tuning by Phosphorescent Solvatochromism." ***Chemistry - A Eur. J.***, **2005**, 11(21), 6347-6357.

16. **Cheng-Chih Hsu**, Michael W. Baker, Eduardo R. Macagno, and Pieter C. Dorrestein, "Top-Down Mass Spectrometry Reveals Molecular Signature of Medicinal Leech Neural Systems Under Fluorescence Microscope." *in manuscript*.

17. Samantha J. Mascuch, Wilna J. Moree, **Cheng-Chih Hsu**, Gregory G. Turner, Tina L. Cheng, David S. Blehert, A. Marm Kilpatrick, Winifred F. Frick, Lena Gerwick, and Pieter C. Dorrestein, "Direct detection of fungal siderophores fluorescence microscopy guided ambient ionization mass spectrometry of bats with white-nose syndrome." *in manuscript*.

CONFERENCE AND SEMINAR PRESENTATIONS

Oral Presentations

1. **Cheng-Chih Hsu**, et al., "Microscopy Guided Atmospheric Ionization *In Situ* Top-Down Protein Mass Spectrometry." *61th Am. Soc. of Mass Spectrometry Conference*, Minneapolis, MN, 2013.

2. **Cheng-Chih Hsu**, "Visualizing the Biology Using Ambient Ionization Mass Spectrometry Microscope." *Special Seminar*, Taipei Medical University, Taiwan, 2014.

3. Mariam ElNaggar; **Cheng-Chih Hsu**; Xueting Liu; Pieter Dorrestein; Bartek Rajwa; Justin Wiseman "Applications of an *in situ* Microextraction Based Surface Sampling System to Microorganism Analysis." *61th Am. Soc. of Mass Spectrometry Conference*, Minneapolis, MN, 2013.

Poster Presentations

1. **Cheng-Chih Hsu**; Chen Wang; Michael J. Tauber; "Fluorescence of Zeaxanthin Aggregates." *58th Annual Western Spectroscopy Association Conference (now: Pacific Conference on Spectroscopy and Dynamics)*, Asilomar, Pacific Grove, CA, 2011.

2. **Cheng-Chih Hsu**; Pieter Dorrestein; Eduardo Macagno; Tiffany Poon; Samuel Pfaff; "Ambient Mass-Fluorescence Microscopic Analysis in Biology." *60th Am. Soc. of Mass Spectrometry Conference*, Vancouver, Canada, 2012.

ABSTRACT OF THE DISSERTATION

Development of Microscopy Ambient Ionization Top-down Mass Spectrometry

by

Cheng-Chih Hsu

Doctor of Philosophy in Chemistry

University of California, San Diego, 2014

Professor Pieter C. Dorrestein, Chair

There is an immense cellular and molecular heterogeneity in biological system. For example, during the embryonic development, the progenitor cells could differentiate into varieties type of cell due to the gradient of chemical stimulus. Once the cell fate is determined, the metabolomics and proteomic features of the cell will subsequently alter. Knowing the details of the molecular interplays between cellular and chemical heterogeneities is crucial in the understanding of the complex biological system.

Mass spectrometry, provides a way of label-free strategy to obtain the chemical information. In the recent decades, considerable amounts of new ionization methods were developed for the use of mass spectrometric analysis on biological system. Among those methods, those so-called "soft ionization" techniques, such as matrix-assisted laser desorption (MALDI) and electrospray ionization (ESI), have been greatly utilized for

biomedical studies. However, some technical limitations currently hinder the application to the more general biology society. First, the spatial mass spectrometric measurement is solely based on passive imaging processes. In this regard, a real-time chemical investigation guided by the histological measurement, e.g. optical microscopy, is difficult. Second, high sensitive instruments that allow detection of full molecular weight range, e.g. covering small metabolites, lipids, and proteins, are rare and hardly used for imaging. Third, ionization methods for surface analysis are challenging for soft biological samples, e.g. bacterial colonies, at their native states. My thesis work is the development of mass spectrometry-based tools that are less limited by the abovementioned aspects and to extend the potential use of mass spectrometry.

In Chapter 1, I will briefly review the current progress of the development on ambient ionization techniques as well as the emergence of their applications to biological system. Chapter 2 describes how I interfaced an inverted fluorescence microscope with an ambient ionization source (nanoDESI) so that the molecular information was obtained via the guidance of microscope directly on glass slides. Endogenous molecules as large as hemoglobin could be characterized without immunostaining. This is for the first time that proteins on *ex vivo* tissue sections could be identified using ambient mass spectrometry. Using this platform we found unique molecular patterns that only express at certain embryonic stages. In Chapter 3 a new ways of microbial metabolomics are introduced using a different surface flow-probe. Chapter 4 we further applied the microscope-mass spectrometry interface to study bats with white-nose syndrome. Key molecules that may be causal to the devastating disease are found. Lastly, Chapter 5 put forth a future direction how tools described in the thesis can be extended to cancer pathology.

Chapter 1

Ambient Ionization Mass Spectrometry and Its Application to Life Science: An Introduction

1.1 Abstract

In 2004, an innovative ionization method was described by exerting a stream of highly charged micro-droplets directly onto intact sample surfaces in which a high-sensitive mass spectrometric analysis can subsequently be made through the aerosol plume generated at atmospheric environment. This technique, now well known as desorption electrospray ionization (DESI), enables a label-free chemical analysis of biological samples with substantial minimum sample preparation. Although many other techniques that allow mass spectrometric measurement directly on sample surfaces had been developed before the year 2004, DESI is most-widely accounted as the milestone among all the other similar ionization methods. Since then, a large amount of ionization methods for mass spectrometry measurement have been developed and later referred to as ambient ionization mass spectrometry. Moreover, ambient ionization mass spectrometry has found applications in wide varieties of extension at chemistry level in biological and medical sciences, including neuroscience and cancer pathology. In the past few years,

novel multimodal platforms that interface ambient mass spectrometry to the other cross-disciplined technologies have granted the applications on pharmaceutical science, such as microbial natural product discovery, and even surgical operation. In this chapter, I will introduce some of the most influential technological advances on ambient ionization mass spectrometry and their application in life science, covering literatures in the most recent years.

1.2 Basic Scopes of Ambient Ionization Mass Spectrometry

Cellular and molecular heterogeneity in biological systems is enormous. Knowing the details of the inter-correlations between cellular and chemical heterogeneities is crucial in order to gain insight into the overall picture of how a set of highly diversified cells constituting a complex biological entity works together, as well as the in-depth mechanisms underlying macroscopic physiological behavior such as embryo development and tumorigenesis. Conventionally the knowledge of this chemical heterogeneity can only be accessed through some very limited techniques with the needs of chemical labels or antibodies. However the types of molecules that are able to be visualized by immune-based techniques are confined, usually only molecules with highly specificity, especially proteins, are applicable.

In the recent decades, the idea of getting label-free chemical information from the biological system has come into practice due to the development of biomolecules-compatible ionization methods for mass spectrometry (MS), e.g. electrospray ionization (ESI) and matrix-assisted laser desorption ionization (MALDI).[1,2] The mass spectral data,

if acquired in a spatial manner, can be intuitively reconstructed as mass spectrometry imaging (MSI) that provides the ability to simultaneously visualize distribution of multiple molecular entities. During the last decade, a large quantity of ionization methods has been developed combining MSI for biological systems, showing the strength of MS-based research and profound impacts on life sciences.[3]

In the context of such progress, it is not overestimating that since the term "**ambient mass spectrometry**" was for the first time phrased and introduced to science communities by Cooks *et al.* in 2006, the technological development of ambient ionization methods has entered the golden age.[4] Since then, *ambient mass spectrometry*, or *ambient ionization mass spectrometry*, has extensively been acknowledged by analytical science as well as biological and medical sciences. Although during the past decade there have been varieties of ambient ionization techniques published and their mechanisms are considerably different, each ambient ionization MS technique follows three main principles: (1) Ions are generated and maintained under atmospheric pressure and room temperature (for most of the techniques) before mass spectrometric analysis; (2) samples do not require any pretreatment or only require minimal preparation; (3) analytes are directly desorbed/ionization from the sample surface that an instantaneous or real-time MS measurement is allowed (Figure 1.1). The scope of this introductory chapter aims at mostly extractive-based methods, including desorption electrospray ionization (DESI), nanospray desorption electrospray ionization (nanoDESI), as well as techniques showing high biomedical impacts or potentials that are published in the most recent years.

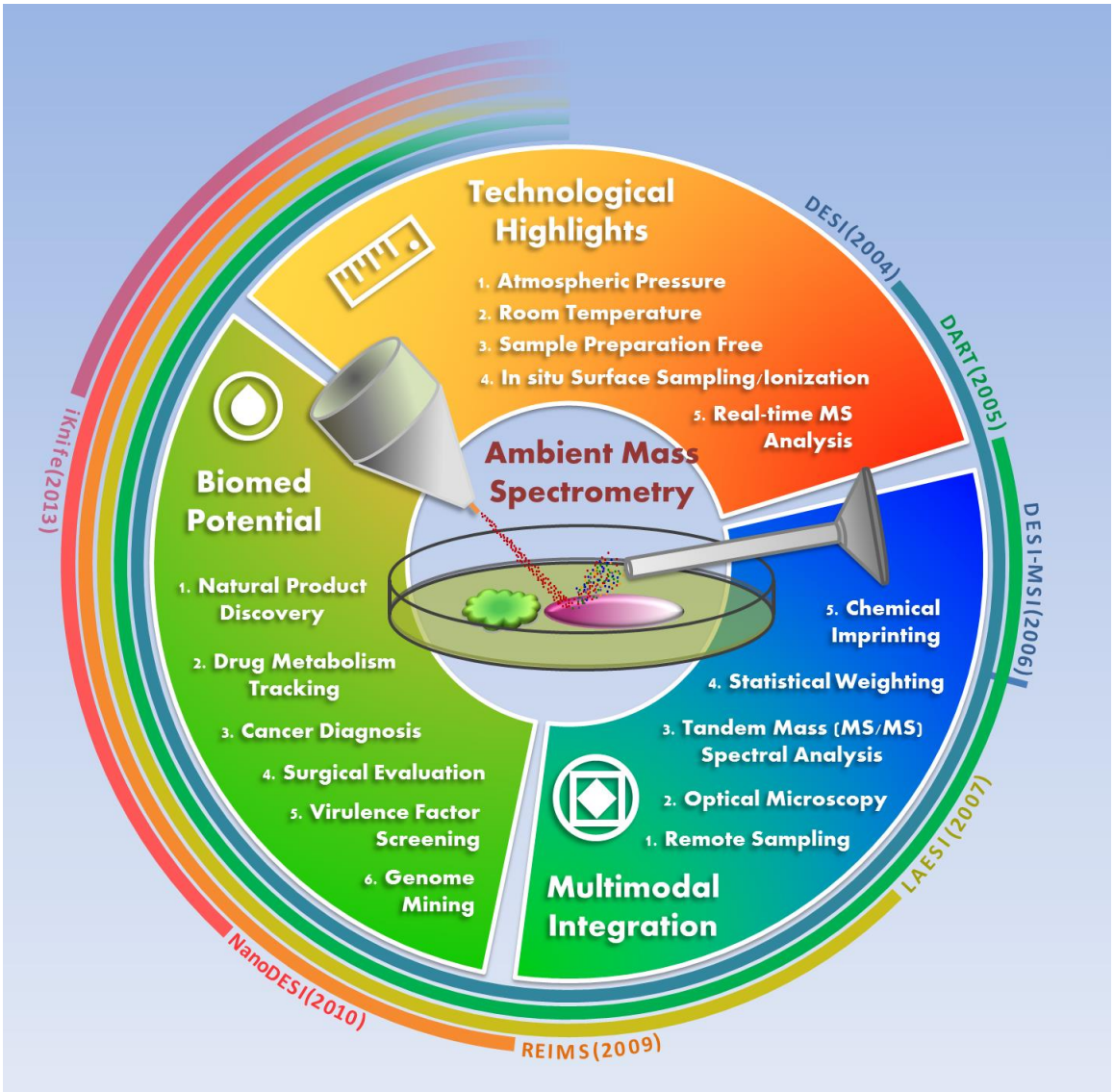

Figure 1.1 Current trends of ambient mass spectrometry. *Center:* Schematic diagram of desorption electrospray ionization (DESI) source obtaining chemical information from a biological sample surface. A stream of charged micro-droplets (in red) is sprayed onto the sample surface to desorb and ionize compounds (in multiple colors), during which molecules retain in their structural intact states. DESI is the most widely used ambient ionization methods for mass spectrometry analysis. *Outer strips:* Time frame of the major development in ambient ionization mass spectrometry methods since DESI MS was reported in 2004. The year of the first publication using the indicated ion sources are listed in the parentheses.

1.3 Desorption Electrospray Ionization (DESI)

1.3.1 The Basics

The introduction of desorption electrospray ionization (DESI) by Cooks laboratory in 2004 is the landmark in the history of ambient ionization mass spectrometry.[5] DESI utilize a nebulized electrospray of highly charged microdroplets to pick up the analytes directly from the sample surface. The subsequent secondary droplets carry the dissolved analytes to the mass spectrometry without separation procedures (Figure 1.1). Similar to conventional ESI of bulk solution, gaseous ions are believed to be created by electrostatic explosion and evaporation, so that the mass spectrometric behavior of DESI is close to ESI.[5] Within a decade, this technique has soon been widely recognized as a revolutionary tool for mass spectrometry analysis in life science.

DESI MS analysis on biological tissues has been used for direct chemical profiling since 2005. The pioneering work published by Wiseman *et al*. presents the first ambient mass spectrometry analysis to animal tissue sections without any sample pretreatment.[6] Strong ion signals from phospholipids were found at the mass-to-charge (*m/z*) range 700-900 on pancreas and brain tissues. Using DESI MS, the alteration of phospholipid profiles of tumor tissue (metastatic human-liver adenocarcinoma) was also firstly investigated and described in this paper.[6] The same group also applied DESI MS to the native and freshly-cut plant tissue in the same year.[7] Dozens of alkaloids, coniine for example, were identified on different species such as poison hemlock jimsonweed, and deadly nightshade. In 2006, the first whole-section surface MSI at ambient environment without matrix deposition was demonstrated using DESI-IMS on rat brain tissue.[8]

Distinctly specialized spatial distributions of different lipid species reflect the chemical-histological heterogeneity of the brain tissue.

1.3.2 Application on Tissues

DESI is currently the most commonly accessible ambient ionization techniques for qualitative or semi-quantitative mass spectrometric investigation on biological tissue. Automatic 2-dimensional (2D) stages are often employed with DESI ion sources so that to acquire 2D MS images.[9] The lateral resolution of a conventional DESI MSI is normally around few hundred microns.[9] Through careful optimization of operating parameters, particularly solvent composition and solvent flow rate, ~35-μm spatial resolution has been achieved.[10] For the better visualization of endogenous compounds in substructures of the tissue, three-dimensional (3D) DESI MSI could be constructed using 2D overlaid of serial sectioning.[11] Because the DESI MSI platform is operated in continuous scanning mode, smooth flat tissue sections are required for high-quality DESI MSI. However, direct imaging of soft or irregular surfaces such as leaves, flowers, vegetable tissues, and microbial colonies, are challenging. To overcome this obstacle, indirect DESI MSI was made via imprinting techniques, where compounds of interests are transferred onto flat rigid surfaces.[12-14]

Molecules on biological samples were usually recorded in a wide mass spectrum window (from few hundred to several thousand *m/z*). Every ionic molecule has its own favored polarity (positive or negative) determined by its intrinsic chemical properties, e.g. acidity and proton affinity. Typically, ions of the same polarity were recorded throughout the full imaging scan. Since a single sampling spot are not allowed to perform mass

spectrometry profiling more than once, DESI images from a tissue section can only provide ions of one polarity. To access imaging in both polarity, the displaced dual-mode DESI MSI, which uses shifted sub-pixel in y-dimension consecutively, was proposed to record images in positive- and negative-mode on the same sample.[15] However, not every biomolecules of crucial physiological functions on the tissue can be easily ionized using electrospray ionization. For instance, cholesterol is a major precursor of various steroid hormones but barely gets charged using DESI. To improve the sensitivity of these compounds, DESI sources that incorporate active reagents have been implemented on the spatial profiling on biological samples. This so-called reactive DESI, by initiating an *in situ* chemical reaction on endogenous biomoelcules into charged derivatives, largely enhances the imaging quality of cholesterol on tissues.[16,17] The solvent components greatly influence the DESI performance in terms of extent of desorption and ionization of analytes. Usually DESI uses aqueous solution as the spray solvent system, but non-aqueous solvents were also explored to cover a broader range of molecules especially hydrophobic compounds.[18,19]

Cell membrane constitutes a group of diverse lipids with different structures and functionalities that plays important roles to cellular processes. Lipids are facilely ionized by DESI, which has been profoundly applied for the characterization and imaging of wide classes of lipids including fatty acid, phospholipids, sphingolipids, and sterol lipids on biological tissues.[19-34] Increasing literatures published in the past years report that *in situ* lipidomic profiling using DESI is becoming a rapid way to interrogate the disease states at molecular level in cancer cells.[24-34] The chemical disparity in lipid species among tumor and healthy tissues (Figure 1.2) provides a fast and accurate marginal

evaluation that could be used to improve the success rate of surgical resection. DESI lipidomic analysis can be also implemented on small cell populations or cell cultures.[21-23] In addition to the endogenous compounds, DESI MSI was also used as label-free tracing of drug and metabolites on histological sections.[35-37]

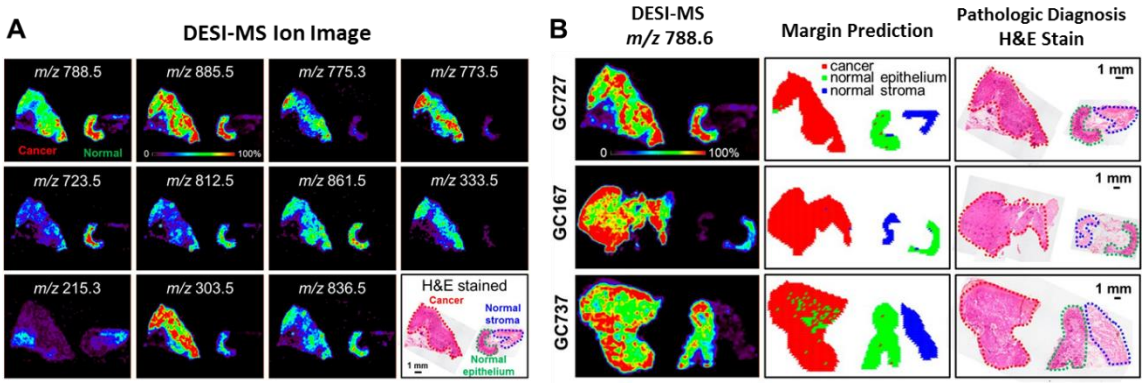

Figure 1.2 Representative DESI MSI of cancer tissue sections. (A) DESIMSI of gastric cancer tissue section (GC727) showing relative ion abundances specifically observed in the regions of cancer or normal epithelial and stromal tissues. Molecular (ion) abundances are usually displayed in false colors. (B) Marginal evaluations (middle panel) of cancerous cells are made by statistical measurements using molecular data (identified as glycerol-phosphoserine) acquired by DESI-MS (left panel). Results of the computational assessment are compared with cancer diagnosis made by pathologists shown in optical images of H&E stained tissue sections (right panel). Figures are reproduced by permission.[32]

DESI MS has also been used to observe the chemical output present within plant tissues.[12,13,38-41] Many plant-derived natural products are found to of great medical values. The enormous structural diversity among the small molecules present in plants gives rise to the utilization of DESI MS analysis and imaging on the vast majority of plant metabolites. Imprinting of compounds from plant tissues onto hard surface, e. g., porous Teflon, prior to DESI MS analysis is necessary especially for imaging.[12,13,38-40] Fine details of chemical cues on fragile plant surfaces could be spatially resolved and these molecular signatures provide insightful information of plants that present distinct

phenotypes or under environmental stresses.[39,40] DESI MSI provides not only an ability to a global exploration of novel metabolites, but also a tool for the chemical representation of particular genotypes. In the work by Li *et al.*, the enzymatic conversion of glycosylated metabolites upon cell disruption and leaf development were visualized by DESI MSI.[39] It is also notable that DESI MS can be used to monitor the environmentally toxic elements accumulated in plants. Organic and inorganic form of arsenic compounds in fern leaves were detected by DESI MS and the results were further quantified by LC-ICP (liquid chromatography coupled to inductively coupled plasma) MS.[41]

1.4 Nanospray Desorption Electrospray Ionization (nanoDESI)

Another solution-phase-mobilized surface desorption/ionization approach that is receiving considerable attention is nanospray desorption electrospray ionization (nanoDESI). This surface sampling technique was developed in Laskin group in 2010.[42] The concept of nanoDESI is derived from DESI and can be considered as the improved version of DESI. The nanoDESI source replaces the primary stream of microdroplets of DESI into a micrometer-size fused silica capillary tube which is continuously infused by highly charged solvents at about 1 μL/min flow-rate. The second capillary tube of the same size is used to aspirate the analytes from the tissue surface via the micro-extraction from a tiny liquid junction sustained on the tissue surface between the two capillary tubes (Figure 1.3A). The subsequent nanoelectrospray ionization occurs at the terminal end of the secondary capillary tube by which the concurrent ions of analytes as well as carrier solvent are pulled into the mass spectrometer via electrostatic force and capillary action.

The nanoDESI source was soon coupled with MSI scanning platform for a very gentle surface lipidomic mapping on rat brain tissue.[43,44] Because the splash of secondary solvent microdroplets in DESI is substituted with a self-aspirated capillary tube as the role of the analyte carrier in nanoDESI, the virtual sampling spot-size of nanoDESI is greatly reduced. A spatial resolution of ~10 μm was achieved using nanoDESI MSI, while the resolution of regular DESI MSI is 100-500 μm.[43] This resolution, although not as good as, is compatible to the other laser-induced or -associated desorption ionization methods such as MALDI MSI. Similar to DESI MS, nanoDESI MS has an excellent ability that allows the characterization and imaging of lipids including phospholipids and steroid.[43-35] There are diverse classes of lipids constituting cell membrane, by which molecular weights could be very close to each other (~50 ppm). Conventional separation procedures, such as liquid chromatography are prerequisite for qualitative and quantitative MS-based lipidomic analysis. Alternatively, by coupling with high resolution mass spectrometer, nanoDESI MS provides an efficient way to resolve endogenous lipid species with very close molecular weights that possess distinctive distribution among biological sections.[44] Recently, Laskin group demonstrated that by doping the nanoDESI solvent with phospholipid standards, online quantification of many other molecular species of the same phospholipid family during MSI is possible in a single experiment.[45]

Moreover, nanoDESI also has been used to the imaging of small metabolites at lower *m/z* region. Imaging of small metabolites by MALDI MS are usually challenging due to the matrix effect and ion suppression. Matrix-free approaches such as DESI and nanoDESI are essential for the MS analysis to small molecules. Distributions of small metabolites involved in energy metabolism and cell proliferation that associated with

pregnancy were recently revealed by nanoDESI MSI on uterine sections.[46] Bearing the ability to characterize compounds with smaller molecular weights, nanoDESI MS can act as the complementary tool with other mass spectrometry methodologies such as MALDI MSI for the characterization of key metabolites and metabolic exchanges in complex host-microbial systems.[47] Using germ-free mice guts as the control model, the interaction between gastrointestinal track and gut microbiota, as well as the chemical transformations yielded by the microbiota were revealed.[47] Furthermore, not only to endogenous substances, this approach can also be applied to detect drugs and track drug metabolisms on a complex organ system, e.g. nicotine in rat brain tissue, in a spatial manner.[48]

1.4.1 Microbial Natural Products Discovery and Genome Mining

The secondary metabolites from microbial communities have been a rich source of useful natural products including antibiotics, antifungal, anticancer agent, and immunosuppressants. However, more than 99% of the microorganisms in this planet have not yet been examined for their chemical outputs. In most of the cases tedious procedures, including liquid-phase extraction and isolation of analytes using liquid chromatography, are required prior to MS analysis. However, these laborious steps become unrealistic when aiming for a large set of microbial species. An ability that allows instantaneous MS analysis of microbial natural products bypassing the time-consuming preparations is of significance in pharmaceutical science. One of the advantages the nanoDESI source has is the relatively slight damage to the sample that is caused during its sampling process. The bombardment on the sample surface initiated by charged micro-droplet in DESI is detrimental to soft samples and inevitably gives rise to delocalization of analytes. The

imprinting of compounds to a rigid substrate is essential for a high quality DESI MSI on soft samples.[12-14] However, this indirect approach is challenging for the real-time MS analysis on fragile organisms, e.g. live microbial colonies. Using nanoDESI MS, Watrous *et al*. successfully obtained spatiotemporal MS profiles of live microorganisms directly from Petri dishes (Figure 3A), that contain profound chemical information of microbe-derived natural products.[49]

Another greater challenge now has is the expensive costs and enormous labor work that are required to the identification and structural elucidation of the tremendous amount of microbial metabolites. This work by Watrous *et al.* also demonstrated that by comparing the tandem mass (MS/MS) spectral similarity (Figure 3B), which is later referred to as "molecular networking", massive amount of secondary metabolites secreted from microbes as well as the metabolic exchanges between microbial communities are revealed (Figure 3C).[49] This nanoDESI-MS/MS networking strategy has been applied to the metabolomics elucidation of a large variety of microbial species.[49-52] Furthermore, the ease of this nanoDESI MS/MS-guided approach enables a new bioinformatics paradigm of genome mining called peptidogenomics,[53] in which MS/MS profiles of peptidic natural products from species of closely related microorganisms (identified as "molecular families") are rapidly screened on living colonies, and brought up to locate the associating gene cluster families (Figure 3D). This genome-mining method, that connects MS/MS spectral patterns of microbial peptide families to their biosynthetic gene cluster families, has been conceptually carried out directly on the top of living microbial colonies of ~60 related strains.[50]

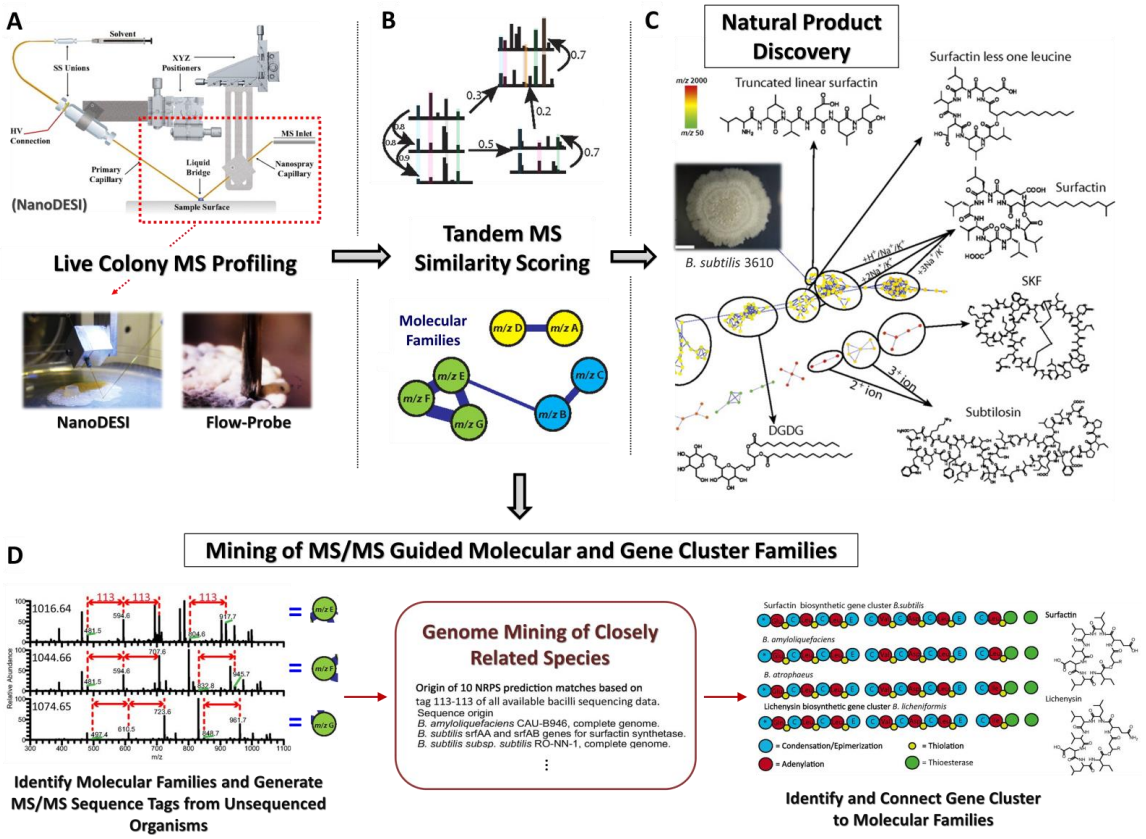

Figure 1.3 Overall real-time microbial metabolomics and peptidogenomics workflow basing on tandem mass spectral analysis. Molecular information is directly fetched from the surface of microbial colonies using nanoDESI[49] or continuous flow-probe[63] as depicted in step **A**. The massive MS/MS (molecular fragments) data are then grouped into multiple subsets (called "molecular families") basing on the fragmentation patterns. Each node represents an individual ion and connects to each other showing the spectral similarity between each pair (**B**). The MS/MS-based computational pipelines have been extensively applied to high-throughput mining of microbe-derived natural products for an instantaneous insight into the molecular classes and structural elucidation (**C**). The pipelines can further be utilized to connect nonribosomal peptide synthetases (NRPSs) gene clusters to the molecular families (**D**). The figure is reproduced by permission.[49,50,63]

MSI using nanoDESI for microbial colonies is complicated as the surfaces of colonies are usually rugged. It is necessary for the use of z-axis adjustment to the probe position in order to follow the contour of the colony, so as to prevent clogging and loss of signal due to collision with or contact losing from the sample surface.[52,54] To compensate the vertical tolerance between the tip of the probe and sample surfaces, nanoDESI MSI

requires larger droplet. This change results in poorer spatial resolution (usually ~ few-hundred μm) compared with the imaging on flat tissue sections.[52] Meanwhile, nanoDESI displays a distinguished ability of targeted *in situ* MS characterizations of pathogen-derived virulence compounds on host tissues. Recently, using nanoDESI to probe directly onto fungi-colonized bats of white nose syndrome (WNS), we acquired the MS evidences showing that the iron-chelating compounds secreted by the pathogen are presented on infected bats. This work is among the first examples in which microbial molecules are directly detected on the infected host and might provide insight into the pathogen-host interaction. More details will be covered in Chapter 4.

1.5 Combinatorial Ambient Ionization Techniques

The adaptation of ambient ionization mass spectrometry with the other techniques has also been developed. The use of the current MS-based multimodal tools allows for better visualization, portability, and flexibility. In the following I will highlight some of newly developed techniques of the most recent year that are coupling with ambient ionization mass spectrometry.

1.5.1 Microscopy Ambient Ionization Mass Spectrometry

In this work published by Dorrestein group, an inverted light microscope was interfaced with nanoDESI MS into a single platform for a better visualization of samples and improved targeted MS analysis (Figure 1.4).[55] Using this integrated platform, the area of interests on the biological sample surface can be targeted by the light microscope

and the subsequent mass spectrometric analysis can be made *in situ* by nanoDESI. A broad range of endogenous molecules associated with embryonic development of central nervous system is revealed. It is particularly notable that via the positioning over the microscope, a pixel-by-pixel data acquisition is achieved for the construction of MSI, which is contrary to the conventional DESI or nanoDESI MSI that are taken via continuous scanning. Generally, the MS sensitivity of nanoDESI are thought to be greater than DESI, as the splash of secondary microdroplets in DESI is substituted with a capillary tube analyte carrier in nanoDESI that give rise to a better ion transfer efficiency. In this regard, Dorrestein group demonstrated that the MS sensitivity can be further improved with prolonged pixel-by-pixel data acquisition for the MS visualization of proteins that show unique patterns during embryonic development. Unlike MALDI, ESI-based ion sources give multiple charges on a protein that usually results in low detection limit of a protein compared to a small metabolite with unitary charge. The work shows for the first time a protein could be identified directly from a tissue section without matrix deposition using ambient ionization MS. The development and uses of this technique is the main topic of my dissertation. Details of the applications using microscopy ambient ionization mass spectrometry will be elaborated throughout the following chapters.

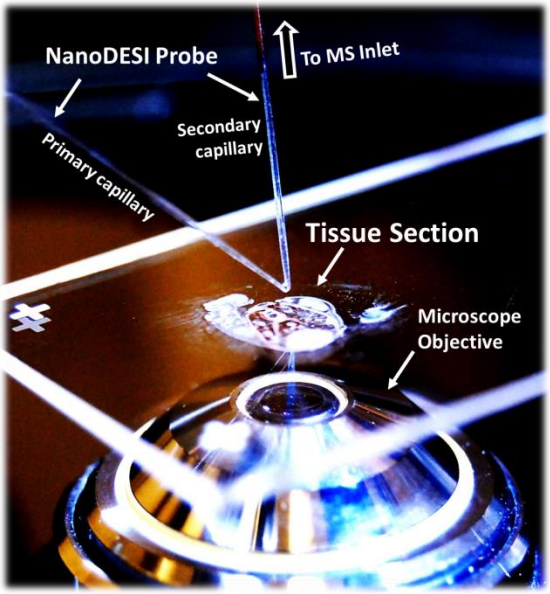

Figure 1.4 Photo of a real-time snapshot of the microscope-nanoDESI platform. The platform is about to make MS measurement from a mouse embryo section mounted on a regular microscope slide.[55]

1.5.2 Atomic Force Microscope Probe Mass Spectrometry.

This multimodal imaging technique adapts an atomic force microscopy (AFM) system with the capability for MSI at atmospheric pressure.[56] The platform is first operated at regular AFM mode to obtain topographical images with spatial resolution at sub-micrometer level. The same AFM proximal probe is then heated to ~350 ^{o}C to enable thermal desorption of the analytes on the sample surface, which is further ionized by a supplementary atmospheric pressure chemical ionization (APCI) source to give MS data. A MS image of the sample surface is made and co-registered with the topographical contour. However, its MS sensitivity and the subsequent ability to identify compounds are not comparable with other ambient ionization method. Although it might open up a new avenue by showing a high spatial-resolution MS profile from ink patterns on paper, its capability for MS analysis on biological system remains unclear.

1.5.3 Ambient Ionization on Bulk Samples

Ambient ionization methods are less restricted by sample geometry compare to MALDI. Designs for direct and indirect targeted MS analysis over native bulk samples has been developed and demonstrated to the use of biological systems.[57-62] In most of the indirect approaches, materials on sample surfaces are collected by needles and transferred for MS analysis. Needle-based spray ionization were shown as a low-invasive *in vivo* sampling method to provide a rapid molecular information in relation to the disease states of specific organs or biopsy for immediate medical diagnosis.[57-60] Usually a high voltage is applied directly onto a needle, with a small piece of tissue punch attaching on the needle tip, to create spray ions for the subsequent MS analysis. The tissue punch could further be transfer to a secondary ionization source, e.g. paper spray technology, for a better MS performance.[60] Alternatively, techniques involving direct application of high voltage onto bulk tissues were also made. For example, it was demonstrated that endogenous biomolecules of living plants and fresh fruits at target regions were detected using *in vivo* nanoelectrospy ionization MS analysis, in which a tiny capillary is partially inserted into the tissue and a high voltage is applied directly onto the plant tissue to generate electrospray on the capillary tip.[61] A similar strategy call internal extractive electrospray ionization (iEESI) MS was also made by a direct infusion of highly charged solvent with a subsequent electrospray initiated by the electrostatic gradient along bulk volume of intact samples.[62] Recently, a report presents a robotic sampling probe for MSI in three-dimensional (3-D) sample surfaces.[63] In this proof-of-concept study, distribution of the standard dye compound on a polystyrene hemisphere was automatically mapped. We envision profound biological applications for this technique in the future.

1.5.4 Remote Sampling Using Long Distance Ion Transfer

Real-time MS measurement on large bulk objects is difficult because the operation of most ionization sources does not allow molecules to travel with a long distance in either solution phase or ionic gas phase. The idea of distant MS sampling at ambient environment has been made possible using different ionization sources that enable a high efficient transfer of neutral molecules or ions.[64-69] A coaxial geometry liquid micro-junction surface sampling probe (LMJ-SSP) was developed with the ability of direct micro-extraction of analytes from sample surfaces for subsequent MS analysis. A remote sampling in real-time was achieved pneumatically using a concentric nebulizer to transfer the neutral analytes via a fused silica capillary to generate electrospray current few inches away from the surface of samples, e.g. microbial colonies.[64] Recently, a regular DESI source was adapted with a rigid 50-centimeter air flow-assisted ion transport tube for a whole-body section MSI of an adult rat.[65] The modified DESI MS provides high sensitive molecular mappings revealing the dynamic drug metabolism and biotransformation.[65] Furthermore, an extended DESI source coupled with a 4-meter ion transmission Tygon tubing has been demonstrated for the distant ionization and MS analysis of polar lipids from a rat brain tissue.[66] The flexibility of the design and adequate ion transmission efficiency are promising for *in vivo* MS analysis compatible with surgical and endoscopic procedures.

The attempt to make remote ambient sampling/ionization for surgical uses has also been exploited using rapid evaporative ionization mass spectrometry (REIMS).[67] REIMS technology utilizes an electrosurgical dissector to generate aerosols containing gaseous ion of analytes from the surgical site. The thermoelectrically generated ions are

transmitted to distant mass spectrometer via a flexible polymer transfer tubing, which is connecting to a Venturi gas jet pump to pull the ions pneumatically.[68] The coupling of REIMS with monopolar or bipolar electrosurgery for tissue diagnostics is later known as the intelligent knife (iKnife) that are implemented for MS-based intraoperative tissue identification as depicted in Figure 1.5.[68] REIMS technology was also used to acquire MS profiles of microbial biomass. Microorganisms among different genus and species were categorized based on their mass spectral fingerprints using REIMS.[69,70]

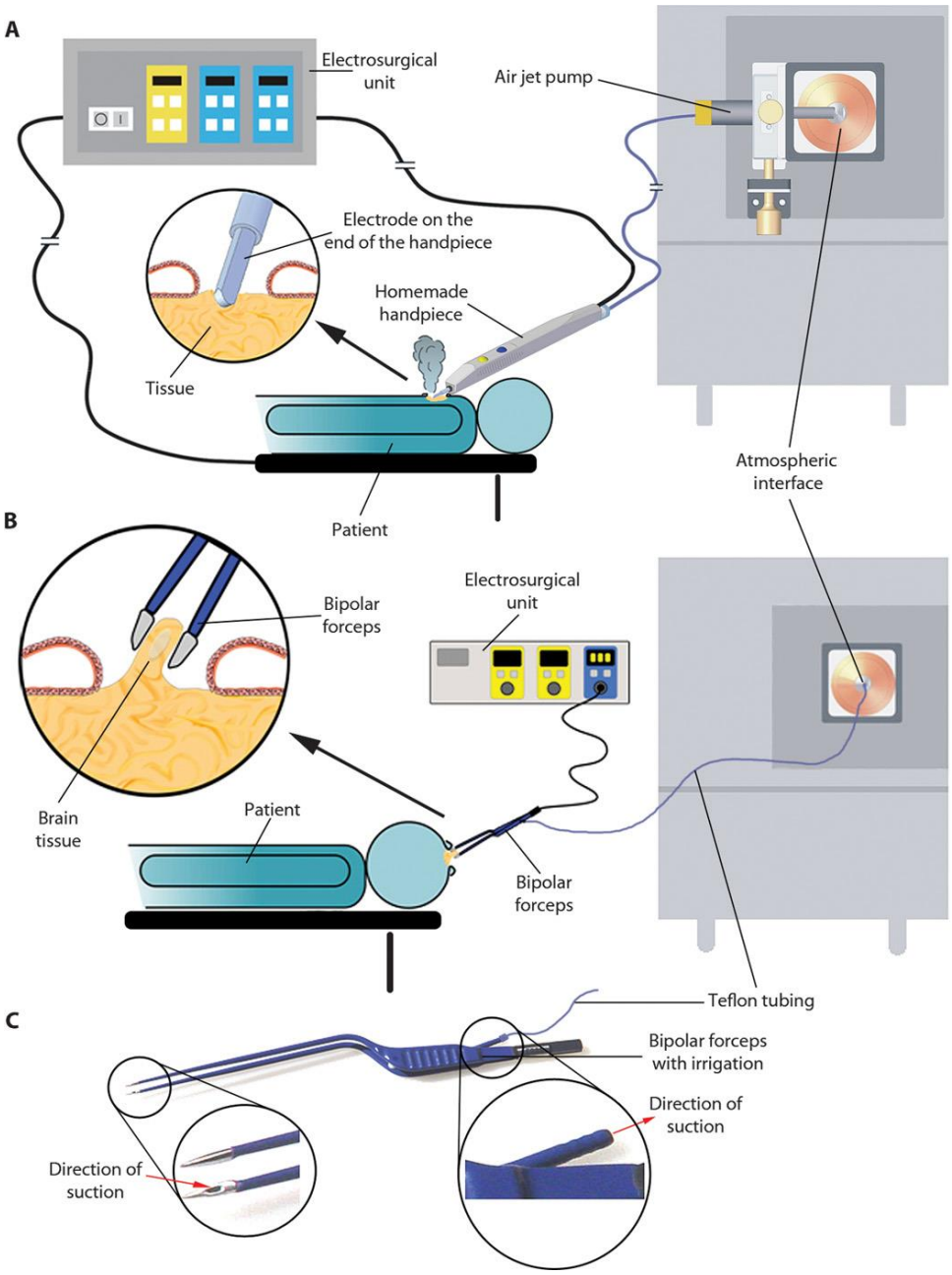

Figure 1.5 Schematic diagram of iKnife technology for real-time data collection in the operating theater using monopolar (A) or dipolar (B) electrosurgery. Evaporative products in REIMS experiment directly from patient tissues are remotely transferred via Teflon tubing into mass spectrometer. The real-time MS patterns provide surgeons an instantaneous indicator to determine tumor margins. Bipolar forceps (C) are commercially available for electrosurgical practices and are used as a REIMS ion source to generate evaporative aerosols. The figure is adapted by permission.[68]

1.6 Clinical Use and Cancer Pathology

An increasing number of research articles have been published in the recent years providing the evidences to the power and usefulness of ambient ionization MS to clinical study especially cancer research.[24-34,57-60,66,68] I will primarily focus on its applications relating to cancer studies in this section.

So far most of the influences exerted by the ambient MS involvement are on the study of global shift in cell metabolism of cancers at prognostic stages. The current attempts to incorporate ambient ionization MS technology for cancer study are mainly aiming at three aspects. First, it permits an ability of large-scale chemotypical screening at malignant regions which is essential to the establishment of region-specific molecular database for the discovery of biomarkers. Second, it offers a mean of tissue classification in cancers solely based on the molecular signatures obtained from tissue sections. Third, it provides molecular assessment and discrimination that could be used to assist surgeons in improving the cancer tissue clearance and decision-making during surgery.

DESI-based approach is the most profoundly used technique among all ambient MS methodologies to acquire prognostic molecular information from cancerous tissues.[24-34] More and more mass spectral evidences obtained from various types of cancer suggest that tumor cells present distinctive lipidomic profiles, representing a characteristic shift in lipid metabolism from normal cells. Such molecular maneuvers are readily detected by DESI MSI, featuring indicative disease states on morphological regions of tissues. Spatially resolved lipid mappings on cancerous tissue sections using DESI MSI have been vastly employed for the discrimination of tumor cells from normal tissues.[24-34] Moreover, the altered lipid metabolisms associated with cancer-causing genes, e.g. MYC

oncogene, can also be captured from *in situ* DESI analysis on oncogene-induced tumor sections. The pioneering work orchestrated in Stanford University shows that by switching the certain genes on and off, a highly specific lipid profile was revealed illustrating distinguishable metabolic pathways between normal and malignant cells.[28]

Ambient MS techniques that allow distant ionization/sampling have also been developed for molecular investigation of cancers.[59,68] This capability is especially favored when cryosection is impossible. It is notable that REIMS technology, a.k.a. iKnife, was recently shown to display a real-time intraoperative MS characterization of cancerous tissues during surgical interventions in the operating theater (Figure 1.5). Takats and his colleagues demonstrated that the MS-based iKnife technology is able to determine the tumor margins for surgeons so as to improve the accuracy of surgical intervention in cancer treatments and could ideally minimize the costly waiting time during intraoperative histological examination.[68]

1.6.1 Statistical Assessment

As DESI MSI provides a large set of pixel-wise molecular information, statistical and computational approaches for the practice of metabolome-wide cancer diagnosis using ambient mass spectrometry have started to be implemented in medical researches. Computer-assisted classifier basing on MS pattern (mainly lipids) obtained from DESI MSI were used to discriminate variant subtypes of brain tumors, e.g. glioma and meningioma.[29] This strategy, containing multivariate statistics and machine learning, provides a molecular assessment of tumor margin for intraoperative use that is complimentary to histopathology diagnosis.[29,34] Similar strategy, by mathematically

weighting of mass spectral components, mostly ions of small metabolites and phospholipids, was used to determine disease states and surgical-resection margins of gastrointestinal cancers.[32] It is noteworthy that because the assessment is solely determined by statistical features of each *m/z* value, those statistics-guided measurements using DESI MSI are irrelevant to and does not require molecular identity. Although the analytical procedures for chemical identification are valuable, they are also very time-consuming and difficult to be made during intraoperative diagnosis. In addition, there are some limitations for the chemical interrogation of clinical uses. Those limitations, including (i) interferences from noise- and solvent-related signals, (ii) MS intensity variances, (iii) mismatching between MSI and histology images, (iv) lack of methods to extract biochemical signatures specific to distinct tissue type, hinder the establishment of the dataset in large-scale and high-throughput manners. In this regards, a comprehensive framework for histology-driven DESI MSI was introduced recently using colorectal cancer as the model.[31] This integrated bioinformatics workflow proposes a refined strategy, which aims to optimize the efficacy of currently-limited DESI MSI platforms for cancer pathology.

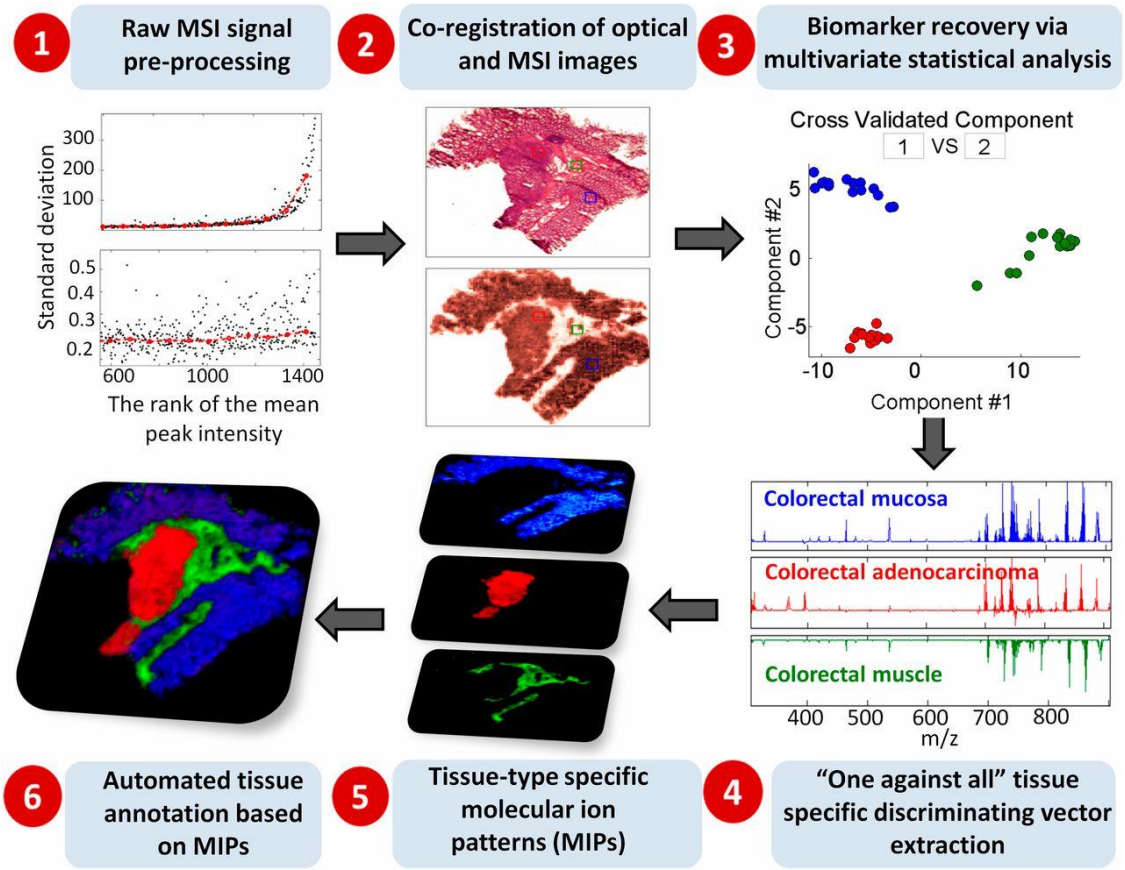

Figure 1.6 Overall computational workflow for tissue-specific molecular exploration on cancer tissues. The workflow uses integrated bioinformatics DESI MS Imaging platform which covers data-processing, co-registration of multimodal images, mining of tissue-specific MS patterns, and reconstruction of chemo-pathological annotation. The figure is adapted by permission.[31]

1.7 Concluding Remarks

With the advent and burgeoning development of a variety of ambient mass spectrometry technologies, the discovery of chemical complexity underlying biological systems and diseases will endure. The stunning extension of the techniques that provides instantaneous molecular information could possibly resemble the methodological shifts in life sciences that have been framed by the other technological advancements, e.g. nuclear magnetic resonance imaging, by which multiple scopes of biological systems and

diseases are revealed. In addition, combining with computational approaches, new ambient mass spectrometry platforms start to show their ability to provide high-throughput and cost-effective chemical screening. These new platforms, though preliminary, open up whole new avenues for future research on life science. Although the technologies covered in this review chapter are limited by manuscript pages, many more ambient ionization techniques possessing variant ionization mechanisms, such as cold plasma-based (the most representative is "direct analysis in real time" or "DART") or laser-based (e.g. laser ablation electrospray ionization or "LAESI") ambient ion sources, have also been presented for the application on life sciences.[71-73] In the end, I hope that through the brief introduction in this chapter, the ease and potential of ambient mass spectrometry are advocated to academic fields outside of mass spectrometry expertise. More importantly, through the introduction of the developmental history of ambient ionization MS, readers will have a deeper understanding to the works elaborated in the following chapters.

1.8 References

(1) Fenn, J. B.; Mann, M.; Meng, C. K.; Wong, S. F.; Whitehouse, C. M. Electrospray ionization for mass spectrometry of large biomolecules. *Science* **1989**, *246*, 64-71.

(2) Hillenkamp, F.; Karas, M.; Beavis, R. C.; Chait, B. T. Matrix-assisted laser desorption/ionization mass spectrometry of biopolymers. *Anal. Chem*. **1991**, *63*, A1193-A1202.

(3) Watrous, J. D.; Alexandrov, T.; Dorrestein, P. C. The evolving field of imaging mass spectrometry and its impact on future biological research. *J. Mass Spectrom.* **2011**, *46*, 209-222.

(4) Cooks, R. G.; Ouyang, Z.; Takats, Z.; Wiseman, J. M. Ambient mass spectrometry. *Science* **2006**, *311*, 1566-1570.

(5) Takats, Z.; Wiseman, J. M.; Gologan, B.; Cooks, R. G. Mass spectrometry sampling under ambient conditions with desorption electrospray ionization. *Science* **2004**, *306*, 471-473.

(6) Wiseman, J. M.; Puolitaival, S. M.; Takats, Z.; Cooks, R. G., Caprioli, R. M. Mass spectrometric profiling of intact biological tissue by using desorption electrospray ionization. *Angew. Chem., Int. Ed*. **2005**, *44*, 7094-7097.

(7) Talaty, N.; Takats, Z.; Cooks, R. G. Rapid in situ detection of alkaloids in plant tissue under ambient conditions using desorption electrospray ionization. *Analyst* **2005**, *130*, 1624-1633.

(8) Wiseman, J. M.; Ifa, D. R.; Song, Q.; Cooks, R. G. Tissue imaging at atmospheric pressure using desorption electrospray ionization (DESI) mass spectrometry. *Angew. Chem., Int. Ed*. **2006**, *45*, 7188-7192.

(9) Ifa, D. R.; Wiseman, J. M.; Song, Q.; Cooks, R. G. Development of capabilities for imaging mass spectrometry under ambient conditions with desorption electrospray ionization (DESI). *Int. J. Mass Spectrom.* **2007**, *259*, 8-15.

(10) Campbell, D. I.; Ferreira, C. R.; Eberlin, L. S.; Cooks, R. G. Improved spatial resolution in the imaging of biological tissue using desorption electrospray ionization. *Anal. Bioanal. Chem*. **2012**, *404*, 389-398.

(11) Eberlin, L. S.; Ifa, D. R.; Wu, C.; Cooks, R. G. Three-dimensional vizualization of mouse brain by lipid analysis using ambient ionization mass spectrometry. *Angew. Chem., Int. Ed.* **2010**, *49*, 873-876.

(12) Thunig, J.; Hansen, S. H.; Janfelt, C. Analysis of secondary plant metabolites by indirect desorption electrospray ionization imaging mass spectrometry. *Anal. Chem*. **2011**, *83*, 3256-3259.

(13) Ifa, D. R.; Srimany, A.; Eberlin, L. S.; Naik, H. R.; Bhat, V.; Cooks, R. G.; Pradeep, T. Tissue imprint imaging by desorption electrospray ionization mass spectrometry. *Anal. Methods* **2011**, *3*, 1910-1912.

(14) Watrous, J.; Hendricks, N.; Meehan, M.; Dorrestein, P. C. Capturing bacterial metabolic exchange using thin film desorption electrospray ionization-imaging mass spectrometry. *Anal. Chem*. **2010**, *82*, 1598-1600.

(15) Janfelt, C.; Wellner, N.; Hansen, H. S.; Hansen, S. H. Displaced dual-mode imaging with desorption electrospray ionization for simultaneous mass spectrometry imaging in both polarities and with several scan modes. *J. Mass Spectrom*. **2013**, *48*, 361-366.

(16) Wu, C.; Ifa, D. R.; Manicke, N. E.; Cooks, R. G. Rapid, direct analysis of cholesterol by charge labeling in reactive desorption electrospray ionization. *Anal. Chem.* **2009**, *81*, 7618-7624.

(17) Wu, C.; Ifa, D. R.; Manicke, N. E.; Cooks, R. G. Molecular imaging of adrenal gland by desorption electrospray ionization mass spectrometry. *Analyst* **2010**, *135*, 28-32.

(18) Badu-Tawiah, A.; Bland, C.; Campbell, D. I.; Cooks, R. G. Non-aqueous spray solvents and solubility effects in desorption electrospray ionization. *J. Am. Soc. Mass Spectrom.* **2010**, *21*, 572-579.

(19) Eberlin, L. S.; Ferreira, C. R.; Dill, A. L.; Ifa, D. R.; Cooks, R. G. Desorption electrospray ionization mass spectrometry for lipid characterization and biological tissue imaging. *Biochim. Biophys. Acta-Mol. Cell Biol. Lipids* **2011**, *1811*, 946-960.

(20) Girod, M.; Shi, Y.; Cheng, J.-X.; Cooks, R. G. Desorption electrospray ionization imaging mass spectrometry of lipids in rat spinal cord. *J. Am. Soc. Mass Spectrom.* **2010**, *21*, 1177-1189.

(21) Ferreira, C. R.; Pirro, V.; Eberlin, L. S.; Hallett, J. E.; Cooks, R. G. Developmental phases of individual mouse preimplantation embryos characterized by lipid signatures using desorption electrospray ionization mass spectrometry. *Anal. Bioanal. Chem.* **2012**, *404*, 2915-2926.

(22) Gonzalez-Serrano, A. F.; Pirro, V.; Ferreira, C. R.; Oliveri, P.; Eberlin, L. S.; Heinzmann, J.; Lucas-Hahn, A.; Niemann, H.; Cooks, R. G. Desorption electrospray ionization mass spectrometry reveals lipid metabolism of individual oocytes and embryos. *PloS One* **2013**, *8*, e74981.

(23) Bodzon-Kulakowska, A.; Cichon, T.; Golec, A.; Drabik, A.; Ner, J.; Suder, P. DESI–MS as a tool for direct lipid analysis in cultured cells. *Cytotechnology* **2014**, DOI: 10.1007/s10616-014-9734-z.

(24) Eberlin, L. S.; Dill, A. L.; Golby, A. J.; Ligon, K. L.; Wiseman, J. M.; Cooks, R. G.; Agar, N. Y. R. Discrimination of human astrocytoma subtypes by lipid analysis using desorption electrospray ionization imaging mass spectrometry. *Angew. Chem., Int. Ed.* **2010**, *49*, 5953-5956.

(25) Eberlin, L. S.; Dill, A. L.; Costa, A. B.; Ifa, D. R.; Cheng, L.; Masterson, T.; Koch, M.; Ratliff, T. L.; Cooks, R. G. Cholesterol sulfate imaging in human prostate cancer tissue by desorption electrospray ionization mass spectrometry. *Anal. Chem.* **2010**, *82*, 3430-3434.

(26) Masterson, T. A.; Dill, A. L.; Eberlin, L. S.; Mattarozzi, M.; Cheng, L.; Beck, S. D. W.; Bianchi, F.; Cooks, R. G. Distinctive glycerophospholipid profiles of human seminoma and adjacent normal tissues by desorption electrospray ionization imaging mass spectrometry. *J. Am. Soc. Mass Spectrom.* **2011**, *22*, 1326-1333.

(27) Gerbig, S.; Golf, O.; Balog, J.; Denes, J.; Baranyai, Z.; Zarand, A.; Raso, E.; Timar, J.; Takats, Z. Analysis of colorectal adenocarcinoma tissue by desorption electrospray ionization mass spectrometric imaging. *Anal. Bioanal. Chem.* **2012**, *403*, 2315-2325.

(28) Perry, R. H.; Bellovin, D. I.; Shroff, E. H.; Ismail, A. I.; Zabuawala, T.; Felsher, D. W.; Zare, R. N. Characterization of MYC-induced tumorigenesis by in situ lipid profiling. *Anal. Chem*. **2013**, *85*, 4259-4262.

(29) Eberlin, L. S.; Norton, I.; Orringer, D.; Dunn, I. F.; Liu, X.; Ide, J. L.; Jarmusch, A. K.; Ligon, K. L.; Jolesz, F. A.; Golby, A. J.; Santagata, S.; Agar, N. Y. R.; Cooks R. G. Ambient mass spectrometry for the intraoperative molecular diagnosis of human brain tumors. *Proc. Natl. Acad. Sci. U.S.A.* **2013**, *110*, 1611-1616.

(30) Calligaris, D.; Norton, I.; Feldman, D. R.; Ide, J. L.; Dunn, I. F.; Eberlin, L. S.; Cooks R. G.; Jolesz, F. A.; Golby, A. J.; Santagata, S.; Agar, N. Y. Mass spectrometry imaging as a tool for surgical decision-making. *J. Mass Spectrom.* **2013**, *48*, 1178-1187.

(31) Veselkov, K. A.; Mirnezami, R.; Strittmatter, N.; Goldin, R. D.; Kinross, J.; Speller, A. V. M.; Abramov, T.; Jones, E. A.; Darzi, A.; Holmes, E.; Nicholson, J. K.; Takats, Z. Chemo-informatic strategy for imaging mass spectrometry-based hyperspectral profiling of lipid signatures in colorectal cancer. *Proc. Natl. Acad. Sci. U.S.A.* **2014**, *111*, 1216-1221.

(32) Eberlin, L. S.; Tibshirani, R. J.; Zhang, J.; Longacre, T. A.; Berry, G. J.; Bingham, D. B.; Norton, J. A.; Zare, R. N.; Poultsides, G. A. Molecular assessment of surgical-resection margins of gastric cancer by mass-spectrometric imaging. *Proc. Natl. Acad. Sci. U.S.A.* **2014**, *111*, 2436-2441.

(33) Abbassi-Ghadi, N.; Veselkov, K.; Kumar, S.; Huang, J.; Jones, E.; Strittmatter, N.; Kudo, H.; Goldin, R.; Takáts, Z.; Hanna, G. B. Discrimination of lymph node metastases using desorption electrospray ionisation-mass spectrometry imaging. *Chem. Commun*. **2014**, *50*, 3661-3664.

(34) Eberlin, L. S.; Norton, I.; Dill, A. L.; Golby, A. J.; Ligon, K. L.; Santagata, S.; Cooks, R. G.; Agar, N. Y. R. Classifying human brain tumors by lipid imaging with mass spectrometry. *Cancer Res.* **2012**, *72*, 645-654.

(35) Wiseman, J. M.; Ifa, D. R.; Zhu, Y.; Kissinger, C. B.; Manicke, N. E.; Kissinger, P. T.; Cooks, R. G. Desorption electrospray ionization mass spectrometry: imaging drugs and metabolites in tissues. *Proc. Natl. Acad. Sci. U.S.A.* **2008**, *105*, 18120-18125.

(36) Liu, J.; Gingras, J.; Ganley, K. P.; Vismeh, R.; Teffera, Y.; Zhao, Z. Whole-body tissue distribution study of drugs in neonate mice using desorption electrospray ionization mass spectrometry imaging. *Rapid Commun. Mass Spectrom.* **2014**, *28*, 185-190.

(37) Eberlin, L. S.; Mulcahy, J. V.; Tzabazis, A.; Zhang, J.; Liu, H.; Logan, M. M.; Roberts, H. J.; Lee, G. K.; Yeomans, D. C.; Du Bois, J.; Zare, R. N. Visualizing dermal

permeation of sodium channel modulators by mass spectrometric imaging. *J. Am. Chem. Soc.* **2014**, *136*, 6401-6405.

(38) Mueller, T.; Oradu, S.; Ifa, D. R.; Cooks, R. G.; Kraeutler, B. Direct plant tissue analysis and imprint imaging by desorption electrospray ionization mass spectrometry. *Anal. Chem*. **2011**, *83*, 5754-5761.

(39) Li, B.; Knudsen, C.; Hansen, N. K.; Jørgensen, K.; Kannangara, R.; Bak, S.; Takos, A.; Rook, F.; Hansen, S. H.; Møller, B. L.; Janfelt, C.; Bjarnholt, N. Visualizing metabolite distribution and enzymatic conversion in plant tissues by desorption electrospray ionization mass spectrometry imaging. *Plant J*. **2013**, *74*, 1059-1071.

(40) Hemalatha, R. G.; Pradeep, T. Understanding the molecular signatures in leaves and flowers by desorption electrospray ionization mass spectrometry (DESI MS) imaging. *J. Agricult. Food Chem.* **2013**, *61*, 7477-7487.

(41) de Abreu, L. B.; Augusti, R.; Schmidt, L.; Dressler, V. L.; de Moraes Flores, E. M.; Nascentes, C. C. Desorption electrospray ionization mass spectrometry (DESI-MS) applied to the speciation of arsenic compounds from fern leaves. *Anal. Bioanal. Chem.* **2013**, *405*, 7643-7651.

(42) Roach, P. J.; Laskin, J.; Laskin, A. Nanospray desorption electrospray ionization: an ambient method for liquid-extraction surface sampling in mass spectrometry. *Analyst* **2010**, *135*, 2233-2236.

(43) Laskin, J.; Heath, B. S.; Roach, P. J.; Cazares, L.; Semmes, O. J. Tissue imaging using nanospray desorption electrospray ionization mass spectrometry. *Anal. Chem.* **2012**, *84*, 141-148.

(44) Lanekoff, I.; Heath, B. S.; Liyu, A.; Thomas, M.; Carson, J. P.; Laskin, J. Automated platform for high-resolution tissue imaging using nanospray desorption electrospray ionization mass spectrometry. *Anal. Chem.* **2012**, *84*, 8351-8356.

(45) Laneko, I.; Thomas, M.; Laskin, J. Shotgun approach for quantitative imaging of phospholipids using nanospray desorption electrospray ionization mass spectrometry. *Anal. Chem*. **2014**, *86*, 1872-1880.

(46) Lanekoff, I.; Burnum-Johnson, K.; Thomas, M.; Short, J.; Carson, J. P.; Cha, J.; Dey, S. K.; Yang, P.; Conaway, M. C. P.; Laskin J. High-speed tandem mass spectrometric in situ imaging by nanospray desorption electrospray ionization mass spectrometry. *Anal. Chem*. **2013**, *85*, 9596-9603.

(47) Rath, C. M.; Alexandrov, T.; Higginbottom, S. K.; Song, J.; Milla, M. E.; Fischbach, M. A.; Sonnenburg, J. L.; Dorrestein, P. C. Molecular analysis of model gut microbiotas by imaging mass spectrometry and nanodesorption electrospray ionization reveals dietary metabolite transformations. *Anal. Chem*. **2012**, *84*, 9259-9267.

(48) Lanekoff, I.; Thomas, M.; Carson, J. P.; Smith, J. N.; Timchalk, C.; Laskin, J. Imaging nicotine in rat brain tissue by use of nanospray desorption electrospray ionization mass spectrometry. *Anal. Chem*. **2013**, 85, 882-889.

(49) Watrous, J.; Roach, P.; Alexandrov, T.; Heath, B. S.; Yang, J. Y.; Kersten, R. D.; van der Voort, M.; Pogliano, K.; Gross, H.; Raaijmakers, J. M.; Moore, B. S.; Laskin, J.; Bandeira, N.; Dorrestein, P. C. Mass spectral molecular networking of living microbial colonies. *Proc. Natl. Acad. Sci. U.S.A.* **2012**, *109*, E1743-E1752.

(50) Nguyen, D. D.; Wu, C.-H.; Moree, W. J.; Lamsa, A.; Medema, M. H.; Zhao, X.; Gavilan, R. G.; Aparicio, M.; Atencio, L.; Jackson, C.; Ballesteros, J.; Sanchez, J.; Watrous, J. D.; Phelan, V. V.; van de Wiel, C.; Kersten, R. D.; Mehnaz, S.; De Mot, R.; Shank, E. A.; Charusanti, P.; Nagarajan, H.; Duggan, B. M.; Moore, B. S.; Bandeira, N.; Palsson, B. Ø .; Pogliano, K.; Gutiérrez, M.; Dorrestein, P. C. MS/MS networking guided analysis of molecule and gene cluster families. *Proc. Natl. Acad. Sci. U.S.A.* **2013**, *110*, E2611-E2620.

(51) Traxler, M. F.; Watrous, J. D.; Alexandrov, T.; Dorrestein, P. C.; Kolter, R. Interspecies interactions stimulate diversification of the streptomyces coelicolor secreted metabolome. *mBio* **2013**, *4*, e00459-13.

(52) Watrous, J.; Roach, P.; Heath, B.; Alexandrov, T.; Laskin, J.; Dorrestein, P. C. Metabolic profiling directly from the Petri dish using nanospray desorption electrospray ionization imaging mass spectrometry. *Anal. Chem.* **2013**, *85*, 10385-10391.

(53) Kersten, R. D.; Yang, Y.-L.; Xu, Y.; Cimermancic, P.; Nam, S.-J.; Fenical, W.; Fischbach, M. A.; Moore, B. S.; Dorrestein, P. C. A mass spectrometry-guided genome mining approach for natural product peptidogenomics. *Nat. Chem. Biol.* **2011**, *7*, 794-802.

(54) Lanekoff, I.; Geydebrekht, O.; Pinchuk, G. E.; Konopka, A. E.; Laskin, J. Spatially resolved analysis of glycolipids and metabolites in living *Synechococcus sp* PCC 7002 using nanospray desorption electrospray ionization. *Analyst* **2013**, *138*, 1971-1978.

(55) Hsu, C.-C.; White, N. M.; Hayashi, M.; Lin, E. C.; Poon, T.; Banerjee, I.; Chen, J.; Pfaff, S. L.; Macagno, E. R.; Dorrestein, P. C. Microscopy ambient ionization top-down mass spectrometry reveals developmental patterning. *Proc. Natl. Acad. Sci. U.S.A.* 2013, *110*, 14855-14860.

(56) Oychinnikova, O. S.; Kjoller, K.; Hurst, G. B.; Pelletier, D. A.; Van Berkel, G. J. Atomic force microscope controlled topographical imaging and proximal probe thermal desorption/ionization mass spectrometry imaging. *Anal. Chem.* **2014**, *86*, 1083-1090.

(57) Liu, J.; Cooks, R. G.; Ouyang, Z. Biological tissue diagnostics using needle biopsy and spray ionization mass spectrometry. *Anal. Chem.* **2011**, *83*, 9221-9225.

(58) Yoshimura, K.; Mandal, M. K.; Hara, M.; Fujii, H.; Chen, L. C.; Tanabe, K.; Hiraoka, K.; Takeda, S. Real-time diagnosis of chemically induced hepatocellular carcinoma using a novel mass spectrometry-based technique. *Anal. Biochem.* **2013**, *441*, 32-37.

(59) Bojko, B.; Gorynski, K.; Gomez-Rios, G. A.; Knaak, J. M.; Machuca, T.; Cudjoe, E.; Spetzler, V. N.; Hsin, M.; Cypel, M.; Selzner, M.; Liu, M.; Keshjavee, S.; Pawliszyn, J. Low invasive in vivo tissue sampling for monitoring biomarkers and drugs during surgery. *Lab. Invest*. **2014**, *94*, 586-594.

(60) Wang, H.; Manicke, N. E.; Yang, Q.; Zheng, L.; Shi, R.; Cooks, R. G.; Zheng, O. Direct analysis of biological tissue by paper spray mass spectrometry. *Anal. Chem.* **2011**, *83*, 1197-1201.

(61) Peng, Y. E.; Zhang, S. C.; Wen, F.; Ma, X. X.; Yang, C. D.; Zhang, X. R. In vivo nanoelectrospray for the localization of bioactive molecules in plants by mass spectrometry. *Anal. Chem.* **2012**, *84*, 3058-3062.

(62) Zhang, H.; Gu, H.; Yan, F.; Wang, N.; Wei, Y.; Xu, J.; Chen, H. Direct characterization of bulk samples by internal extractive electrospray ionization mass spectrometry. *Sci. Rep*. **2013**, *3*, 2495.

(63) Bennett, R. V.; Morzan, E. M.; Huckaby, J. O.; Monge, M. E.; Christensen, H. I.; Fernández, F. M. Robotic plasma probe ionization mass spectrometry (RoPPI-MS) of non-planar surfaces. *Analyst* **2014**, *139*, 2658-2662.

(64) Hsu, C.-C.; ElNaggar, M. S.; Peng, Y.; Fang, J.; Sanchez, L. M.; Mascuch, S. J.; Moller, K. A.; Alazzeh, E. K.; Pikula, J.; Quinn, R. A.; Zeng, Y.; Wolfe, B. E.; Dutton, R. J.; Gerwick, L.; Zhang, L.; Liu, X.; Månsson, M.; Dorrestein, P. C. Real-time metabolomics on living microorganisms using ambient electrospray ionization flow-probe. *Anal. Chem.* **2013**, *85*, 7014-7018.

(65) Luo, Z; He, J.; Chen, Y.; He, J.; Gong, T.; Tang, F.; Wang, X.; Zhang, R.; Huang, L.; Zhang, L.; Lv, H.; Ma, S.; Fu, Z.; Chen, X.; Yu, S.; Abliz, Z. Air flow-assisted ionization imaging mass spectrometry method for easy whole-body molecular imaging under ambient conditions. *Anal. Chem.* **2013**, *85*, 2977-2982.

(66) Chen, C.-H.; Lin, Z.; Garimella, S.; Zheng, L.; Shi, R.; Cooks, R. G.; Ouyang, Z. Development of a mass spectrometry sampling probe for chemical analysis in surgical and endoscopic procedures. *Anal. Chem.* **2013**, *85*, 11843-11850.

(67) Balog, J.; Szaniszlo, T.; Schaefer, K.-C.; Denes, J.; Lopata, A.; Godorhazy, L.; Szalay, D.; Balogh, L.; Sasi-Szabo, L.; Toth, M.; Takats, Z. Identification of biological tissues by rapid evaporative ionization mass spectrometry. *Anal. Chem.* **2010**, *82*, 7343-7350.

(68) Balog, J.; Sasi-Szabo, L.; Kinross, J.; Lewis, M. R.; Muirhead, L. J.; Veselkov, K.; Mirnezami, R.; Dezso, B.; Damjanovich, L.; Darzi, A,; Nicholson, J. K.; Takáts, Z. Intraoperative tissue identification using rapid evaporative ionization mass spectrometry. *Sci. Trans. Med.* **2013**, *5*, 194ra93.

(69) Strittmatter, N.; Jones, E. A.; Veselkov, K. A.; Rebec, M.; Bundy, J. G.; Takats, Z. Analysis of intact bacteria using rapid evaporative ionisation mass spectrometry. *Chem. Commun*. **2013**, *49*, 6188-6190.

(70) Strittmatter, N.; Rebec, M.; Jones, E. A.; Golf, O. M. H.; Abdolrasouli, A.; Balog, J.; Behrends, V. D.; Veselkov, K. A.; Takats, Z. Rapid characterization and identification of clinically relevant microorganisms using rapid evaporative ionization mass spectrometry. *Anal. Chem.* **2014**, DOI: 10.1021/ac501075f.

(71) Gross, J. H. Direct analysis in real time-a critical review on DART-MS. *Anal. Bioanal. Chem.* **2014**, *406*, 63-80.

(72) Venter, A. R.; Douglass, K. A.; Shelley, J. T.; Hasman, G. Jr., Honarvar, E. Mechanisms of real-time, proximal sample processing during ambient ionization mass spectrometry. *Anal. Chem.* **2014**, *86*, 233-249.

(73) Monge, M. E.; Harris, G. A.; Dwivedi, P.; Fernandez, F. M. Mass spectrometry: recent advances in direct open air surface sampling/ionization. *Chem. Rev.* **2013**, *113*, 2269-2308.

Chapter 1 is a modified reprint of the material as it appears in the manuscript of the perspective article invited for publication in Current Opinion in Biotechnology: Analytical Biotechnology 2014 by Cheng-Chih Hsu and Pieter C. Dorrestein. The thesis author is the primary author of the article.

Chapter 2

Microscopy Ambient Ionization Top-Down Mass Spectrometry Reveals Developmental Patterning

2.1 Abstract

In this chapter we demonstrate the utility of integrating an inverted light microscope with an ambient ionization source—nanospray electrospray desorption ionization—attached to a high-resolution mass spectrometer to define the proteome and metabolom with unprecedented resolution in embryonic tissues. Via the top-down mass spectrometry analysis, we characterized the molecular composition of wild type and developing mouse spinal cords adjacent non-neuronal tissues, and readily detected a broad range of molecules including peptides and proteins, as well as metabolites such as lipids, sugars, and other small molecules including *S*-adenosyl methionine and glutathione. Top-down analysis revealed variation in the expression of hemoglobin, including the transition from fetal to adult hemoglobin and heterogeneity in hemoglobin subunits consistent with genetic diversity of the mouse models. Similarly, temporal changes to actin-sequestering proteins β-thymosins during development were observed. These results demonstrate that interfacing microscopy with atmospheric ionization

provides the means to perform targeted *in situ* ambient top-down mass spectral analysis to study and explore the molecular pattern of proteins, lipids, and sugars in biologically heterogeneous samples.

2.2 Introduction

Light microscopy has been instrumental to understanding biological processes such as embryonic development by providing insight into the temporal and spatial arrangements of cells within a tissue, but it provides limited molecular information. Mass spectrometry (MS), in contrast, can provide detailed molecular information. However, if one aims to understand biology at multiple levels of organization, from molecules to organelles and eventually entire organisms, methods that can bridge these levels and surpass the limitations of current techniques need to be developed. Most methods in biology examine a limited number of molecules at a time. As the need for system-wide analysis is emerging so is the need for tools that can capture a wide range of chemistry. For example, immunohistochemistry yields excellent sub-cellular resolution of the distribution of the recognized antigen, but its applicability is limited mostly to certain peptides and proteins.[1] Moreover, the usefulness of this technique is constrained to those proteins for which accurate and selective antibodies have been developed. By comparison, MS-based approaches, in particular MALDI-TOF imaging mass spectrometry (IMS), have demonstrated their capacity to explore the molecular nature of biology by integrating the chemistry of samples with their biology in a spatial manner.[2-5] The quality of the spectra in MALDI-TOF imaging is dependent on very even and reproducible crystalline matrix deposition that limits transparency and therefore the use of

simultaneous microscopic analysis. A MALDI-TOF-MS has been built with a microscope where one can collect MALDI and microscopy on the same sample. The design includes a stage where the topographic data is first collected by microscopy and then the stage is moved into position for MALDI-MS data collection, thereby disconnecting the microscopy step from mass spectrometric analysis even though they are present in the same instrument.[5] In addition, the ease of obtaining and the quality of MALDI-TOF based fragmentation, usually via post-source decay or a derivative thereof, has yet to be improved compared to collision-induced fragmentation. Information rich fragmentation information is critical for the identification of the molecules, which provides insight into the biology under investigation.

Although other ambient methods exist that can be interfaced with imaging modalities such as a laser ablation/dissection and atomic force microscopy,[6,7] electrospray ionization (ESI) MS added an alternative powerful tool to the system-level exploration of biological questions particularly in terms of proteomics and atmospheric analysis.[8-12] Recently, several ESI-based ambient ionization MS techniques are developed--including desorption electrospray ionization (DESI) and nanospray desorption electrospray ionization (nanoDESI)—each of which has been adapted to perform IMS.[13-16] Of these ambient ionization methods, nanoDESI has a spatial resolution down to 12 μm and superb MS spectral resolution with good mass accuracy when combined with high-resolution spectrometry.[15,16] High mass accuracy and spectral resolving power are essential for accurately identifying the signals of biomolecules, a particularly difficult task in the case of large biomolecules. NanoDESI operates at ambient pressure and temperature, does not require a sensitive tissue preparation protocol,

and has an uncomplicated instrumental setup that works at multiple angles, all of which make it an appropriate technique to integrate with light microscopes commonly used in biological studies while maintaining high sensitivity. Here we present our hybrid design that integrates the nanoDESI ion source with a hybrid ion trap quadrupole Fourier transform ion cyclotron resonance (LTQ-FT-ICR) mass spectrometer and an inverted light microscope into a single platform. The design is shown in Figure 2.1 and online supplementary video (https://www.youtube.com/watch?v=D9UHpL3cVVM). For ease of discussion, we will refer to the design described in this paper as AMM for ambient ionization interfaced with a microscope and mass spectrometry.

2.3 Design of NanoDESI-Microscope Setup

The schematic setup of AMM is shown as Figure 2.1. It is composed of two parts: an inverted light microscope and nanoDESI. The transmitted optical images of the tissue were taken by the inverted microscope (Nikon DIAPHOT 300) via the illumination of the tungsten lamp. The photons were collected by the object lenses and split into a CCD camera (Nikon D40 DSLR) to take digital images before the start of experiments. A xenon arc lamp and fluorescence filter cube turrets were used for fluorescence images. NanoDESI was set-up on the same x-y movable platform that was used to position the microscope. The fused silica capillary tubes of the nanoDESI were mounted on the independent x-y-z linear actuator (A1) for accurate alignment. To make the illuminating light pass through, the two capillary tubes were properly angled (~45 degree) and the plane into which the two capillaries are embedded was tilted (~45 degree). The conjunct terminals of the two capillary tubes were flame-pulled to shrink the size of the capillary

to ~40 μm (outer diameter). The sample was placed steady on a z-axis actuator, which is fixed onto the x-y stage of the Nikon microscope that was used to adjust the coordinate of the sample (relative to the nanoDESI liquid junction). The plane of the sample section was perpendicular to the focal axis of the object lenses (central axis). The solvent used is a 65/35 (v/v) acetonitrile/0.05% formic acid aqueous solution, which is used to extract polar compounds. The relative location of the secondary capillary outlet to the extended MS (hybrid 6.4T LTQ-FT, Thermo Electron, North America) ion inlet was adjusted by AMM platform and A1 for optimal ESI performance. All spectra were acquired in the positive-ion mode with 2.0 kV spray voltage. Once the ESI current was formed, the position of the nanoDESI capillary tubes was fixed. A liquid junction was sustained throughout the experiment and was positioned at the central axis. To avoid scattering from the fused silica capillary tubes and sample loss via liquid extraction, the tissue sample was lowered 5 mm underneath the liquid junction at the "microscopy mode". The target tissue was aligned (x-y) to the central z-axis before switching to the “MS mode”, at which the surface of the sample was approximated along the z direction to the capillary tube junction to mobilize the molecules on the sample surface. Total ion intensity started to rise within 10 seconds after the liquid made contact. The flow rate of the carrier solvent was tuned to match the self-aspiration rate of the secondary capillary (typically 0.8-2.0 μl/min) so the droplet spread-out size was limited to 100 μm.

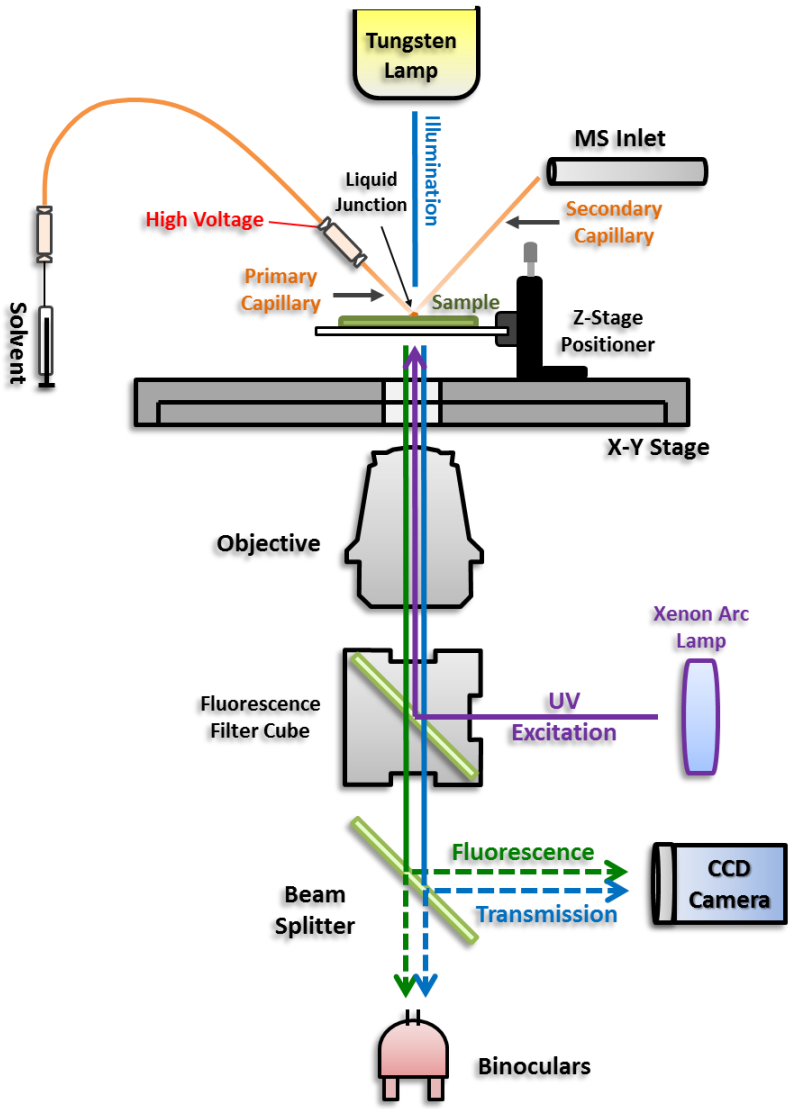

Figure 2.1 Schematic overview of how targeted microscopy based nanoDESI works. The light microscope is a modified Nikon DIAPHOT 300 inverted fluorescence microscope. A home-built nanoDESI setup similar to that introduced in reference 53 is integrated with the inverted microscope to perform *in situ* mass spectrometry analysis. Thawed tissue sections on standard (1x3 inch) glass slides are positioned on a z-axis drive, which is fixed onto the x-y stage of the inverted microscope that is used to adjust the coordinate of the sample (relative to the nanoDESI liquid junction). The specimen is then moved under the liquid junction produced by the sampling capillaries, so that the target sample region is directly underneath as judged visually through the microscope, and desorbed molecules are aspirated into the secondary capillary. The ions in the electrospray process are generated at the terminal end of the secondary capillary, where the solvent is infused.

2.4 Result and Discussion

2.4.1 Tandem Mass Analysis of Compounds on E15.5 Mouse

The results that can be obtained with this hybrid instrument were first assayed using frozen mouse tissue sections. Previously, using MALDI-IMS and DESI, the molecular profiles during embryo development were performed on the tissue sections or pre-implantation embryos.[17-20] In an attempt to investigate the early development of the central nervous system (CNS), a mouse embryo was flash-frozen and sectioned at day 15.5 after fertilization (E15.5) at the lumbar level of the developing spinal cord. Starting from a transmitted light image of the preparation positioned on the microscope, the spinal cord cross-section and adjacent structures were outlined and mass spectra obtained at locations of interests as depicted in Figure 2.2. Spectra in the range of *m/z* 200-2000 were obtained by FT-ICR-MS, with 50,000 resolving power. Three spectra, taken along the dorsoventral axis at locations 1, 2 and 3 noted on the histological image (Figure 2.2c), are shown side-by-side on the upper left (Figure 2.2a). Within the selected *m/z* range from ~685 to 850 *m/z*, various classes of biomolecules were identified in each spectrum. Significantly different relative abundances were observed for several proteins at the selected locations (the process of identification of these proteins and molecules is described below and in the Supporting Information).

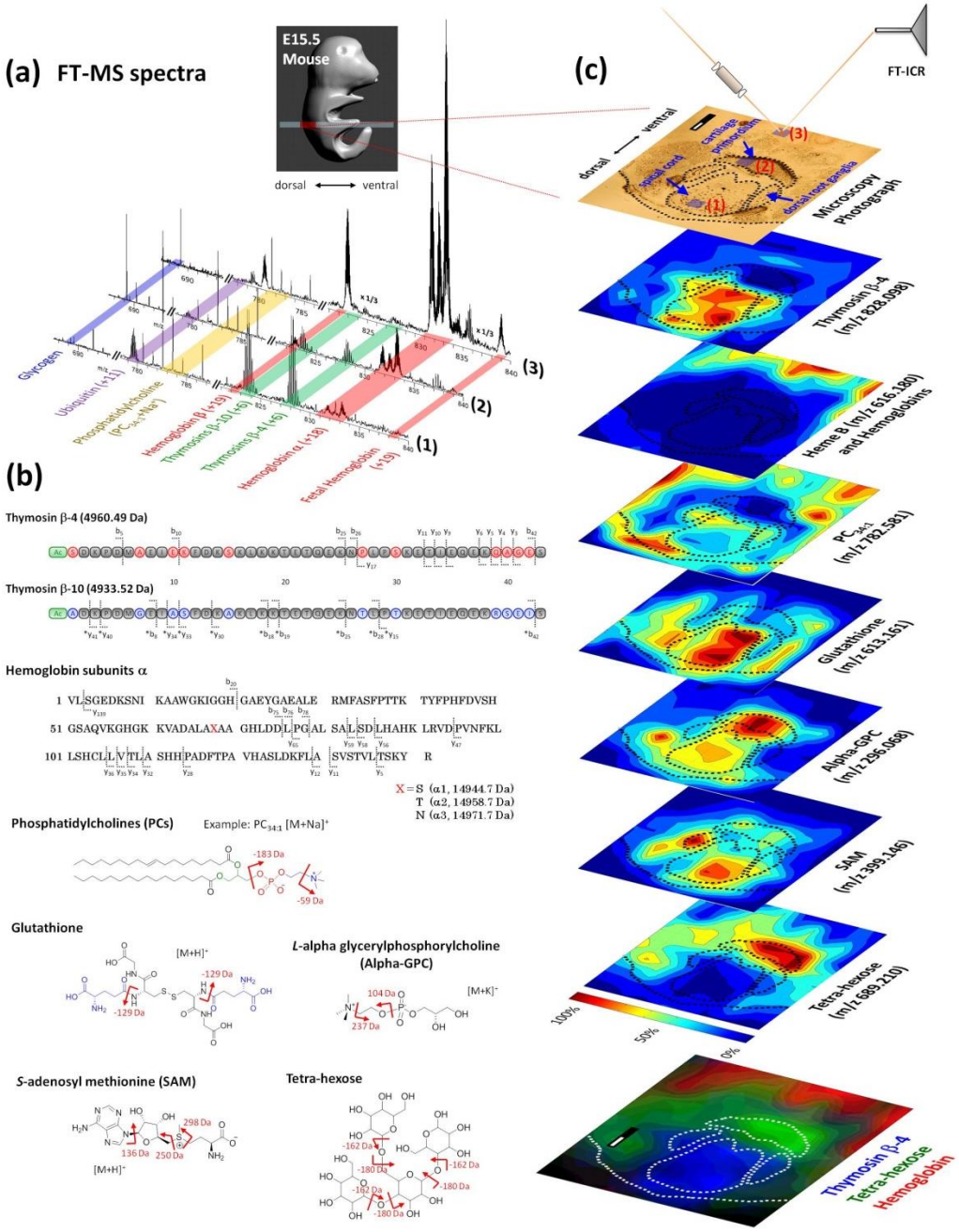

Figure 2.2 AMM of an E15.5 mouse spinal cord section in the lumbar region. (a) High resolution FT-MS spectra in the 685-850 *m/z* range, taken at the locations specified by the blue squares depicted on the micrograph at top right along the dorsoventral axis: (1) dorsal region of the spinal cord, (2) the cartilage primordium, and (3) the ventral body cavity. The regions of interest are outlined by the dotted lines. (b) Representative molecules, with molecular weights ranging from a few hundred Da to 15 kDa, are annotated via top-down tandem mass analysis (see Supporting Information for MS/MS spectra). (c) Abundance contour maps reconstructed from a raster for several of the identified molecules. Scale bar: 200 μm.

Indeed, high levels of the ions of two intact β-thymosins, thymosin β-10 (Tβ-10, 4933.51 Da; 823.594 *m/z*, charge +6) and thymosin β-4 (Tβ-4, 4960.48 Da; 828.098 *m/z*, charge +6) were observed in the spinal cord (Figure 2.2a, spectrum (1)), but were not detected in the body cavity (Figure 2.2a, spectrum (3)). A similar relative distribution was observed for ubiquitin (8559.64 Da; 779.612 *m/z*, charge +11). A contrasting distribution pattern was observed for hemoglobin, which was more abundant at location 3, in the body cavity, than at location 1 in the spinal cord. Signals of monomeric hemoglobin α (14944.7-14971.7 Da) and β (15607.1 Da) subunits predominated in the body cavity, which is rich in blood vessels in the E15.5 mouse embryo. The characterization of all proteins was determined by *in situ* top-down analysis using ProSight PTM as shown in Figure 2.2b and Supporting Information.[21-27]

To support the annotation of Tβ-4 determined by top down mass spectrometric analysis, we looked for Tβ-4 protein in a previously described global Tβ-4 knockout mouse.[28] The FT-MS spectra (Figure 2.3) indicated Tβ-4 was not present in the Tβ-4 knockout, while the Tβ-10 peaks were detected in both the wild-type (WT) and Tβ-4 knockout samples. This was further supported by immunohistochemistry (Figure 2.22). This highlights the accuracy and sensitivity of this targeted microscopy MS interface. It also introduces the possibility that this technique could be used to identify a proteinaceous phenotype in genotypic mutants that display no obvious behavioral or cell-biological phenotypes.

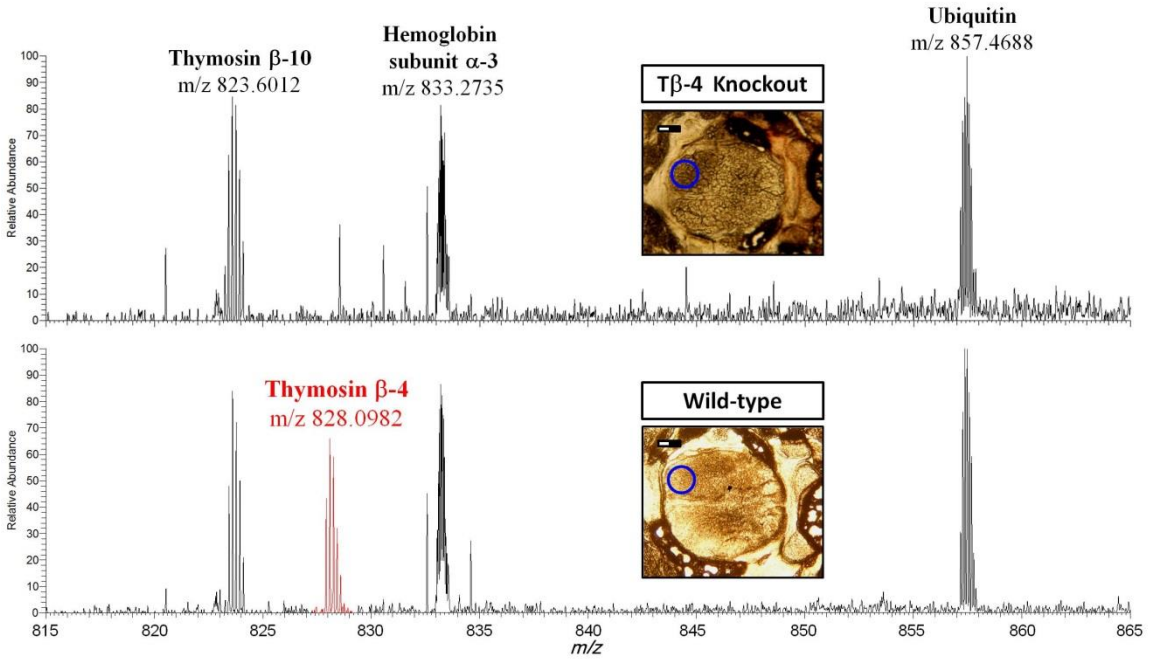

Figure 2.3 Targeted AMM analysis of thymosin β-4 knockout mouse tissue sections. FT-MS spectrum and microscope photographs of *in situ* Tβ-4 knockout (upper) and wild-type (lower) P2 mice using AMM. Spectra were collected on the spinal cords near the dorsal end as indicated by the blue circles (scale bar: 200 μm). The absence of the m/z 828.0982 ion clusters in the knockout mouse verifies its annotation of Tβ-4 via the top-down approach.

In addition to proteins, metabolites were also detected. Detected metabolites (Figure 2.2b) were compared to metabolomic databases such as METLIN[29] and Massbank.[30] Phospholipids, the major component of cell membranes, such as phosphatidylcholine $PC_{34:1}$ (782.581 *m/z*, Na^+ adduct) and others with variable lipid chain lengths, were found throughout the sample, but the signal was significantly weaker in the cartilage primordium of the lumbar spine (we will refer to this as the cartilage primordium). In the lower *m/z* region, some of the critical small metabolites such as glutathione (613.161 *m/z*), *S*-adenosyl methionine (399.146 *m/z*) and *L*-alpha glycerylphosphorylcholine (Alpha-GPC, 296.068 *m/z*) were also observed in the spinal cord (Figure 2.4 and Supporting Information for MS/MS spectra).

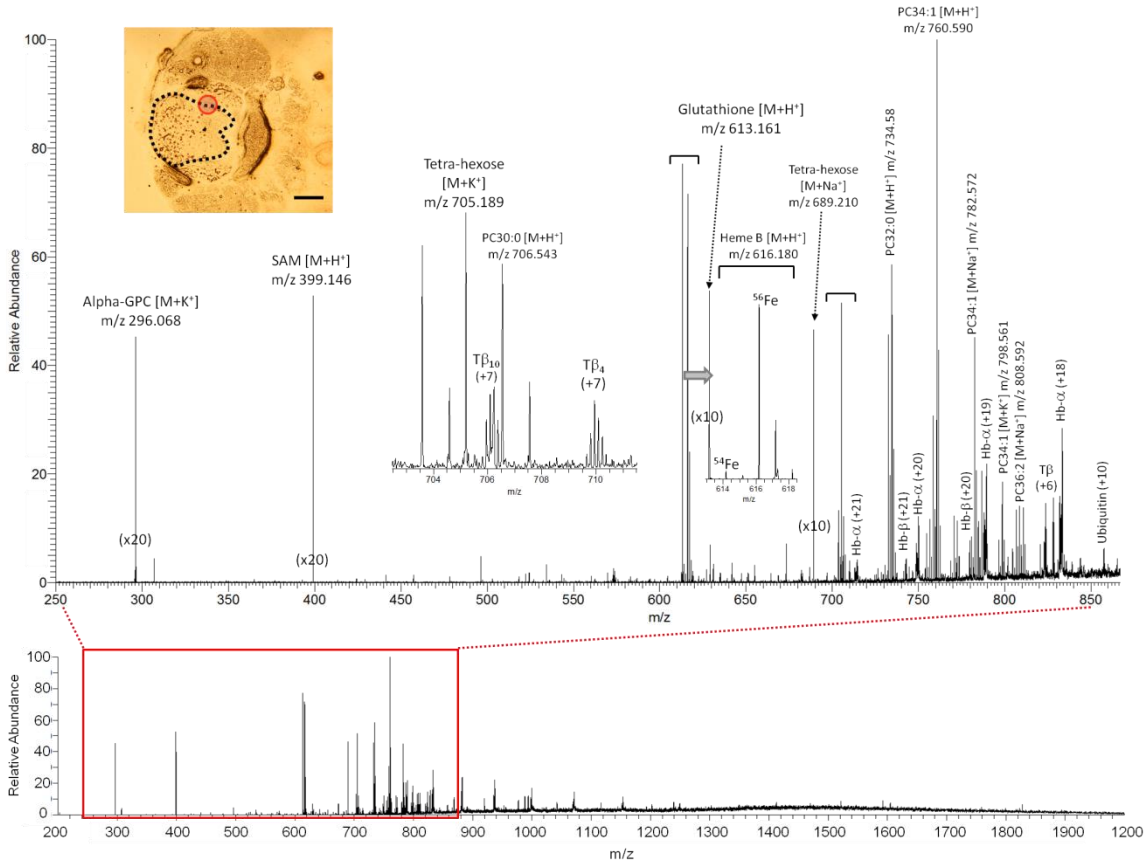

Figure 2.4. FT-MS spectrum of *in situ* E15.5 mouse using AMM. Spectrum was collected on the spinal cord near the dorsal root ganglia as indicated by the red circle (scale bar: 200 μm). The tandem mass analysis of the annotated ions is elaborated in Figure 2.7-21).

2.4.2 Fetal-to-Adult Hemoglobin Ontogeny

The transition of hemoglobin from embryonic protein isoforms, known as fetal hemoglobin, to adult isoforms, is typically assayed by gel electrophoresis.[31-33] Fetal hemoglobin binds oxygen with greater affinity than does adult hemoglobin, which allows the former to compete effectively for oxygen with adult hemoglobin in the placental blood. High mRNA expression of mouse β-like fetal hemoglobin such as εy and βH1 has been reported at early embryonic stages.[34] Given this known transition, we investigate the

ontogeny of hemoglobin isoforms during fetal and postnatal development (E12.5 to P10), and in the adult, using *in situ* top-down MS analysis to determine whether AMM is able to capture this by targeting the blood vessels adjacent to the spinal cord (Supplementary Video could be found online: https://www.youtube.com/watch?v=D9UHpL3cVVM).

Using AMM, the monomeric hemoglobin subunits, including the fetal β-like globins, were readily observed as shown in Figure 2.5. No intact tetrameric hemoglobin ($\alpha_2\beta_2$) was observed, since the acid-induced ferrihemoglobin disassembly and heme (616.180 *m/z*, Figure 2.21) dissociation took place within sub-second intervals during real-time extraction from the tissue surface.[35] As expected, the α subunits were observed at all time points, and the embryonic β-like hemoglobin ε-Y2 subunit (16004.4 Da) was found in all prenatal stages and disappeared at 2 days after birth (postnatal day2; P2). In addition, the β subunits were detected beginning at E13.5 (very low level compared with the other fetal hemoglobin at E12.5) when they co-existed with ε-Y2. After gestation, the adult β globin became the predominant form of β-like globin chains. Another fetal β-like globin, βH1 (16352.6 Da), was also found on the E13.5 and E14.5 tissues, but it was not detected after E15.5. Our observation of high level ε-Y2 and βH1 β-like hemoglobin in the prenatal stages is consistent with the transition from fetal hemoglobin ($\alpha_2\varepsilon_2$ and $\alpha_2\beta h_2$), to adult hemoglobin ($\alpha_2\beta_2$) reported previously.[34]

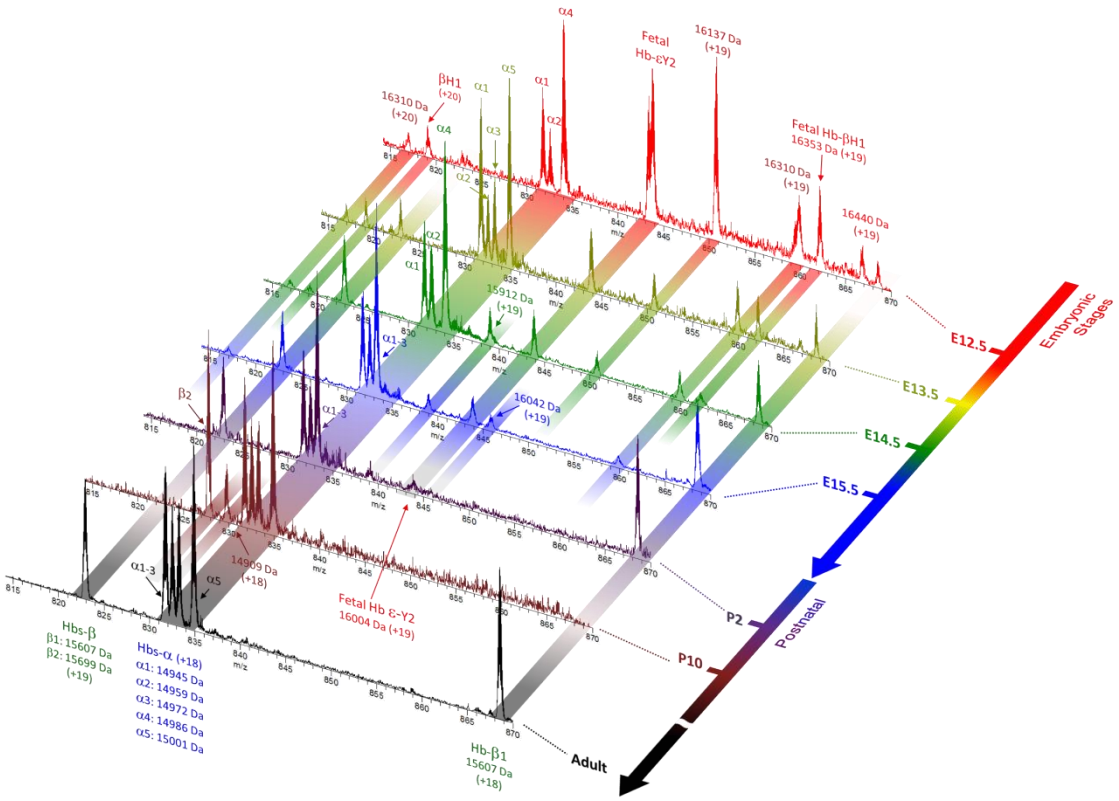

Figure 2.5 Mouse hemoglobin expression during development characterized by AMM. All of the FT-MS spectra were taken by targeted analysis of the blood vessel-rich regions of the tissue sections near the spinal cord. The data show that the variety of hemoglobin subtypes and isoforms over time can be captured using this approach. Proteins that were not identified by top-down analysis are labeled by the corresponding monoisotopic masses and charge states (in parentheses). Heterogeneity of adult α and β hemoglobin isoforms (e.g., absence of α4 in E13.5 and α5 in E12.5; β2 instead of β1 in P10) results from the genetic diversity inherent in the parental background strains which is then passed to their offspring. Replicates of E12.5-P2 using different mice are displayed in supporting information Figure 2.26.

In addition to capturing the developmental transition from fetal-to-adult hemoglobin at the earlier time points, we also observed a heterogeneity of some documented adult α and β hemoglobin proteoforms, e.g., α1: 14944.7 Da, α2: 14958.7 Da, α3: 14971.7 Da, α4: 14985.7 Da, α5: 15000.7 Da; and β1: 15607.1 Da, β2: 15699.1 Da.[36-38] Many factors might be responsible for this heterogeneity. "Extrinsic" factors such

as transcriptional regulation of globin genes (α, β, ε, etc.) during fetal-to-adult development is well established, however, not to a sufficient level of detail to explain the regulation within each globin family, e.g. α1-α5.[32] Recently, a report showed that adult hemoglobin subunit pairs have higher bonding strengths, and this variation on the affinity affects the hemoglobin regulation during development.[33] This "intrinsic" factor may suggest that post-transcriptional regulation could cause one subunit to be more rapidly degraded at one point in development by virtue of forming weaker interfaces with other subunits. However, this shift of those documented adult hemoglobin might not be a result of neither regulatory factors during development, but only the genetic diversity inherent in the parental background strains that is passed to the offspring.[36-38] A prominent example is the α-hemoglobin heterogeneity on different mice at the same embryonic stage. As can be found in the supporting information (Figure 2.26), some P2 mice express only α-3 globin while others express α-1 to α-3. In short, this is a direct result of classical Mendelian genetics that affect hair color, the color of the eyes and in this case the detected phenotype is the diversification of the observed molecular phenotype, the hemoglobin proteoforms observed in the offspring when two parents mate.

The annotations of the hemoglobin ions were verified by matching *y* and *b* ions using the top-down approach with ProSight PTM (Figure 2.7-12). Some other low-intensity ions that represent masses of ~16 kDa were observed during the fetal period. These may yet represent other globins important during development, but were not of sufficient abundance to get fragmentation information. These results highlight how top-down ambient mass spectrometric analysis can identify protein isoforms with sufficient

specificity to provide valuable insight into the role distinct isoforms play in localized and temporally-specific biological processes.

Table 2.1 Hemoglobin subtype ontogeny (data in **Figure 2.5**) using top-down mass spectrometry analysis*

	Subtype	Neutral Monoisotopic Mass (Da)	E12.5	E13.5	E14.5	E15.5	P2	P10	Adult	MS/MS Validation
α-like	α-1	14944.7	+	+	+	+	+	+	+	Yes
	α-2	14958.7	+	+	+	+	+	+	+	Yes
	α-3	14971.7	-	+	-	+	+	+	+	Yes
	α-4	14985.7	+	-	+	-	-	-	-	No
	α-5	15000.8	-	+	-	-	-	+	+	Yes
β-like	β-1	15607.1	low	+	+	+	+	-	+	Yes
	β-2	15699.1	-	-	-	-	-	+	-	Yes
	ε-Y2	16004.4	+	+	+	+	-	-	-	Yes
	βH1	16352.7	-	+	+	-	-	-	-	No
Not identified		16310.6	+	+	+	+	-	-	-	No
		16137.3	+	+	+	-	-	-	-	No
		16440.5	+	-	-	-	-	-	-	No
		15912.1	-	-	+	+	-	-	-	No
		16042.5	-	-	-	+	-	-	-	No
		14909.5	-	-	-	-	-	+	-	No

* Additional data using different mice sections are shown in Figure 2.26. Expressions within the same globin families (α and β) are subject to change as a result of genetic diversity.[36-38]

2.4.3 Molecular Histology and Dorsoventral Pattern

Having demonstrated that the interface of nanoDESI with light microscopy can capture molecular changes during embryonic development with top-down MS, we proceeded to use this approach to measure the spatial distribution of specific molecules in the spinal cord. Using the microscope to position the nanoDESI probe for data collection, FT-MS spectra were collected from the E15.5 tissue in a raster at locations spaced ~160 μm apart from each other. Representative molecular contour maps of individual ions

were plotted in a color scale representing the relative intensity of the specific *m/z* (Figure 2.2c). It is notable that no significant protein signals above the detection limit were found on the cartilage primordium; however, a great amount of tetra-hexose (689.210 *m/z*), based on our interpretation of the tandem mass spectra (Figure 2.17), was detected near the cartilage primordium. As expected, hemoglobin ions were absent from this area, given that cartilage is devoid of blood vessels. The two β-thymosins, as well as small metabolites such as glutathione and Alpha-GPC, all showed slight but consistent dorsoventral asymmetric distributions in the spinal cord. One of the molecules that displayed this asymmetry was SAM, a metabolite known to affect transcriptional regulation through histone methylation.[39,40] The limit of detection of β-thymosins is at sub-femtomole (Figure 2.24). Although at this point only abundant proteins were observed, our result demonstrates that endogenous proteins can be resolved and characterized via top-down analysis directly from a tissue surface using ambient MS.

The β-thymosin isoforms Tβ-4 and Tβ-10 are both abundant in the developing CNS, as well as in proliferating tumor cells, and can be regulated by cell fate regulators such as retinoic acid.[41-44] β-thymosins are highly conserved polypeptides that act as actin-sequestering molecules and regulate the polymerization of G (globular) actin to form F (filamentous) actin.[45-47] Altered expression of β-thymosins is strongly associated with various important biological activities, especially tissue repair and regeneration.[42,43] Given the significant developmental transitions in hemoglobin isoforms, we sought to explore whether such changes were also associated with key β-thymosins. Our spatiotemporal results indicate that from early embryonic stages to postnatal day 10 (P10)

both Tβ-4 and Tβ-10 are detected in and near the spinal cord (Figure 2.6). At the earliest embryonic stage studied (E12.5), the distributions of Tβ-4 and Tβ-10 both display dorsally-low to ventrally-high concentration gradients, with increased levels around the notochord. Similar concentration gradients were also found at E13.5 for both Tβ-4 and Tβ-10, but at and after E15.5 the signals for both thymosins on the cartilage primordium diminish. At stages later than E12.5, the ions for β-thymosins become more intense within the spinal cord.

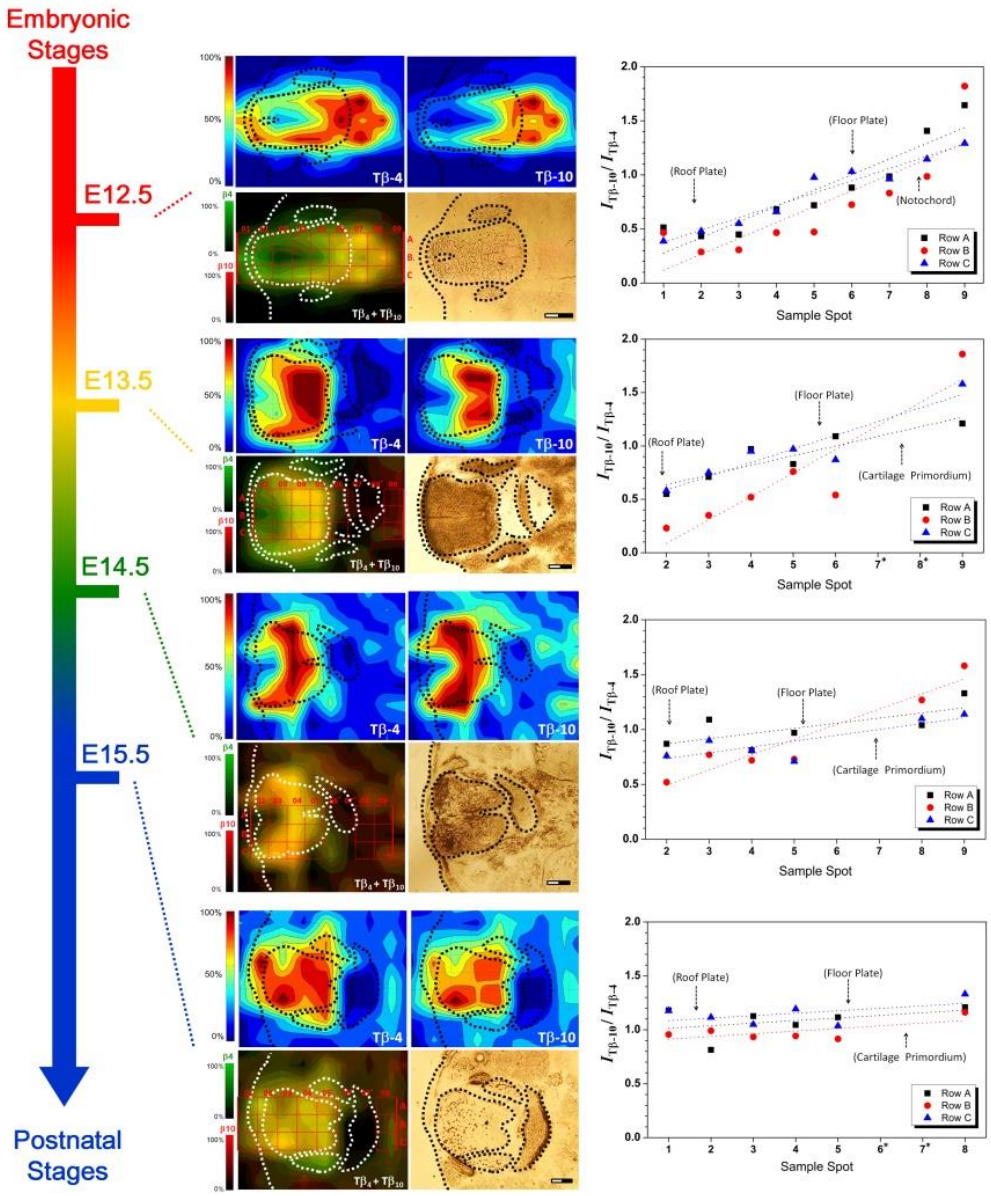

Figure 2.6 Contour maps of thymosin β-4 and β-10 in spinal cord sections during embryonic development and the transition from prenatal to adult mice. *Upper panels*: molecular contour maps of Tβ-4 (upper left, rainbow scale), Tβ-10 (upper right, rainbow scale), overlays of both (lower right, Tβ-4: green, Tβ-10: red) and transparent photographs at the indicated embryonic stages taken with the microscope on the lower left. The dashed lines represent histological outlines. The red grids indicate the sample spots at which the ion intensity ratios of Tβ-10/Tβ-4 were plotted along the dorsoventral axes that are shown on the right side of this figure. Because very low β-thymosins signal were detected on the cartilage primordium (prenatal) and vertebrae (postnatal) starting at E13.5, ratios of those sampling spots were not presented. The lines indicate the general ratio trend observed in the data. Scale bar: 200 μm. Replicates of E12.5-P2 are displayed in supporting information Figure 2.25.

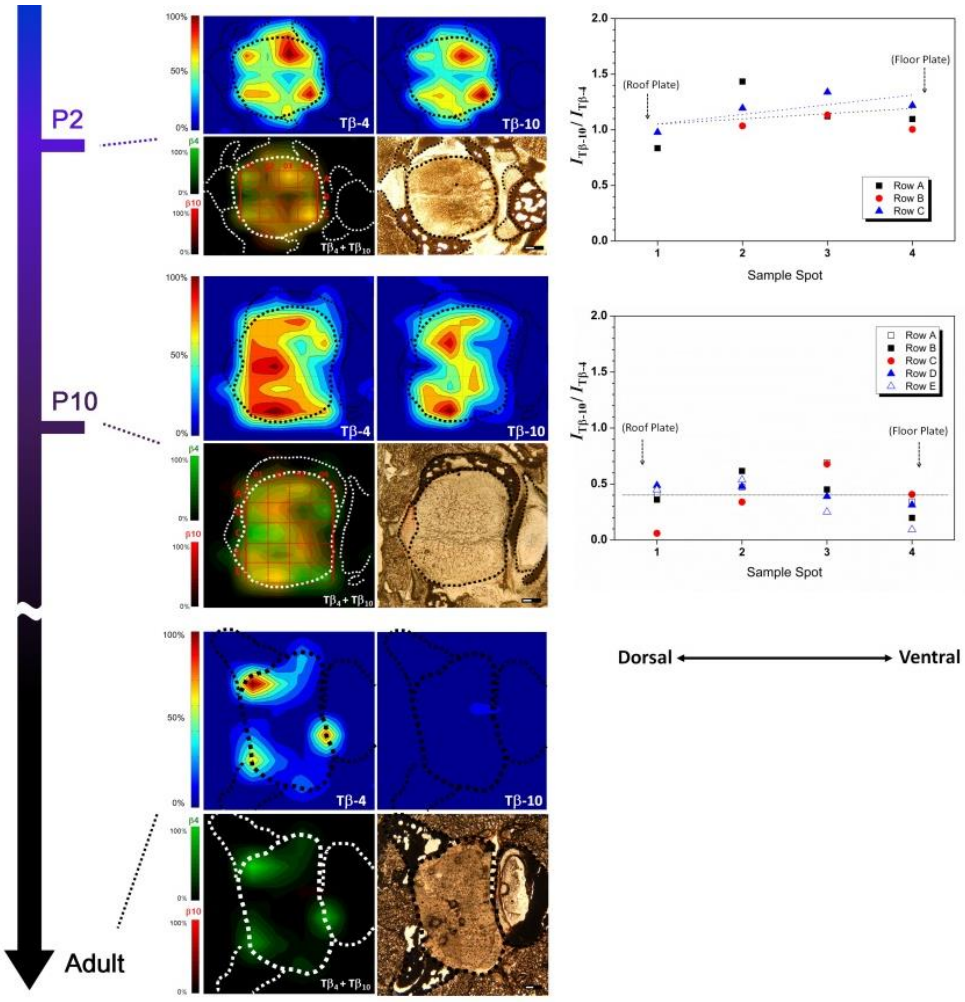

Figure 2.6 Contour maps of thymosin β-4 and β-10 in spinal cord sections during embryonic development and the transition from prenatal to adult mice. (*Continued*) *Upper panels*: molecular contour maps of Tβ-4 (upper left, rainbow scale), Tβ-10 (upper right, rainbow scale), overlays of both (lower right, Tβ-4: green, Tβ-10: red) and transparent photographs at the indicated embryonic stages taken with the microscope on the lower left. The dashed lines represent histological outlines. The red grids indicate the sample spots at which the ion intensity ratios of Tβ-10/Tβ-4 were plotted along the dorsoventral axes that are shown on the right side of this figure. Because very low β-thymosins signal were detected on the cartilage primordium (prenatal) and vertebrae (postnatal) starting at E13.5, ratios of those sampling spots were not presented. The lines indicate the general ratio trend observed in the data. Scale bar: 200 μm. Replicates of E12.5-P2 are displayed in supporting information Figure 2.25.

The data suggests that Tβ-10 is depleted more rapidly than Tβ-4 during embryogenesis. To ensure this is not an artifact of ionization, an instrumental response plot using synthetic β-thymosin standards was obtained (Figure 2.24). The ion intensity ratio of Tβ10-to-Tβ4 (γ) had a linear relationship to the relative amount of the two β-thymosins using the AMM and indicated there was no ionization bias when the two thymosins were compared. Based on this result, we proceeded to investigate the relative spatiotemporal features of the two β-thymosins. A linear trend of γ at E12.5 (Figure 2.6) revealed a gradient along the dorsoventral axis, high near the notochord (γ ~1.6) and low near the roof plate (γ = 0.4). At six days before birth (E13.5), a similar dorsoventral gradient of γ values persisted in the spinal cord, but the gradients became less significant starting from E14.5. Then at E15.5 and P2 the γ values of all sampling point throughout the spinal cord approached ~1.0. After birth the relative amount of Tβ-10 decreased and became completely undetectable with AMM in the adult spinal cord. Compared to Tβ-4, Tβ-10 levels dropped significantly within ten days after birth as shown by the low γ plot at P10. This rapid decrease relative to Tβ-4 is consistent with the drop observed in the developing brain at postnatal stages.[41] Thus, AMM reveals gradients of molecules in the spinal cord during embryonic development. Such gradients have not been reported for β-thymosins or any of the other molecules that were detected such as SAM or glutathione. Many morphogens, such as sonic hedgehog, display concentration gradients during embryonic development and are thought to determine cell fate via transcriptional regulation.[48-52] Based on the initial data obtained with AMM, we hypothesize that the

regulation of β-thymosins plays a role in embryonic spinal cord development perhaps through binding of G-actin.[41,45]

2.4.4 Conclusion and Significance

In conclusion, we propose that the nanoDESI-microscope MS interface, a new approach that provides targeted molecular information, can be used to reveal molecular changes over time and space, genotypic information and subtle molecular phenotypes in real-time. Three major accomplishments are describe in this chapter: **(1)** How we design an interface of a light microscope with ambient ionization mass spectrometry to perform *in situ* mass spectrometric analysis directly on tissue surfaces. **(2)** How we characterized endogenous biomolecules, whose molecular weights ranging from ~300 Da to 16 kDa, using top-down analysis on embryonic mice spinal cords. **(3)** How this novel design can be applied to investigate the developmental patterning of fetal and neonatal mice at molecular level in spatial and temporal manners. Although in this work AMM is only applied to study the mouse models, other types of samples that are amenable to microscopy could also be analyzed using this technique as elaborated in Chapter 4 and 5. We foresee novel applications of this methodology in areas ranging from chemical biology, pathology and microbiology to neuroscience, medicine and agriculture.

2.5 Methods and Experiments

2.5.1 Mass Spectrometric Analysis

Analysis was performed directly on the tissue via AMM using a hybrid ion trap quadrupole Fourier transform ion cyclotron resonance (LTQ-FT-ICR) mass spectrometer (Thermo Electron, North America). The instrument was first tuned to m/z 816.3 using 2 μM bovine cytochrome c (Sigma-Aldrich) 65/35 (v/v) acetonitrile/0.05% formic acid aqueous solution. Ion spectra of 200-2000 *m/z* (E12.5 and E15.5 mice) or isolated ion spectra at 830 m/z with a 100 *m/z* isolation window (for the other time points) were recorded. High-resolution FT-ICR-MS detection was performed using 8000 ms maximum ion accumulation time although in general it took 100-1000ms per scan at 50,000 resolution. The largest protein we observed in this study is ~16 kDa. At a flow rate of μL/min scale, MS signals from molecules on the tissue sections decay within a few min and therefore the shorter scans were preferred. 50,000 resolution was the right balance between our ability to detect isotopes of the proteins vs scan rate and the quality of the signals in the resulting averaged dataset. A 1000 ms maximum ion accumulation time was used for low-resolution LTQ detection. The top-down MS^2 and MS^3 analyses were performed utilizing a collision energy of 30% and an activation Q of 0.200 for both LTQ (isolation $\Delta m/z=3$) and FT-ICR (isolation $\Delta m/z=8$) detections. MS/MS ion intensity of multiple sample points was accumulated to increase the signal-to-noise ratio. For protein analysis the charge states of the ion fragments measured in the ion trap were confirmed by high resolution FT-ICR-MS/MS. The raw FT-ICR-MS/MS spectra were deconvoluted by Xtract (Thermo Electron) as neutral monoisotopic spectra.[54] We also

manually inspected and deconvoluted the raw spectra;[55] ion fragments of isotopic patterns that were not identified by Xtract were manually pulled out. The ions for all the neutral monoistopic masses were analyzed against the candidate proteins in ProSight PTM for validation.[27] Ions of proteins were mainly verified on the basis of the annotations to the mono-isotopic y and b fragments. The amino acid sequences of the candidate proteins were obtained from the online protein data bank (www.pdb.org) and UniProt.[56,57]

2.5.2 Sample Preparation and Immunohistochemistry

Mouse matings were timed to obtain embryonic and neonatal samples. EphA4 -/- males (CB6F1/J background) and EphA4 -/+; Hb9::eGFP females (CB6F1/J background) were used for the E15.5 time point.[58,59] For the other time points, Hb9::eGFP males (CB6F1/J background) and ICR females were used.

Embryos were collected in cold phosphate buffered saline (PBS), drained on a perforated spoon, and flash frozen in isopentane on dry ice briefly. For neonatal samples, the lower body from euthanized animals was collected and flash frozen. For adult samples, lumbar levels of vertebrae with surrounding tissue were removed from euthanized animals and flash frozen quickly. Frozen samples were equilibrated to -15 ^{o}C prior to cryosectioning (Leica CM1850). The rostral part of each sample was affixed to a specimen chuck with a dab of O.C.T. (Optimal Cutting Temperature) Compound (Tissue-Tek 4583), taking care to avoid contamination of relevant tissues and equipment. From the caudal end of the sample, 50-um-thick successive sections were cut and, upon reaching lumbar levels, collected onto glass slides (VWR 48311-703). Each slide was

briefly dried on a heat plate, and the slides were stored in -80^{o}C before mass analysis. Tβ-4 knockout mice are described elsewhere.[60] The slides for ambient mass spectrometry investigation were quickly placed in an air-flowed fume hood to prevent water condensation on the slide until reaching thermal equilibrium at ambient temperatures. To decrease the lipid component of the cell membrane, the slides were quickly rinsed with chloroform. 20 μL of chloroform was pipetted onto the slide on the region of tissue to be measured. We gently shook the slide for 10 seconds and removed the solvent by tilting the slide. The rinse process was performed three times on each slide.

Thymosin β-4 (H-2608) and β-10 (H-2928) standards were purchased from Bachem, Inc. Ubiquitin (89165-288) and glutathione (89143-386) standards were purchased from VWR International. *S*-adenosyl methionine (A7007) and L-alpha glycerylphosphorylcholine (G5291) standards were purchased from Sigma-Aldrich, Inc.

Immunohistochemistry was performed as described previously.[59] Isolated mouse spinal cords (P4) were fixed with 4% paraformaldehyde and cryosectioned. Immunohistochemistry was performed with rabbit anti-Tβ-4 (AB6019, Millipore; 1:1000).

2.5.3 Spatial Profiling and Data Processing

To visualize the molecular distribution on the tissue, we first generated the coordinates of imaging pixels on the tissue sections within 2-to-5-mm^2 regions (dependent on the developmental stages) near the spinal cord. The digital photographs of the tissue sections were taken with the inverted microscope on which the nanoDESI was mounted and sketched with referential grids (100 to 200 μm each) as the coordinate that

needed to be targeted with nanoDESI. Once the liquid junction contacted the tissue surface, MS spectra were recorded. The data for each pixel was accumulated for 1 minutes after the extracted compounds were detected by nanoDESI-MS. The tissue was lowered down to remove it from the liquid junction. The tissue stayed offline for 2 minutes before moving to the next pixel in order to flush out the remaining compounds in the secondary capillary tube and prevent inter-pixel contamination. All of the sampling process and ionization were performed at ambient pressure and temperature.

After the MS collection of all pixels, the raw spectra of each pixel were exported in ASCII format for image processing. For the purpose of speeding up the data processing, we compressed the raw data by binning the intensity within 0.01 m/z and integrated the spectral area in the bin. The integrated data were spatially arranged according to the corresponding coordinate. The ion intensity arrays of the corresponding *m/z* were exported into the two-dimensional contour maps. To improve the visualization we smoothed the output data by applying bilinear interpolation (3rd order) that considers the intensity of the neighboring pixels. The data processing and the generation of contour maps were both carried out in MATLAB.

2.6 Supporting Information

2.6.1 Protein Identification via Top-down MS/MS

Table 2.2 List of proteins characterized using high resolution FT mass spectrometry analysis.

Protein	Theoretical Mass (Da)	Observed Mass (Da)	Mass Error (ppm)
Hemoglobin α-1	14944.72	14944.73	1
Hemoglobin α-2	14958.74	14958.73	-1
Hemoglobin α-3	14971.73	14971.76	-2
Hemoglobin α-4	14985.75	14985.71	-2
Hemoglobin α-5	15000.78	15000.78	0
Hemoglobin β-1	15607.11	15607.04	-5
Hemoglobin β-2	15699.11	15699.00	-5
Hemoglobin ε-Y2*	16004.40	16004.34	-4
Hemoglobin βH1*	16352.67	16352.59	-5
Thymosin β-4	4960.49	4960.48	-2
Thymosin β-10	4933.52	4933.51	-2
Ubiquitin	8559.62	8559.64	3

* See reference 61, 62 for more details.

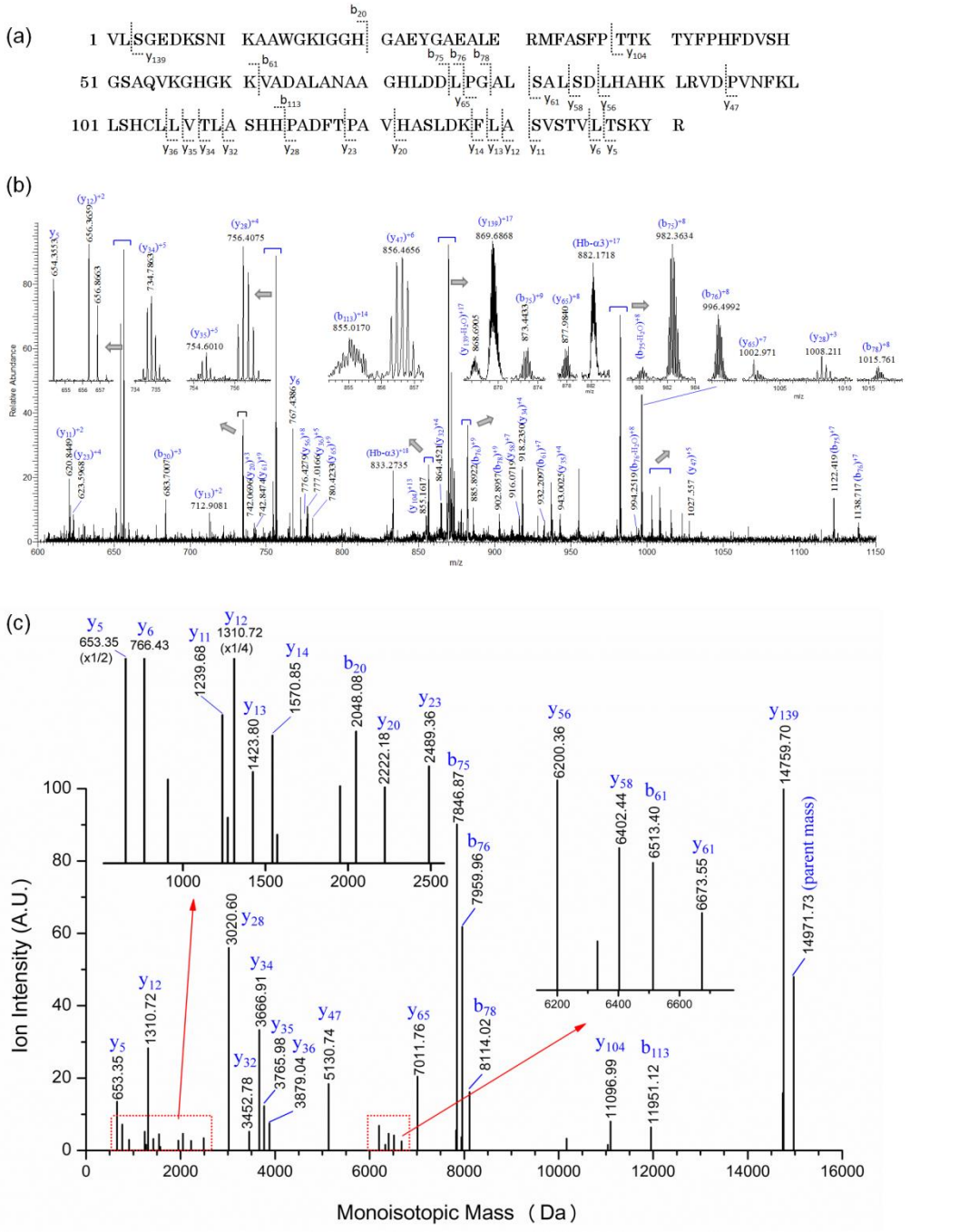

Figure 2.7 Top-down FT-MS/MS analysis of *Mus musculus* hemoglobin subunits α-3 (Hb α–3, 14971.7 Da) acquired on the P2 mouse section using AMM. (a) Amino acid (a.a.) sequences[1] and fragmentation map. (b) FT-MS/MS spectra of isolated Hb α–3 ions (m/z 833.2735, +18 charge). Isolation Δm/z = 5 @ m/z 835, only Hb α–3 was isolated. The numbers indicate the m/z of the corresponding peaks or the highest peaks in the isotopic clusters. The blue labels denote the ion fragment annotations and the charge states. (c) Deconvoluted FT-MS/MS spectra of Hb α–3. The numbers indicate the neutral monoisotopic mass of the corresponding fragments.

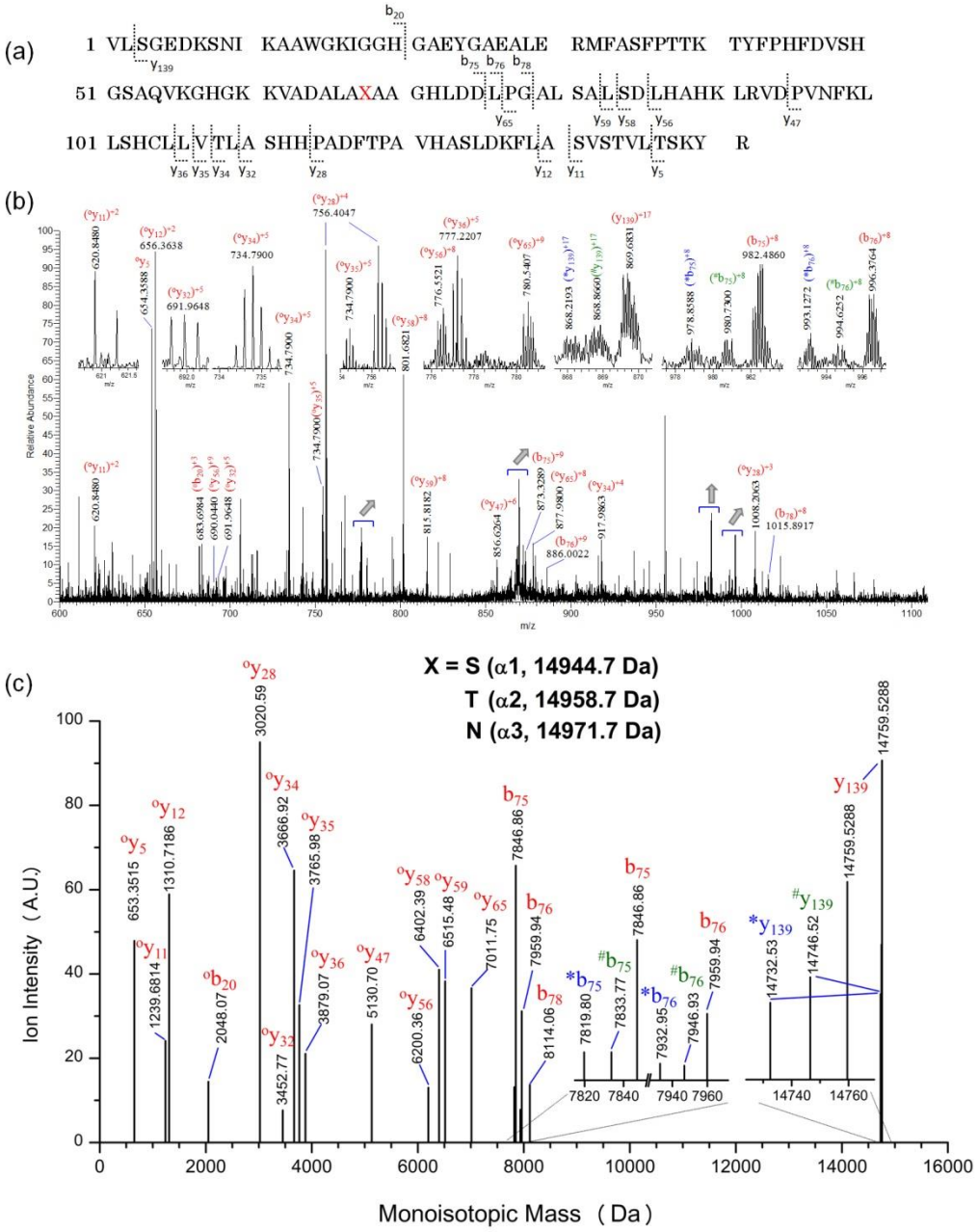

Figure 2.8 Top-down FT-MS/MS analysis of *Mus musculus* hemoglobin subunits α1-3 (Hb α1-3, 14944.7-14971.7 Da) acquired on the E15.5 mouse section using AMM. (a) a.a. sequences[1] and fragmentation map based on the tandem mass analysis. The red tag denotes the sequence variations from Hb α–1 and α–2 (both BABL/c strains) to α–3 (C57BL strain).[1] (b) FT-MS/MS spectra of isolated Hb α1-3 ions (m/z 830-833, +18 charge, isolation Δm/z = 8 @ *m/z* 832). The numbers indicate the *m/z* of the corresponding peaks or the highest peaks in the isotopic clusters. The blue labels denote the ion fragment annotations and the charge states. Peptide fragments superscripts: °(common fragments for all three Hb-α), *(α–1), #(α–2), and no superscript (α3). (c) Deconvoluted FT-MS/MS spectra of Hb-α mixtures. The numbers indicate the neutral monoisotopic mass of the corresponding ion fragments.

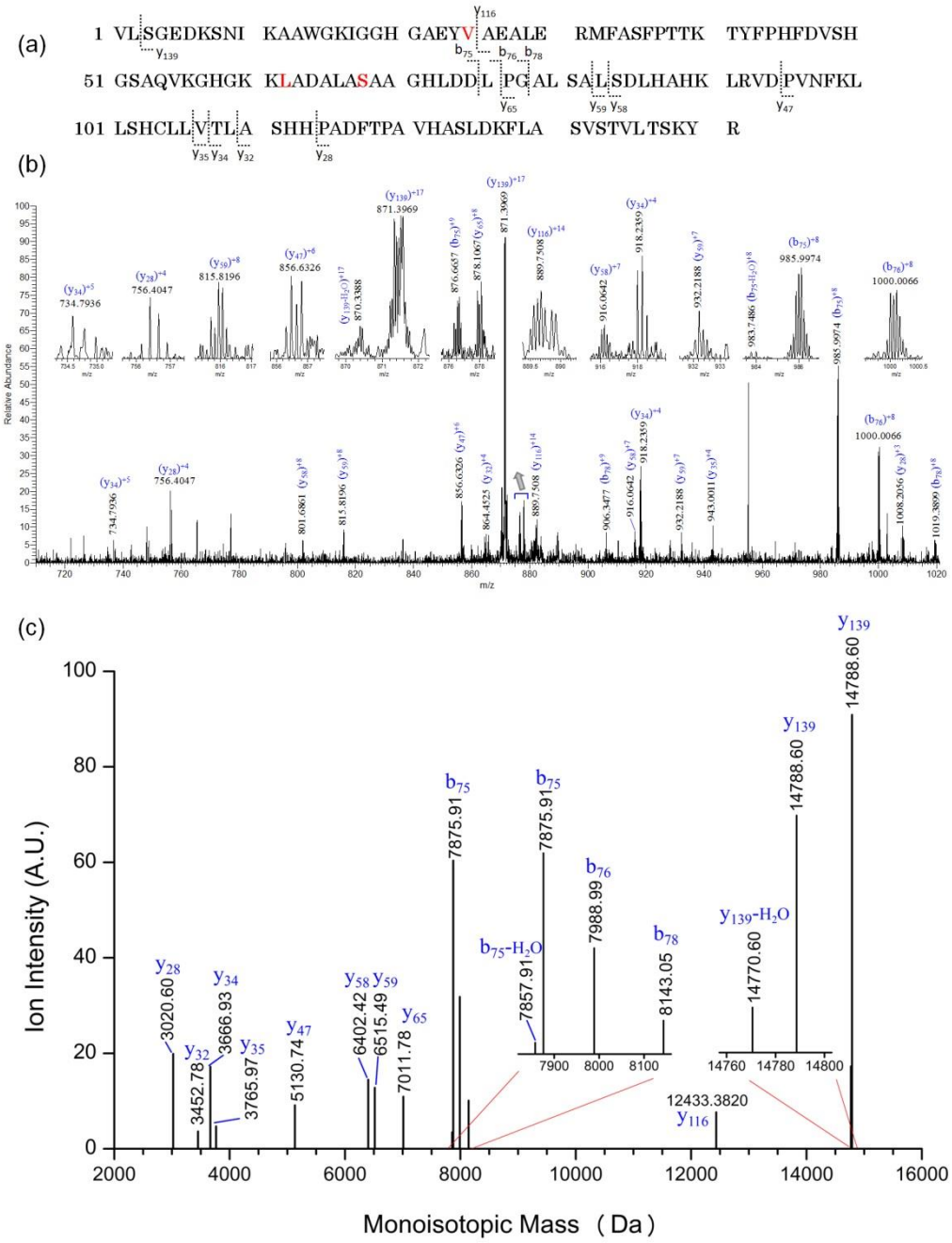

Figure 2.9 Top-down FT-MS/MS analysis of *Mus musculus* hemoglobin subunits α–5 (Hb α–5, 15000.7 Da) acquired on the E13.5 mouse section using AMM. (a) a.a. sequences[1] and fragmentation map. The red tag denotes the possible variants of the sequence to that of Hb α–3 (C57BL strain).[1] (b) FT-MS/MS spectra of isolated Hb α–5 ions (m/z 834.8299, +18 charge). Isolation Δ*m/z* = 5 *@ m/z* 836, only Hb α–5 was isolated. The numbers indicate *the m/z* of the corresponding peaks or the highest peaks in the isotopic clusters. The blue labels denote the ion fragment annotations and the charge states. (c) Deconvoluted FT-MS/MS spectra of Hb α–5. The numbers indicate the neutral monoisotopic mass of the corresponding ion fragments.

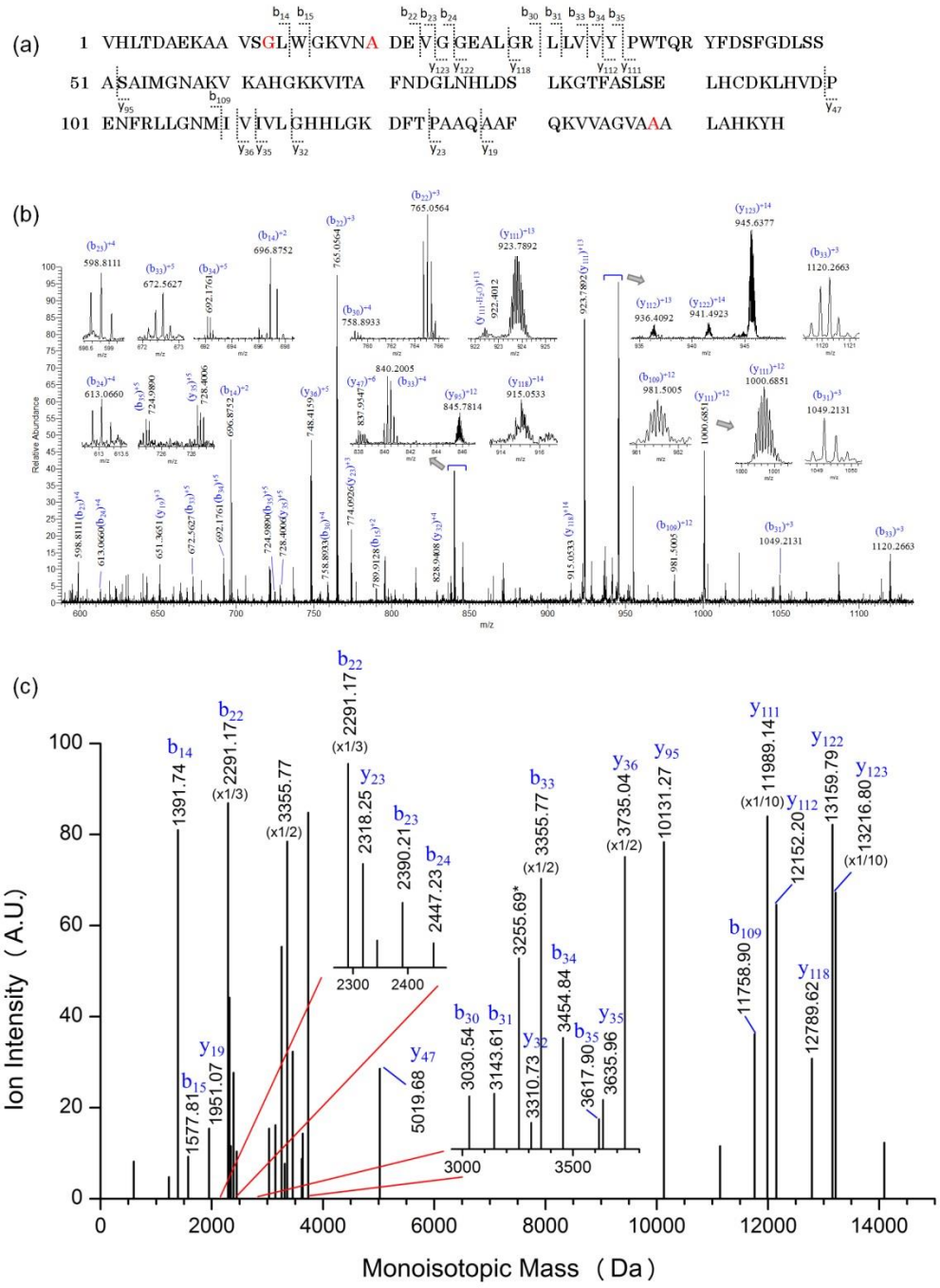

Figure 2.10 Top-down FT-MS/MS analysis of *Mus musculus* hemoglobin subunits β-1 (Hb β–1, 15607.1 Da) acquired on the P2 mouse section using AMM. (a) a.a. sequences[3] and fragmentation map. The red tag denotes the sequence variations between Hb β–1 and β–2. (b) FT-MS/MS spectra of isolated Hb β–1 ions (*m/z* 868.5106, +18 charge). The numbers indicate the m/z of the corresponding peaks or the highest peaks in the isotopic clusters. The blue labels denote the ion fragment annotations and the charge states. (c) Deconvoluted FT-MS/MS spectra of Hb β-1. The numbers indicate the neutral monoisotopic mass of the corresponding fragments.

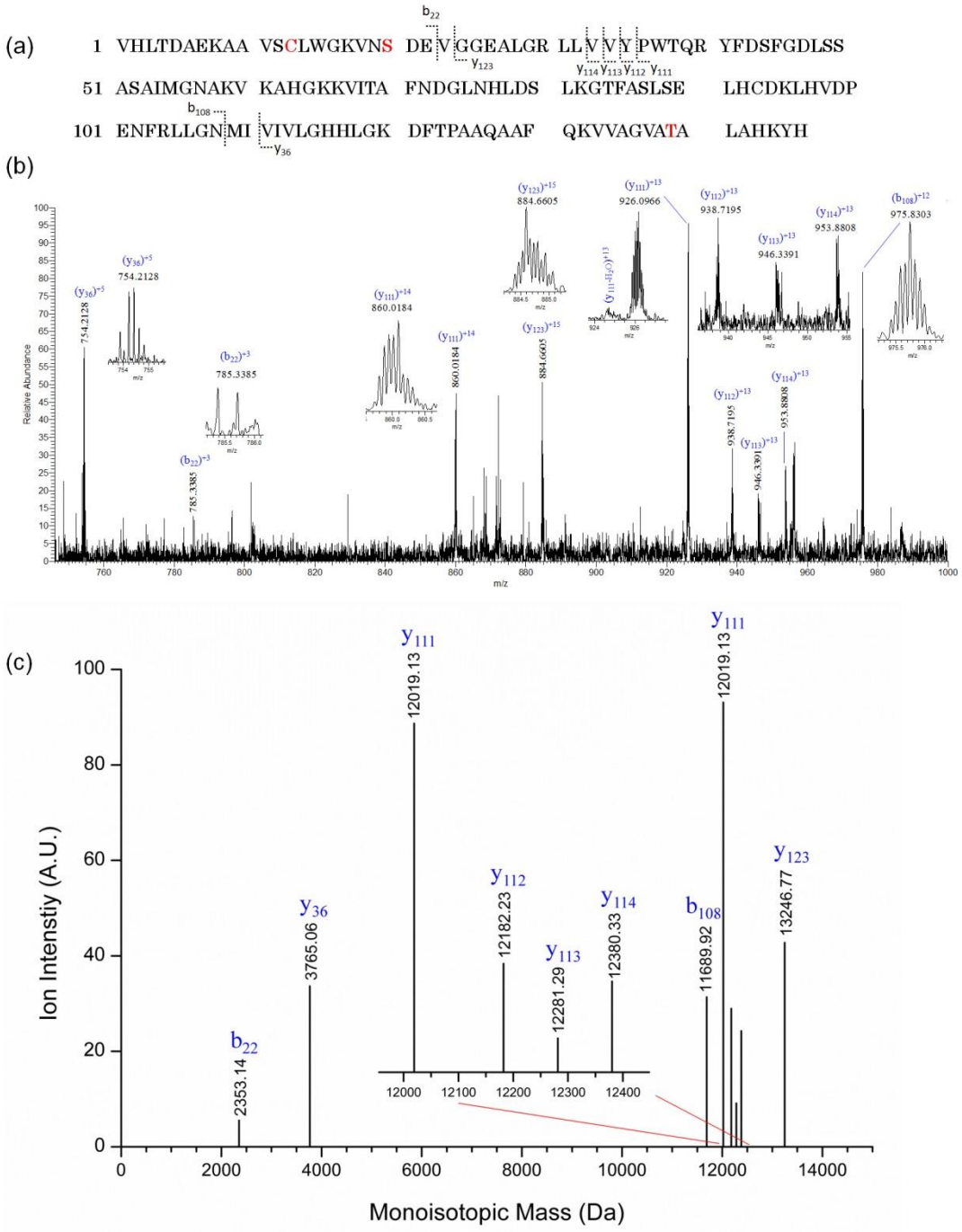

Figure 2.11 Top-down FT-MS/MS analysis of *Mus musculus* hemoglobin subunits β-2 (Hb β–2, 15699.1 Da) acquired on the P10 mouse section using AMM. (a) a.a. sequences[3] and fragmentation map. The red tag denotes the sequence variations between Hb β–1 and β–2. (b) FT-MS/MS spectra of isolated Hb β–2 ions (*m/z* 827.7473, +19 charge). The numbers indicate the *m/z* of the corresponding peaks or the highest peaks in the isotopic clusters. The blue labels denote the ion fragment annotations and the charge states. (c) Deconvoluted FT-MS/MS spectra of Hb β-2. The numbers indicate the neutral monoisotopic mass of the corresponding fragments.

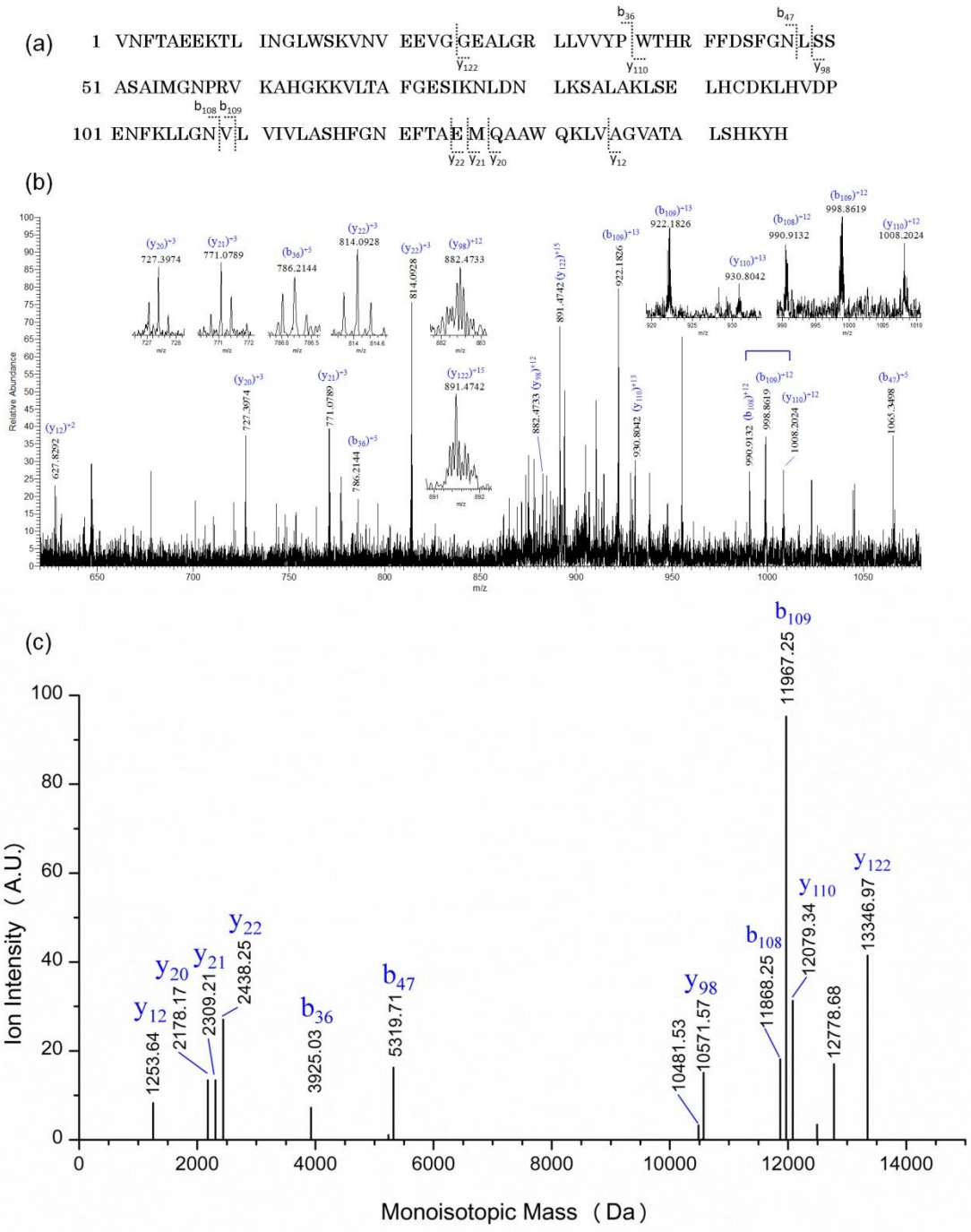

Figure 2.12 Top-down FT-MS/MS analysis of *Mus musculus* hemoglobin subunits ε-Y2 (Hb-εY2, 16004.4 Da) acquired on the E13.5 mouse section using AMM. (a) a.a. sequences[4] and fragmentation map. (b) FT-MS/MS spectra of isolated Hb-εY ions (*m/z* 843.8268, +19 charge). The numbers indicate the m/z of the corresponding peaks or the highest peaks in the isotopic clusters. The blue labels denote the ion fragment annotations and the charge states. (c) Deconvoluted FT-MS/MS spectra of Hb-εY. The numbers indicate the neutral monoisotopic mass of the corresponding fragments.

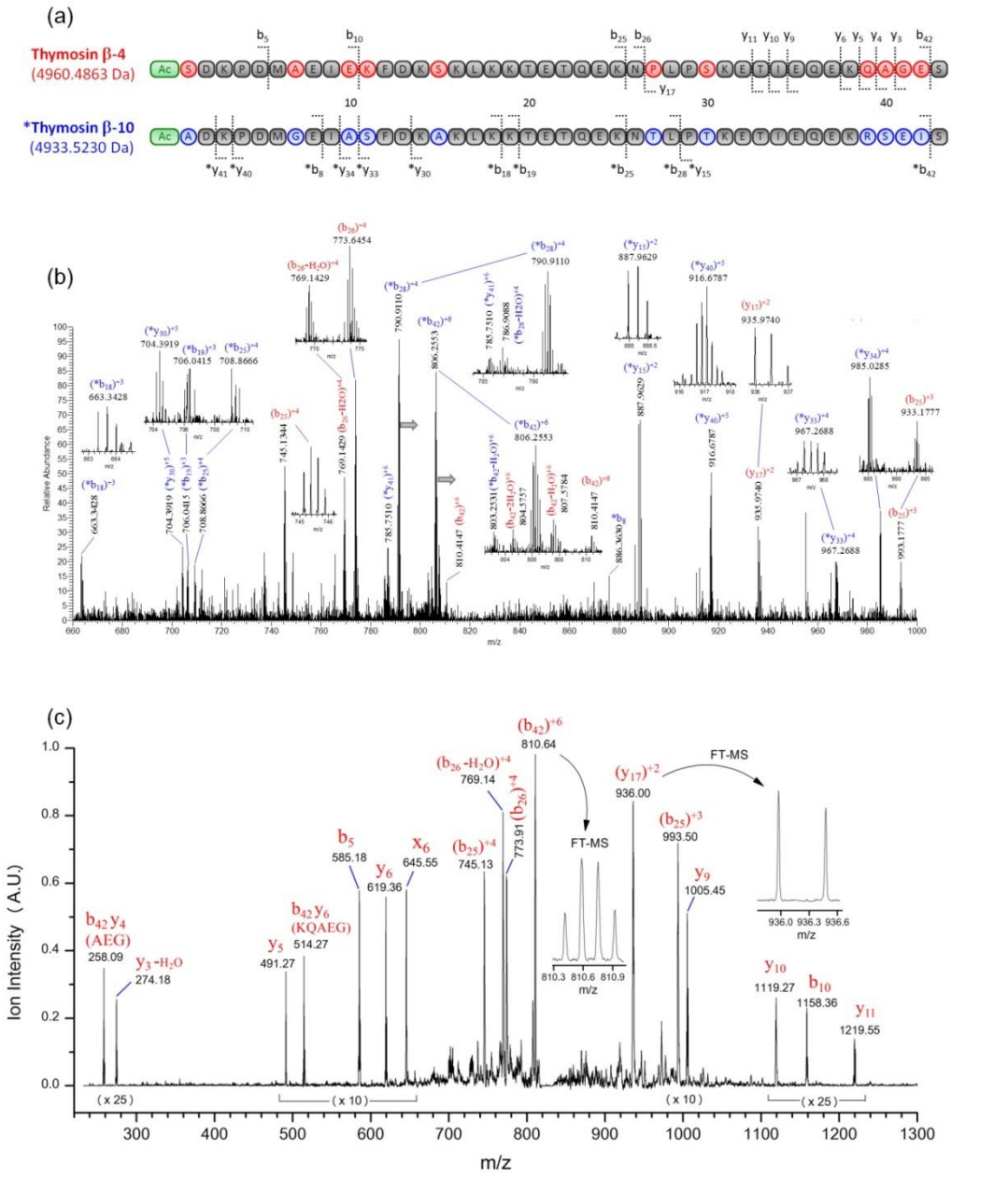

Figure 2.13 Top-down MS/MS analysis of thymosin β-10 (*) and β-4 (red, no superscript) by AMM acquired on the E15.5 mouse spinal cord. (a) a.a. sequences and the fragmentation map. The grey tags represent the conserved a.a. residues of the two β-thymosins. The green tags represent the acetylation on the N-terminals. (b) FT-MS/MS spectra of Tβ-4 and Tβ-10 ion mixtures. Isolation mass = 823.6 *m/z*. The numbers indicate the *m/z* of the corresponding peaks or the highest peaks in the isotopic clusters. The labels (red: Tβ-4; blue: Tβ-10) denote the ion fragment annotations and the charge states. (c) Low resolution LTQ-MS/MS spectrum of Tβ–4. Isolation mass = 828.1 *m/z*. *Insets*: high resolution spectra of the multiple-charge states of the ion fragments. (d) Deconvoluted FT-MS/MS spectra of Tβ-4 and Tβ-10 ion mixture. The numbers indicate the neutral monoisotopic mass of the corresponding peaks.

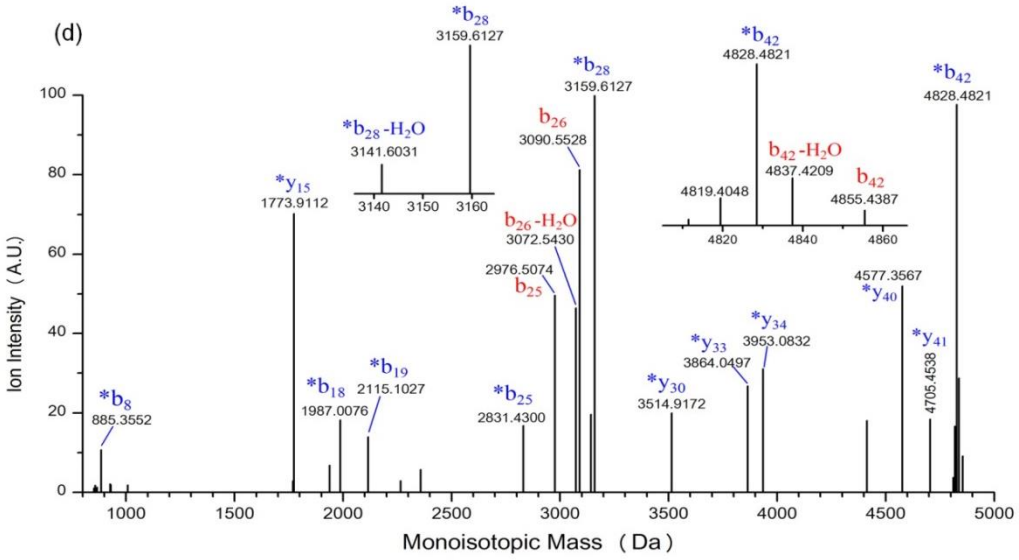

Figure 2.13 Top-down MS/MS analysis of thymosin β-10 (*) and β-4 (red, no superscript) by AMM acquired on the E15.5 mouse spinal cord. (a) a.a. sequences and the fragmentation map. The grey tags represent the conserved a.a. residues of the two β-thymosins. The green tags represent the acetylation on the N-terminals. (b) FT-MS/MS spectra of Tβ-4 and Tβ-10 ion mixtures. Isolation mass = 823.6 *m/z*. The numbers indicate the *m/z* of the corresponding peaks or the highest peaks in the isotopic clusters. The labels (red: Tβ-4; blue: Tβ-10) denote the ion fragment annotations and the charge states. (c) Low resolution LTQ-MS/MS spectrum of Tβ–4. Isolation mass = 828.1 *m/z*. *Insets*: high resolution spectra of the multiple-charge states of the ion fragments. (d) Deconvoluted FT-MS/MS spectra of Tβ-4 and Tβ-10 ion mixture. The numbers indicate the neutral monoisotopic mass of the corresponding peaks. (*Continued*)

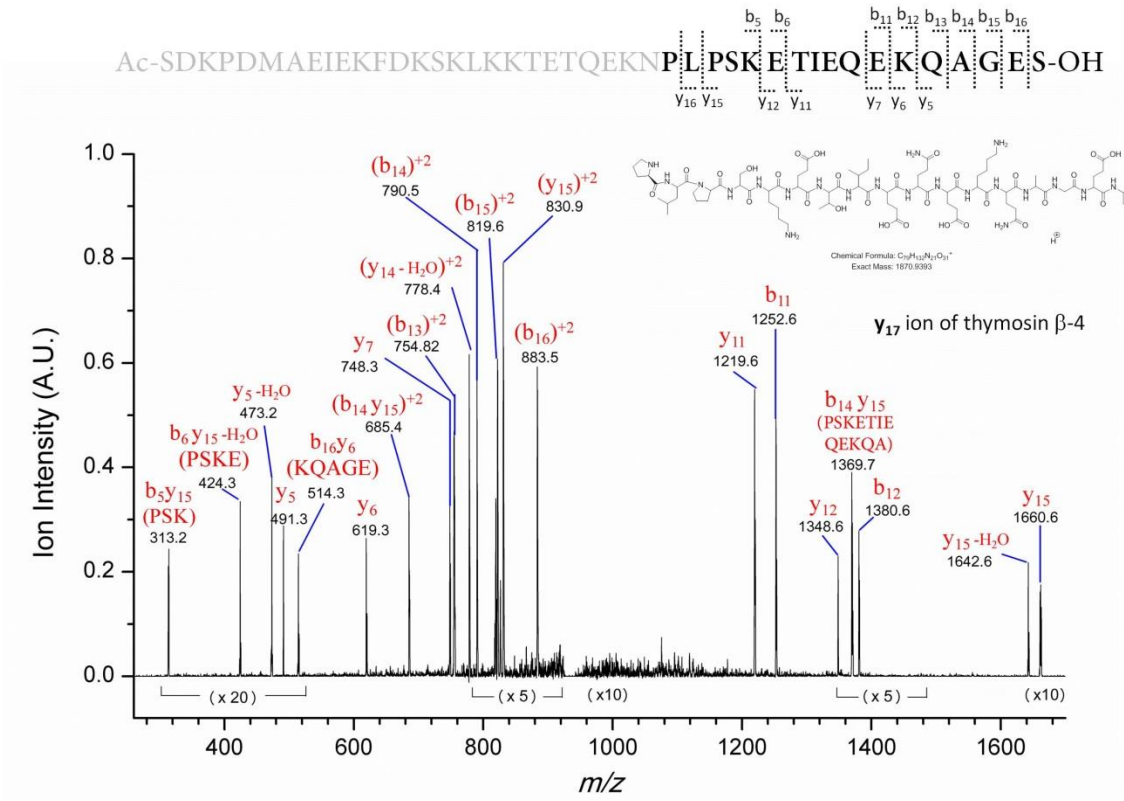

Figure 2.14 Top-down MS^3 spectrum of thymosin β-4 y_{17} ion (*m/z* 936 in the MS/MS of Tβ-4, Figure 2.13) by AMM acquired on the E15.5 mouse spinal cord. *Top*: a.a. sequences and the fragmentation map. *Bottom*: Low resolution LTQ-MS^3 spectrum of thymosin β-4 y_{17} ion. Isolation mass = 936 *m/z*. The red labels denote the ion fragment annotations and the charge states.

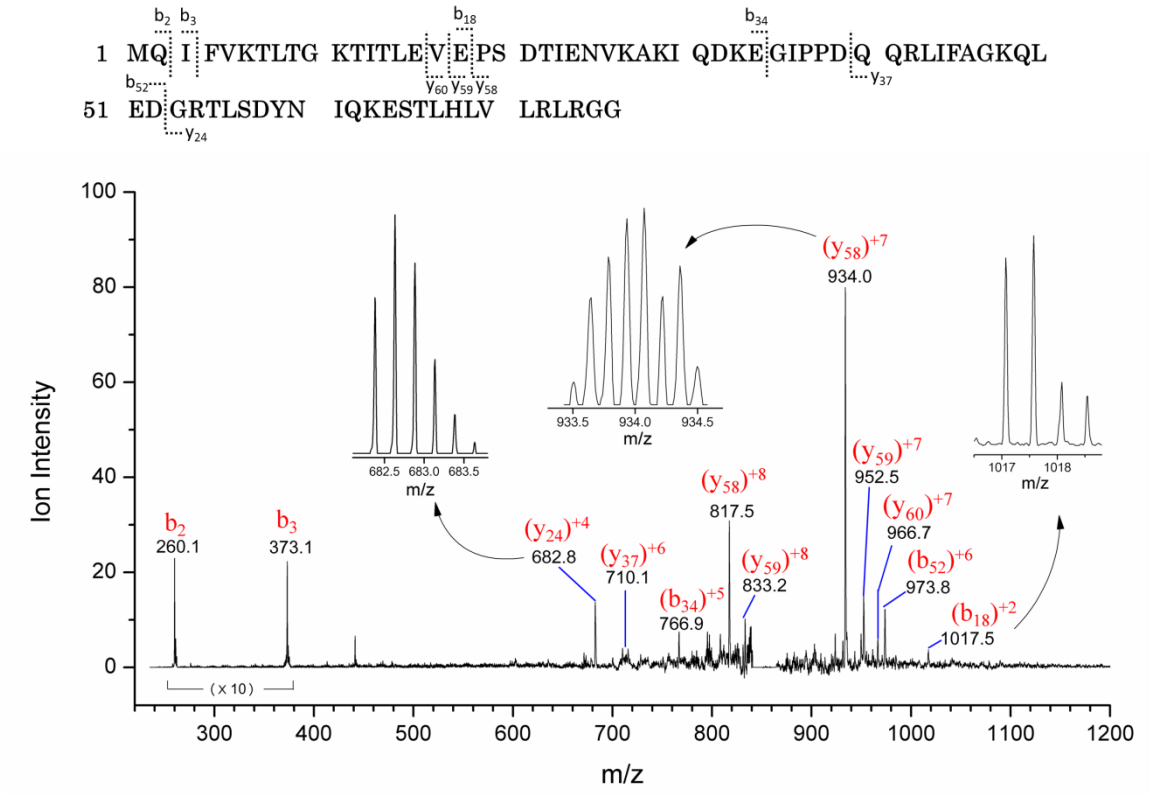

Figure 2.15 Top-down MS/MS analysis of ubiquitin by AMM acquired on the P2 mouse spinal cord. *Top*: a.a. sequences and the fragmentation map. *Bottom*: Low resolution LTQ-MS/MS spectrum of ubiquitin. The red labels denote the ion fragment annotations and the charge states. *Insets*: high resolution FT-MS spectra of the multiple-charge states of the ion fragments.

2.6.2 Tandem Mass Analysis of Lipids and Small Metabolites

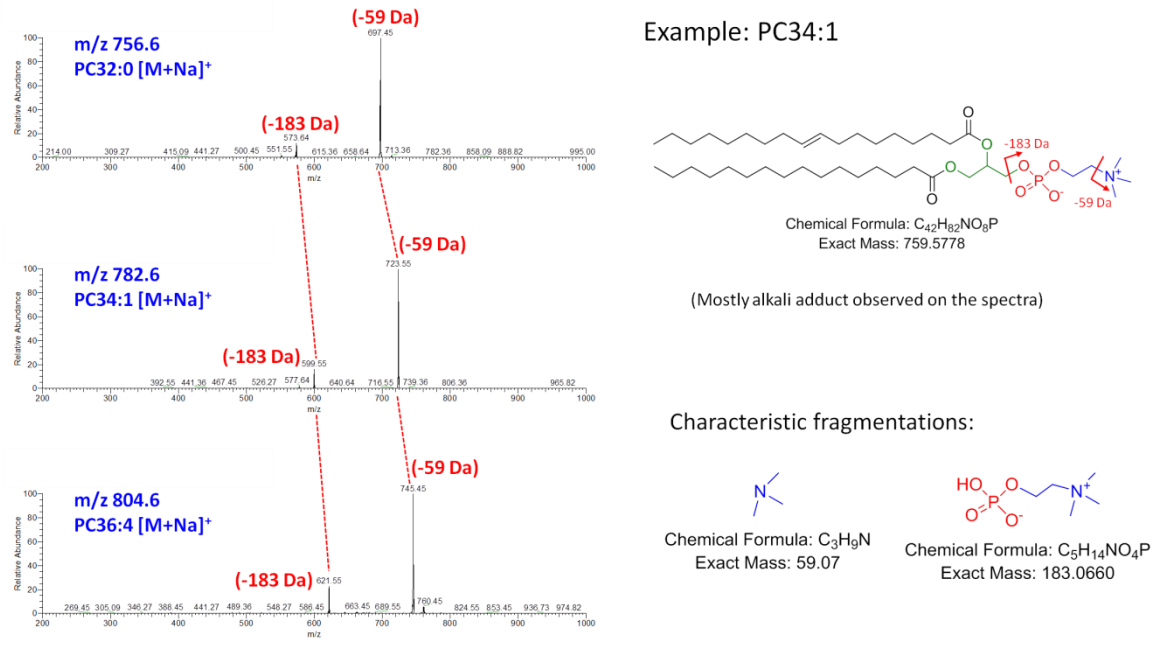

Figure 2.16 Top-down MS/MS analysis of representative phospholipids found on the E15.5 mouse sections.

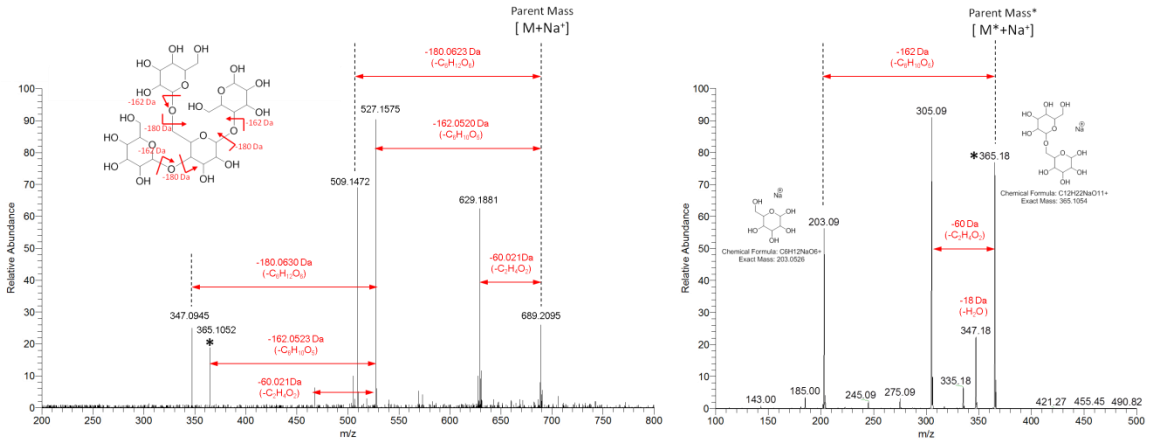

Figure 2.17 Tandem mass analysis of tetra-hexose (left, m/z 689.2096, error to the theoretical *m/z* = 2 ppm) found on the E15.5 mouse cartilage primordium by AMM. *Left*: FT-MS/MS spectra of tetra-hexose. Isolation mass = 689.2 *m/z*. The asterisk at *m/z* 365 indicates the disaccharide ion, which is confirmed by the FT-MS^3 spectrum on the *right*.

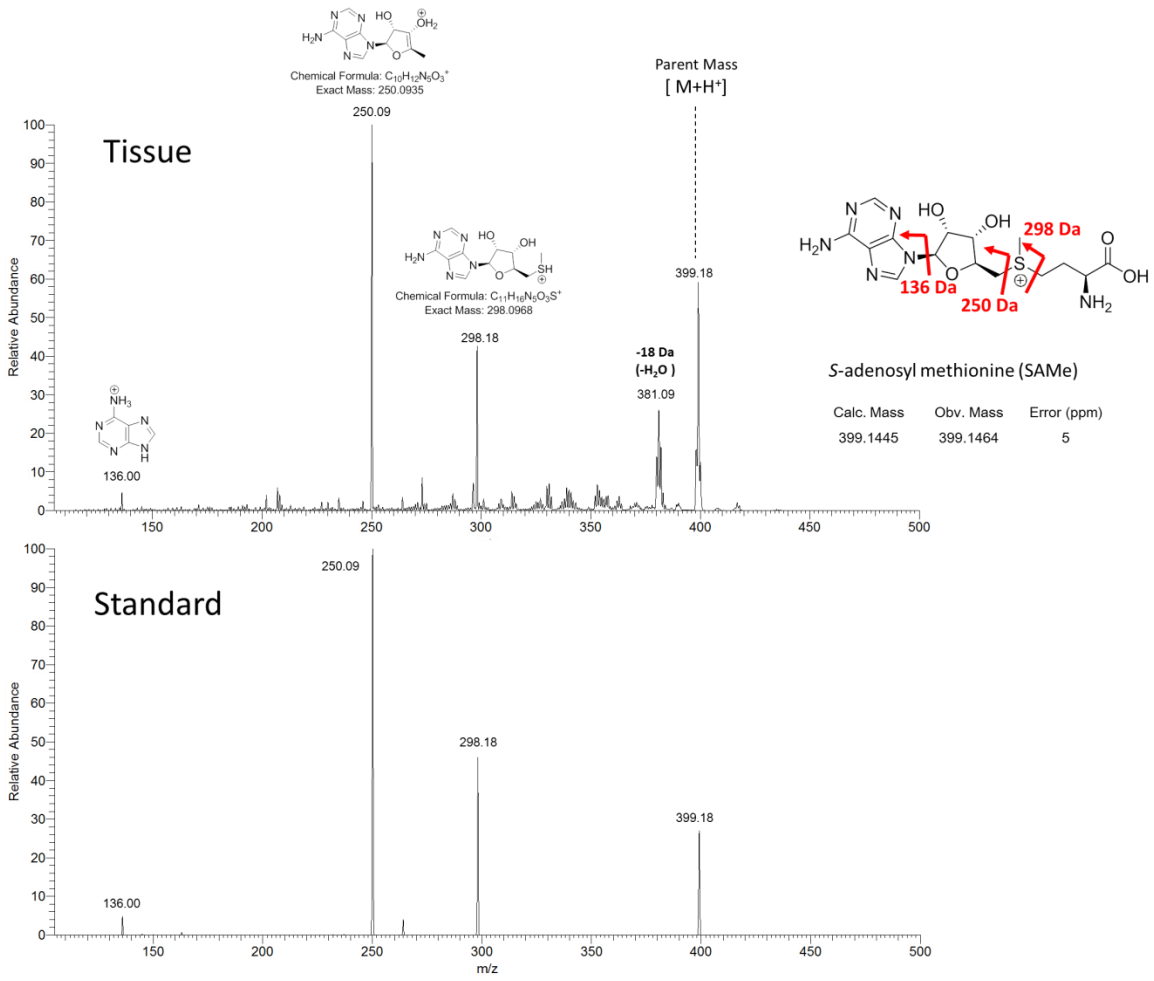

Figure 2.18 Tandem mass analysis of *S*-adenosyl methionine (SAM) acquired by AMM. *Top*: LTQ-MS/MS of SAM found on the E15.5 mouse spinal cords. *Bottom*: LTQ-MS/MS of SAM standard directly introduced by AMM.

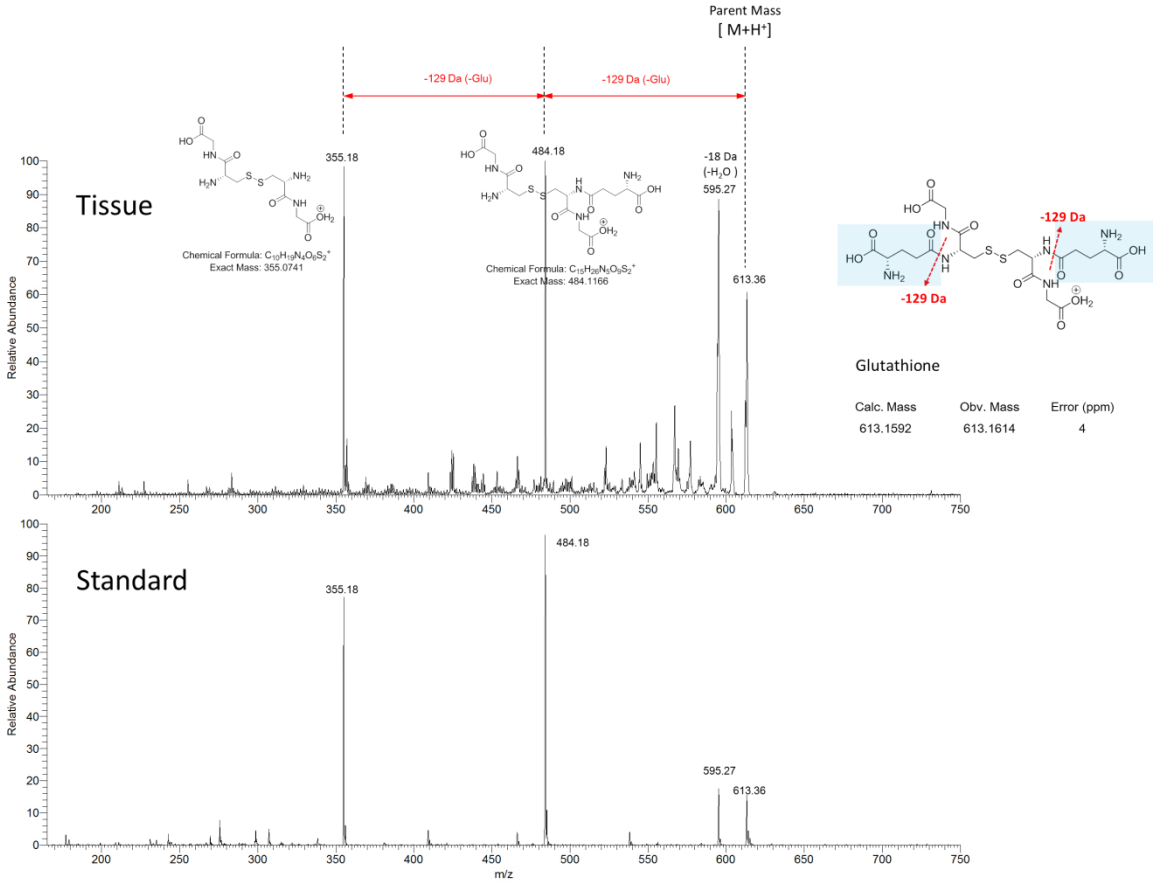

Figure 2.19 Tandem mass analysis of glutathione acquired by AMM. *Top*: LTQ-MS/MS of glutathione found on the E15.5 mouse spinal cords. *Bottom*: LTQ-MS/MS of glutathione standard directly introduced by AMM.

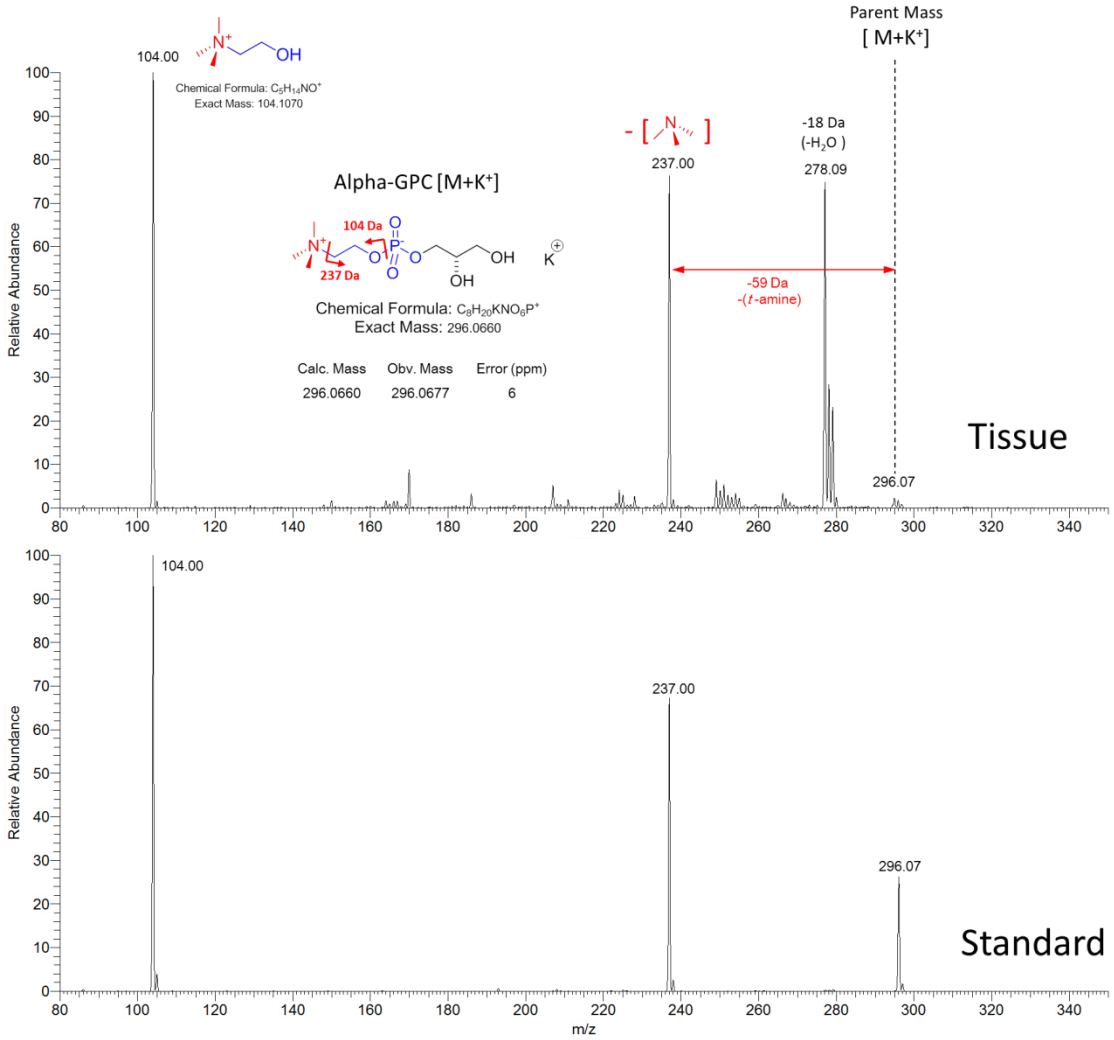

Figure 2.20 Tandem mass analysis of *L*-alpha glycerylphosphorylcholine (Alpha-GPC) acquired by AMM. *Top*: LTQ-MS/MS of Alpha-GPC found on the E15.5 mouse spinal cords. *Bottom*: LTQ-MS/MS of Alpha-GPC standard directly introduced by AMM.

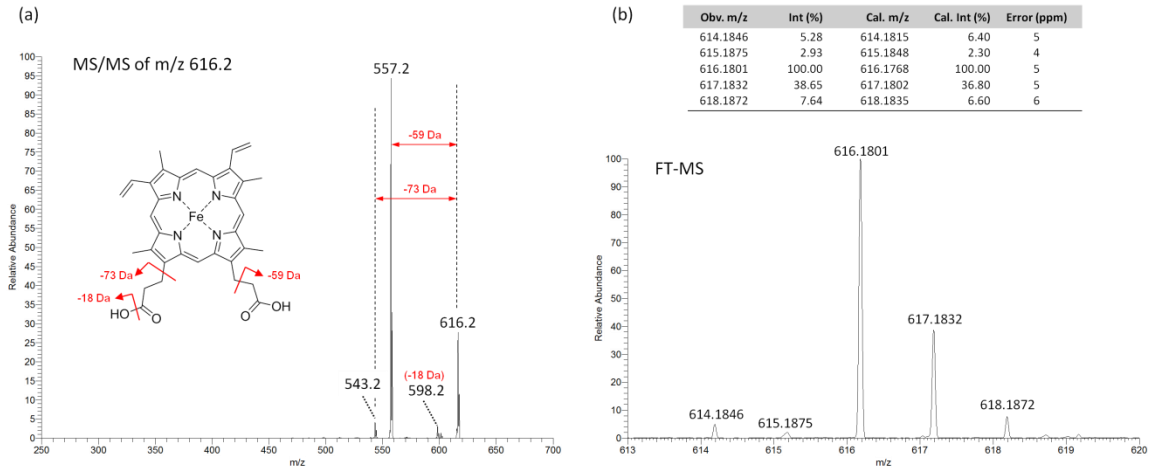

Figure 2.21 MS/MS spectra (a) and high resolution FT-MS spectra (b) of *m/z* 616.180 found on the E15.5 mouse section using AMM. The fragment patterns and isotopic features of the parent ion indicate that m/z 616.180 is the ferric heme B ion. Similar fragment patterns were found by S. Shimma using MALDI-TOF/TOF.[63]

2.6.3 Immunohistochemistry

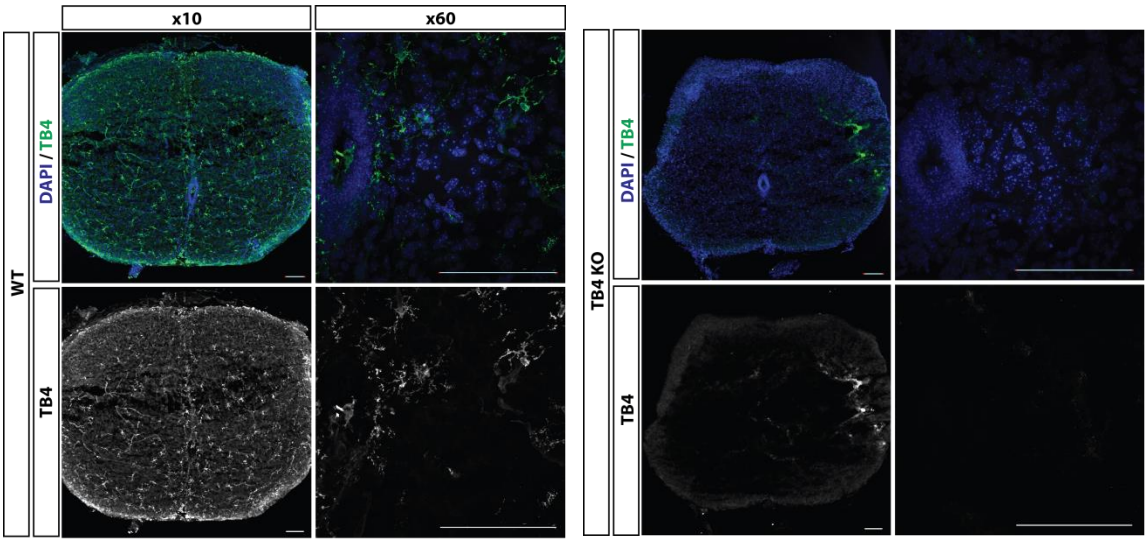

Figure 2.22 Immunohistostaining of P4 wild-type and Tβ-4 knockout mice. Spinal cords were dissected out from Tβ-4 knockout mice and littermate wild-type mice at P4. 50 um of transverse sections were prepared for immunohistochemitry analysis. Scale bar: 100um.

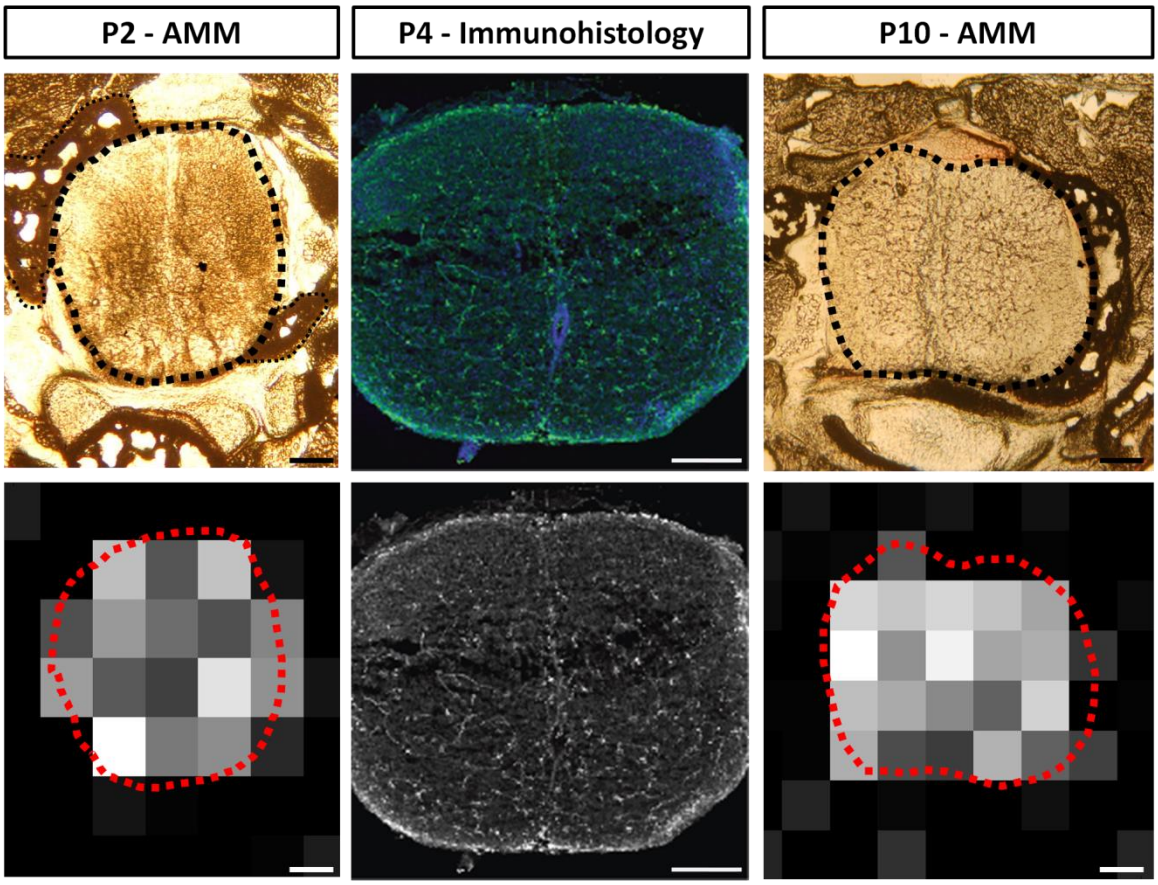

Figure 2.23 Comparison of ambient MS-based molecular images to immunohistostaining of the neonatal mice.

2.6.4 Instrument Responses of β-thymosins

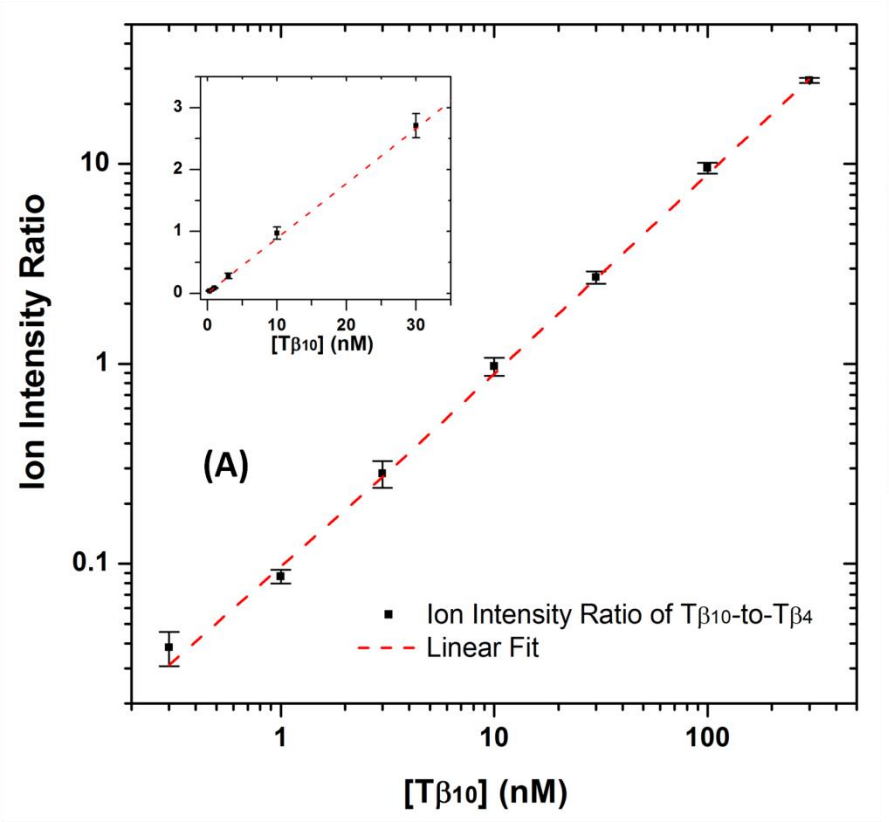

Figure 2.24 Instrumental response of Tβ-10/Tβ-4 intensity ratios at varying Tβ-10 concentration on a logarithmic scale. 10 nM Tβ-4 was used as the internal standard. The ionization efficiencies of Tβ-10 and Tβ-4 are very close (ratio ~ 1.0) and the MS intensity responses a linear read-out against Tβ-10 concentration within 3 orders of magnitude (0.3-300 nM). The detection limit is 0.3 nM (or 0.3 femtomole equivalent at 1 μL/min flow-rate in 1-minute acquisition). *Inset:* linear plot of instrumental response at low concentration range.

2.6.5 Developmental Patterns: the replicates

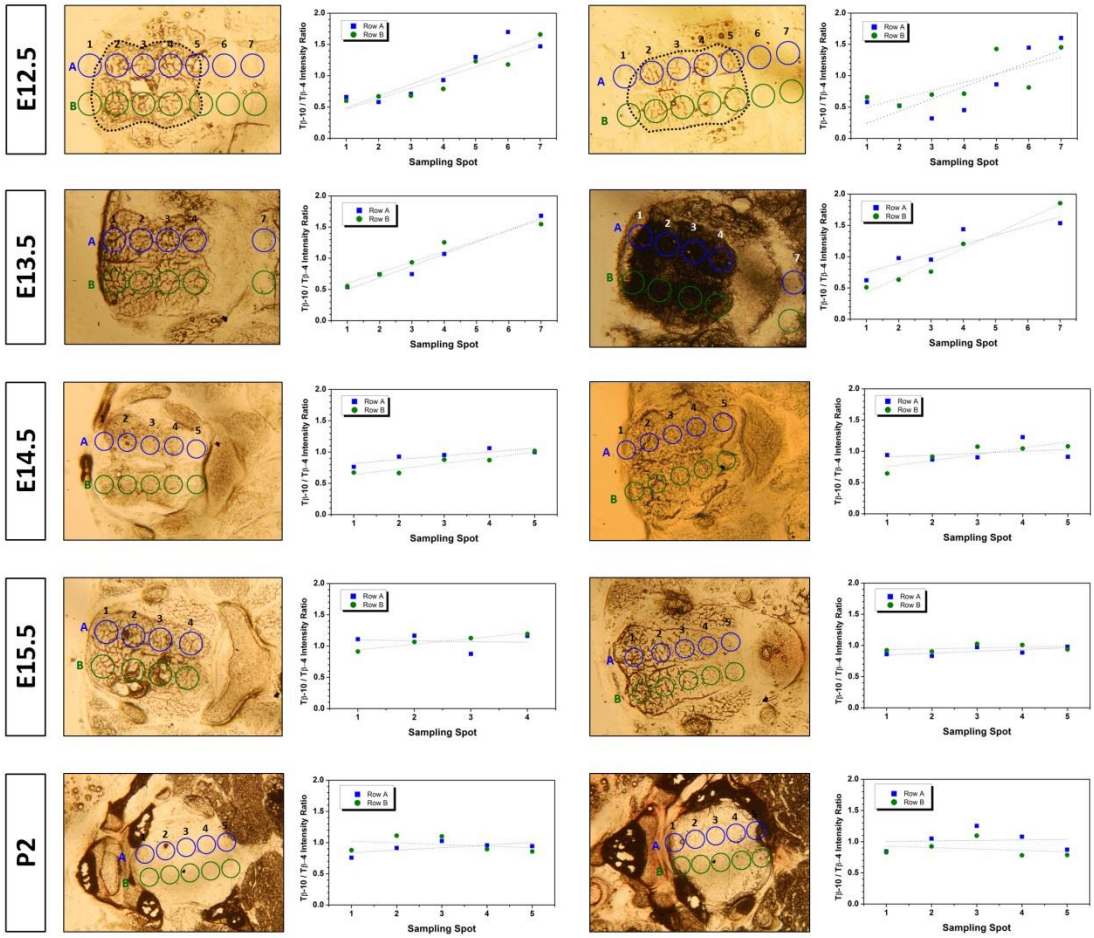

Figure 2.25 Tβ-10/Tβ-4 intensity ratios along the dorsoventral axes of the developing mouse spinal cord (in addition to the data shown in Figure 2.6 of the main manuscript)**.** The blue and green circles indicate the sample spots at which the ion intensity ratios of Tβ-10/Tβ-4 were plotted to the right.

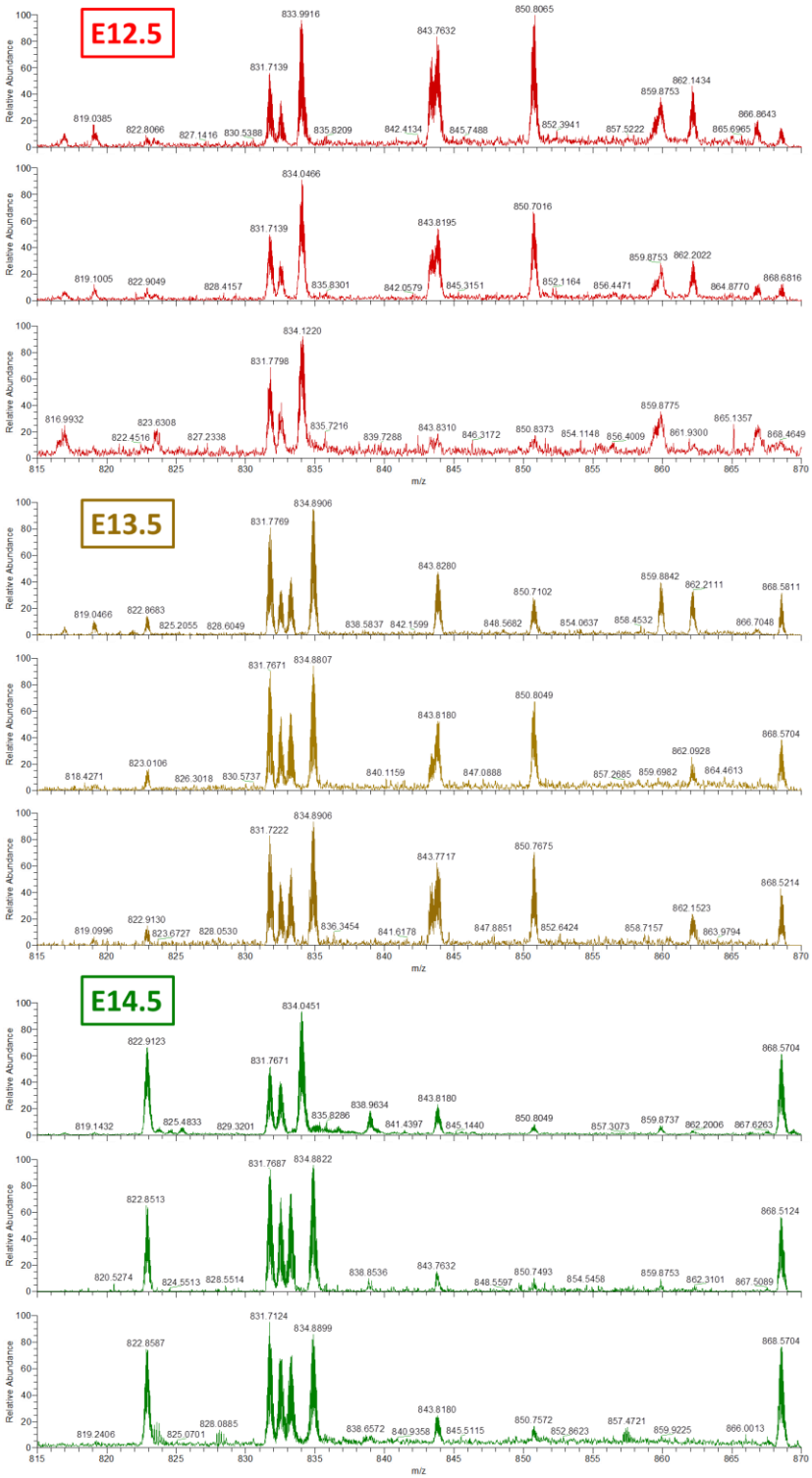

Figure 2.26 Representative FT-MS spectra of embryonic mice hemoglobin obtained on the blood vessel-rich regions of the tissue sections using AMM. The heterogeneity of α-hemoglobin (e.g., the third P2 section express only α–3 [*m/z* 833.2665]) reveals the genetic diversity of different parental background strains.

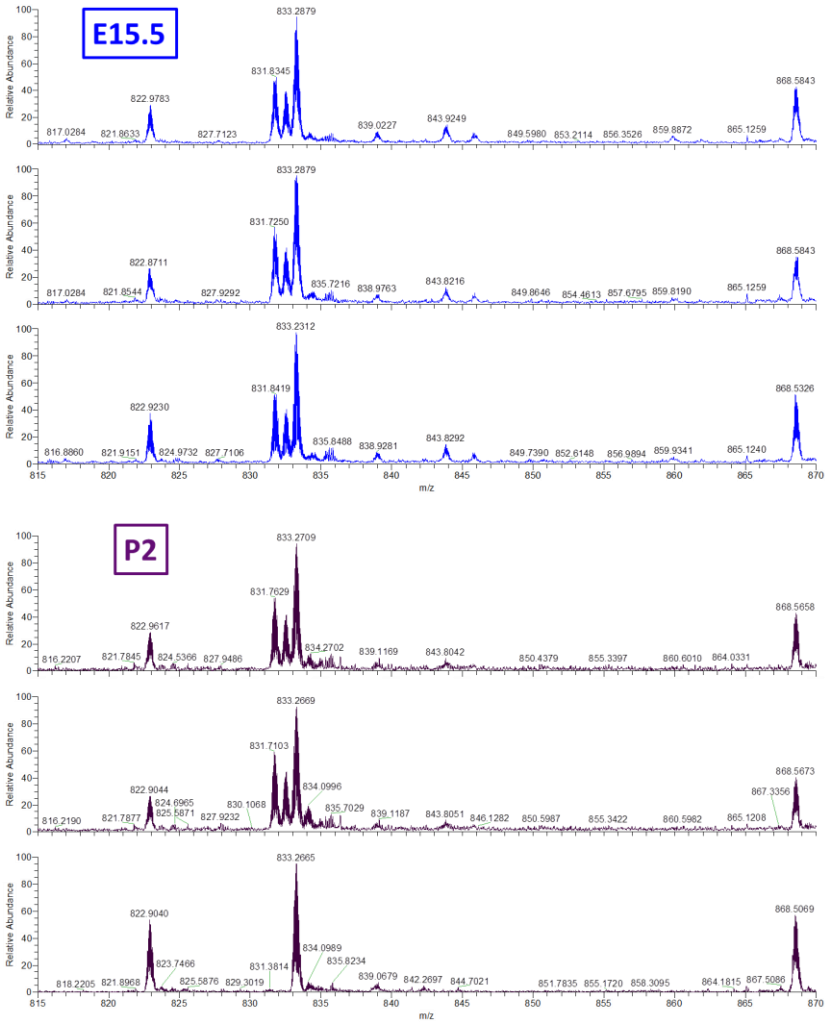

Figure 2.26 Representative FT-MS spectra of embryonic mice hemoglobin obtained on the blood vessel-rich regions of the tissue sections using AMM. The heterogeneity of α-hemoglobin (e.g., the third P2 section express only α–3 [*m/z* 833.2665]) reveals the genetic diversity of different parental background strains. (*Continued*)

2.7 References

(1) Ramos-Vara, J. A. Technical aspects of immunohistochemistry. *Vet. Patho.* **2005**, *42*, 405-426.

(2) Caprioli, R. M.; Farmer, T. B.; Gile, J. Molecular imaging of biological samples: Localization of peptides and proteins using MALDI-TOF MS. *Anal. Chem.* **1997**, *69*, 4751-4760.

(3) Cornett, D. S.; Reyzer, M. L.; Chaurand, P.; Caprioli, R. M. MALDI imaging mass spectrometry: molecular snapshots of biochemical systems. *Nature Methods* **2007**, *4*, 828-833.

(4) Seeley, E. H.; Caprioli, R. M. Molecular imaging of proteins in tissues by mass spectrometry. *Proc. Natl. Acad. Sci. U. S. A.* **2008**, *105*, 18126-18131.

(5) Harada, T.; Yuba-Kubo, A.; Sugiura, Y.; Zaima, N.; Hayasaka, T.; Goto-Inoue, N.; Wakui, M.; Suematsu, M.; Takeshita, K.; Ogawa, K.; Yoshida, Y.; Setou, M. Visualization of volatile substances in different organelles with an atmospheric-pressure mass microscope. *Anal. Chem.* 2009, *81*, 9153-9157.

(6) Lorenz, M.; Ovchinnikova, O. S.; Kertesz, V.; Van Berkel, G. J. Laser microdissection and atmospheric pressure chemical ionization mass spectrometry coupled for multimodal imaging. *Rapid Commun. Mass Spectrom.* **2013**, *27*, 1429-1436.

(7) Ovchinnikova, O. S.; Nikiforov, M. P.; Bradshaw, J. A.; Jesse, S.; Van Berkel, G. J. Combined atomic force microscope-based topographical imaging and nanometer-scale resolved proximal probe thermal desorption/electrospray ionization mass spectrometry. *ACS Nano* **2011**, *5*, 5526-5531.

(8) Aebersold, R.; Mann, M. Mass spectrometry-based proteomics. *Nature* **2003**, *422*, 198-207.

(9) Olsen, J. V.; Blagoev. B.; Gnad, F.; Macek, B.; Kumar, C.; Mortensen, P.; Mann, M.; Global, in vivo, and site-specific phosphorylation dynamics in signaling networks. *Cell* **2006**, *127*, 635-648.

(10) Zanivan, S.; Gnad, F.; Wickström, S. A.; Geiger, T.; Macek, B.; Cox, J.; Fässler, R.; Mann, M. Solid tumor proteome and phosphoproteome analysis by high resolution mass spectrometry. *J. Proteome Res.* **2008**, *7*, 5314-5326.

(11) Domon, B.; Aebersold, R. Review: mass spectrometry and protein analysis. *Science* **2006**, *312*, 212-217.

(12) Grassmann, J.; Scheerle, R. K.; Letzel, T. Functional proteomics: application of mass spectrometry to the study of enzymology in complex mixtures. *Anal. Bioanal. Chem.* **2012**, *402*, 625-645.

(13) Takats, Z.; Wiseman, J. M.; Gologan, B.; Cooks, R. G. Mass spectrometry sampling under ambient conditions with desorption electrospray ionization. *Science* **2004**, *306*, 471-473.

(14) Badu-Tawiah, A. K.; Eberlin, L. S.; Ouyang, Z.; Cooks, R. G. Chemical aspects of the extractive methods of ambient ionization mass spectrometry. *Annu. Rev. Phys. Chem.* **2013**, *64*, 481-505.

(15) Laskin, J.; Heath, B. S.; Roach, P. J.; Cazares, L.; Semmes, O. J. Tissue imaging using nanospray desorption electrospray ionization mass spectrometry. *Anal. Chem.* **2012** *84*, 141-148.

(16) Eckert, P. A.; Roach, P. J.; Laskin, A.; Laskin, J. Chemical characterization of crude petroleum using nanospray desorption electrospray ionization coupled with high-resolution mass spectrometry. *Anal. Chem.* **2012**, *84*, 1517-1525.

(17) Burnum, K. E.; Tranguch, S.; Mi, D.; Daikoku, T.; Dey, S. K.; Caprioli, R. M. Imaging mass spectrometry reveals unique protein profiles during embryo implantation. *Endocrinology* **2008**, *149*, 3274-3278.

(18) Burnum, K. E.; Cornett, D. S.; Puolitaival, S. M.; Milne, S. B.; Myers, D. S.; Tranguch, S.; Brown, H. A.; Dey, S. K.; Caprioli, R. M. Spatial and temporal alterations of phospholipids determined by mass spectrometry during mouse embryo implantation. *J. Lipid Res.* **2009**, *50*, 2290-2298.

(19) Ferreira, C. R.; Pirro, V.; Eberlin, L. S.; Hallett, J. E.; Cooks, R. G. Developmental phases of individual mouse preimplantation embryos characterized by lipid signatures using desorption electrospray ionization mass spectrometry. *Anal. Bioanal. Chem.* **2012**, *404*, 2915-2926.

(20) Ferreira, C. R.; Eberlin, L. S.; Hallett, J. E.; Cooks, R. G. Single oocyte and single embryo lipid analysis by desorption electrospray ionization mass spectrometry. *J. Mass Spec.* **2012**, *47*, 29-33.

(21) Loo, J. A., Quinn, J. P.; Ryu, S. I.; Henry, K. D.; Senko, M. W.; McLafferty, F. W. High-resolution tandem mass spectrometry of large biomolecules. *Proc. Natl. Acad. Sci. U. S. A.* **1992**, *89*, 286-289.

(22) Senko, M. W.; Speir, J. P.; McLafferty, F. W. Collisional activation of large multiply charged ions using Fourier transform mass spectrometry. *Anal. Chem.* **1994**, *66*, 2801-2808.

(23) Kelleher, N. L.; Lin, H. Y.; Valaskovic, G. A.; Aaserud, D. J.; Fridriksson, E. K.; McLafferty, F. W.; Top down versus bottom up protein characterization by tandem high-resolution mass spectrometry. *J. Am. Chem. Soc.* **1999**, *121*, 806-812.

(24) Ge, Y.; Lawhorn, B. G.; ElNaggar, M.; Strauss, E.; Park, J.-H.; Begley, T. P.; McLafferty, F. W. Top down characterization of larger proteins (45 kDa) by electron capture dissociation mass spectrometry. *J. Am. Chem. Soc.* **2002**, *124*, 672-678.

(25) Kelleher, N. L. Top-down proteomics. *Anal. Chem.* **2004**, *76*, 196A-203A.

(26) Chait, B. T. Mass spectrometry: Bottom-up or top-down? *Science* **2006**, *314*, 65-66.

(27) LeDuc, R. D.; Taylor, G. K.; Kim, Y. B.; Januszyk, T. E.; Bynum, L. H.; Sola, J. V.; Garavelli, J. S.; Kelleher, N. L. ProSight PTM: an integrated environment for protein identification and characterization by top-down mass spectrometry. *Nucleic Acids Res.* **2004**, *32*, W340-W345.

(28) Banerjee, I.; Zhang, J.; Moore-Morris, T.; Lange, S.; Shen, T.; Dalton, N. D.; Gu, Y.; Peterson, K. L.; Evans, S. M.; Chen, J. Thymosin beta 4 is dispensable for murine cardiac development and function. *Circ. Res.* **2012**, *110*, 456-464.

(29) Smith, C. A.; O'Maille, G.; Want, E. J.; Qin, C.; Trauger, S. A.; Brandon, T. R.; Custodio, D. E.; Abagyan, R.; Siuzdak, G. METLIN: a metabolite mass spectral database. *Ther. Drug Monit.* **2005**, *27*, 747-751.

(30) Horai, H.; Arita, M.; Kanaya, S.; Nihei, Y.; Ikeda, T.; Suwa, K.; Ojima, Y.; Tanaka, K.; Tanaka, S.; Aoshima, K.; Oda, Y.; Kakazu, Y.; Kusano, M.; Tohge, T.; Matsuda, F.; Sawada, Y.; Hirai, M. Y.; Nakanishi, H.; Ikeda, K.; Akimoto, N.; Maoka, T.; Takahashi, H.; Ara, T.; Sakurai, N.; Suzuki, H.; Shibata, D.; Neumann, S.; Iida, T.; Tanaka, K.; Funatsu, K.; Matsuura, F.; Soga, T.; Taguchi, R.; Saito, K.; Nishioka, T. MassBank: a public repository for sharing mass spectral data for life sciences. *J. Mass Spectrom.* **2010**, *45*, 703-714.

(31) Barrowma, J., Craig, M. Hæmoglobins of fœtal C57BL/6 Mice. *Nature* **1961**, *190*, 818-819.

(32) Stamatoyannopoulos, G. in *The Molecular Basis of Blood Diseases*, eds Stamatoyannopoulos, G.; Majerus, P. W.; Perlmutter, R. M.; Varmus, H. (W.B. Saunders) **2001**, pp 135-182.

(33) Manning, J. M.; Popowicz, A. M.; Padovan, J. C.; Chait, B. T.; Manning, L. R. Intrinsic regulation of hemoglobin expression by variable subunit interface strengths. *FEBS J.* **2012**, *279*, 361-369.

(34) Trimborn, T.; Gribnau, J.; Grosveld, F.; Fraser, P. Mechanisms of developmental control of transcription in the murine α- and β-globin loci. *Genes & Develop.* **1999**, *13*, 112-124.

(35) Simmons, D. A.; Wilson, D. J.; Lajoie, G. A.; Doherty-Kirby, A.; Konermann, L. Subunit disassembly and unfolding kinetics of hemoglobin studied by time-resolved electrospray mass spectrometry. *Biochemistry* **2004**, *43*, 14792-14801.

(36) Popp, R. A. Hemoglobins of mice: sequence and possible ambiguity at 1 position of alpha chain. *J. Mol. Biol.* **1967**, *27*, 9-16.

(37) Popp, R. A.; Bailiff, E. G.; Skow, L. C.; Whitney, J. B. The primary structure of genetic variants of mouse hemoglobin. *Biochem. Genet.* **1982**, *20*, 199-208.

(38) Popp, R. A. Sequence of amino-acids in beta chain of single hemoglobins from C57BL, SWR, and NB mice. *Biochim. Biophys. Acta* **1973**, *303*, 52-60.

(39) Ng, S.-C.; Locasale, J. W.; Lyssiotis, C. A.; Zheng, Y.; Teo, R. Y.; Ratanasirintrawoot, S.; Zhang, J.; Onder, T.; Unternaehrer, J. J.; Zhu, H.; Asara, J. M.; Daley, G. Q.; Cantley, L. C. Influence of threonine metabolism on s-adenosylmethionine and histone methylation. *Science* **2013**, *339*, 222-226.

(40) Lilja, T.; Heldring, N.; Hermanson, O. Like a rolling histone: epigenetic regulation of neural stem cells and brain development by factors controlling histone acetylation and methylation. *Biochim. Biophy. Acta* **2013**, *1830*, 2354-2360.

(41) Lugo, D. I.; Chen, S. C.; Hall, A. K.; Ziai, R.; Hempstead, J. L.; Morgan, J. I. Developmental regulation of beta-thymosin in the rat central nervous system. *J. Neurochem.* **1991**, *56*, 457-461.

(42) Sribenja, S.; Li, M.; Wongkham, S.; Wongkham, C.; Yao, Q.; Chen, C. Advances in thymosin beta 10 research: differential expression, molecular mechanisms, and clinical implications in cancer and other conditions. *Cancer Invest.* **2009**, *27*, 1016-1022.

(43) Goldstein, A. L.; Hannappel, E.; Sosne, G.; Kleinman, H. K. Thymosin β4: a multi-functional regenerative peptide. Basic properties and clinical applications. *Expert Opin. Biol. Ther.* **2012**, *12*, 37-51.

(44) Hall, A. K.; Hempstead J.; Morgan J. I. Thymosin beta-10 levels in developing human brain and its regulation by retinoic acid in the HTB-10 neuroblastoma. *Mol. Brain Res.* **1990**, *8*, 129-135.

(45) Yu, F. X.; Lin, S. C.; Morrisonbogorad, M.; Atkinson, M. A. L.; Yin, H. L. Thymosin beta-10 and thymosin beta-4 are both actin monomer sequestering proteins. *J. Biol. Chem.* **1993**, *268*, 502-509.

(46) Huff, T.; Muller, C. S. G.; Otto, A. M.; Netzker, R.; Hannappel, E. Beta-thymosins, small acidic peptides with multiple functions. *Int. J. Biochem. Cell Biol.* **2001**, *33*, 205-220.

(47) Mannherz, H. G.; Hannappel, E. The beta-thymosins: intracellular and extracellular activities of a versatile actin binding protein family. *Cell Motil. Cytoskeleton* **2009**, *66*, 839-851.

(48) Balaskas, N.; Ribeiro, A.; Panovska, J.; Dessaud, E.; Sasai, N.; Page, K. M.; Briscoe, J.; Ribes, V. Gene regulatory logic for reading the sonic hedgehog signaling gradient in the vertebrate neural tube. *Cell* **2012**, *148*, 273-284.

(49) Jessell, T. M. Neuronal specification in the spinal cord: Inductive signals and transcriptional codes. *Nature Rev. Genet.* **2000**, *1*, 20-29.

(50) Briscoe, J.; Sussel, L.; Serup, P.; Hartigan-O'Connor, D.; Jessell, T. M.; Rubenstein, J. L.; Ericson, J.; Homeobox gene Nkx2.2 and specification of neuronal identity by graded Sonic hedgehog signalling. *Nature* **1999**, *398*, 622-627.

(51) Chamberlain, C. E.; Jeong, J.; Guo, C.; Allen, B. L.; McMahon, A. P. Notochord-derived shh concentrates in close association with the apically positioned basal body in neural target cells and forms a dynamic gradient during neural patterning. *Development* **2008**, *135*, 1097-1106.

(52) Sasaki, N.; Kurisu, J.; Kengaku, M. Sonic hedgehog signaling regulates actin cytoskeleton via Tiam1-Rac1 cascade during spine formation. *Mol. Cell. Neurosci.* **2010**, *45*, 335-344.

(53) Watrous, J.; Roach, P.; Alexandrov, T.; Heath, B. S.; Yang, J. Y.; Kersten, R. D.; van der Voort, M.; Pogliano, K.; Gross, H.; Raaijmakers, J. M.; Moore, B. S.; Laskin, J.; Bandeira, N.; Dorrestein, P. C. Mass spectral molecular networking of living microbial colonies. *Proc. Natl. Acad. Sci. U. S. A.* **2012**, *109*, E1743-E1752.

(54) Zabrouskov, V.; Senko, M. W.; Du, Y.; Leduc, R. D.; Kelleher, N. L. New and automated MS^n approaches for top-down identification of modified proteins. *J. Am. Soc. Mass Spectrom.* **2005**, 16, 2027-2038.

(55) Mann, M.; Meng, C. K.; Fenn, J. B. Interpreting mass spectra of multiply charged ions. *Anal. Chem.* **1989**, *61*, 1702-1708.

(56) Berman, H. M.; Westbrook, J.; Feng, Z.; Gilliland, G.; Bhat, T. N.; Weissig, H.; Shindyalov, I. N.; Bourne, P. E. The protein data bank. *Nucleic Acids Res.* **2000**, *28*, 235-242.

(57) UniProt C. Reorganizing the protein space at the Universal Protein Resource (UniProt). *Nucleic Acids Res.* **2012**, *40*(Database issue), D71-D75.

(58) Kullander, K.; Butt, S. J.; Lebret, J. M.; Lundfald. L.; Restrepo, C. E.; Rydström, A.; Klein, R.; Kiehn, O. Role of EphA4 and EphrinB3 in local neuronal circuits that control walking. *Science* **2003**, *299*, 1889-1892.

(59) Lee, S. K.; Jurata L. W.; Funahashi J.; Ruiz E. C.; Pfaff S. L. Analysis of embryonic motoneuron gene regulation: derepression of general activators function in concert with enhancer factors. *Development* **2004**, *131*, 3295-3306.

(60) Banerjee, I.; I.; Zhang, J.; Moore-Morris, T.; Lange, S.; Shen, T.; Dalton, N. D.; Gu, Y.; Peterson, K. L.; Evans, S. M.; Chen, J. Thymosin beta 4 is dispensable for murine cardiac development and function. *Circ. Res.* **2012**, *110*, 456-464.

(61) Gilman, J. G.; Mouse haemoglobin beta chains. Sequence data on embryonic y chain and genetic linkage of the Y-chain locus to the adult beta-chain locus Hbb. *Biochem. J.* **1976**, *155*, 231-241.

(62) Shehee, W. R.; Loeb, D. D.; Adey, N. B.; Burton, F. H.; Casavant, N. C.; Cole, P.; Davies, C. J.; McGraw, R. A.; Schichman, S. A.; Severynse, D. M. Nucleotides sequence of the BALB/c mouse beta-globin complex. *J. Mol. Biol.* **1989**, *205*, 41-62.

(63) Shimma, S.; Setou, M. Mass microscopy to reveal distinct localization of heme B (m/z 616) in colon cancer liver metastasis. *J. Mass Spectrom. Soc. Jpn.* **2007**, *55*, 145-148.

Chapter 2 is a full reprint of the material as it appears in the published article of PNAS 2013, vol. 110, pp.14855-14860 by Cheng-Chih Hsu, Nicolas M. White, Marito Hayashi, Eugene C. Lin, Tiffany Poon, Indroneal Banerjee, Ju Chen, Samuel L, Pfaff, Eduardo. R. Macagno and Pieter C. Dorrestein. The thesis author was the primary author and investigator.

Chapter 3

Real-time Metabolomics on Living Microorganisms Using Ambient Electrospray Ionization Flow-Probe

3.1 Abstract

Microorganisms such as bacteria and fungi produce a variety of specialized metabolites that are invaluable for agriculture, biological research, and drug discovery. However, the screening of microbial metabolic output is usually a time intensive task. In Chapter 2 we implement a micro-junction flow-probe system, nanoDESI, to obtain the molecular information from the tissue surfaces. Here we utilize a similar liquid micro-junction surface sampling probe (LMJ-SSP) for electrospray ionization mass spectrometry to extract and ionize metabolite mixtures directly from living microbial colonies grown on soft nutrient agar in Petri-dishes without any sample pre-treatment. To demonstrate the method is robust, this technique was applied to observe the metabolic output of more than 30 microorganisms, including yeast, filamentous fungi, pathogens, and marine-derived bacteria, that were collected worldwide. Diverse natural products produced from different microbes, including *Streptomyces coelicolor*, *Bacillus subtilis*, and *Pseudomonas aeruginosa* are further characterized in this chapter.

3.2 Introduction

Microorganisms produce a wide array of specialized metabolites that phenotypically affect cell populations in their surroundings, a process known as metabolic exchange.[1] These exchange factors have a diverse array of functions: some act as signaling molecules that control metabolism and morphology, some are virulence factors or even cannibalistic factors, some serve as nutrients, and others function as antibiotic agents that promote the survival of the species.[1] Many of these specialized metabolites, such as penicillin and vancomycin, have been found to be of great clinical importance.[1] The ubiquity and variety of microbes generating compounds of such high potential utility presents a consequent challenge and opportunity. There are more than 10^5 formally named bacteria species in pure cultures and approximately twice as many uncultured species.[2,3] The total richness is estimated at 10^7 to 10^9 bacteria species worldwide.[3,4] Microbes also often co-exist with hosts such as humans: some of these microbial communities have been characterized at the nucleotide level.[5] Human microbiota play physiological roles and are thought to be associated with multiple disease states.[6] For example, a recent study indicates that the gut microbiome can drive hormonal regulation of human autoimmunity.[7] The ability to characterize metabolic exchange factors from agar grown microbial colonies facilitates the understanding of the roles of such specialized metabolites and their roles in virulence, symbiosis, and mutualism, yet there are very few tools available that can capture the chemistry of microbes in such a direct manner.

One of the most challenging aspects of investigating the chemistry of microbes in conventional mass spectrometric workflows is the time required for techniques such as

liquid chromatography mass spectrometry (LC-MS), to isolate individual molecular species. Matrix-assisted laser desorption ionization (MALDI) mass spectrometry can be applied to directly study microbial metabolic exchange eliminating the need for compound isolation.[8-10] However, the requisite crystalline organic matrix deposition and dehydration procedures involved in sample preparation inevitably deactivates microbial cellular activity. Recently, in order to investigate microbial metabolic profiles in real-time, an angled capillary liquid bridge based technique called nanospray desorption electrospray ionization (nanoDESI) was applied to the analysis of living microbial colonies.[11,12] This technique allows spatiotemporal profiling of metabolite output directly on Petri-dishes in ambient environments without a labor intensive purification process. Although nanoDESI works well for many microbiology applications, it is susceptible to loss of solvent flow through the liquid bridge due to the hydrophilicity of the extracellular matrix (ECM) of the microbes themselves and we have observed that high salinity media alters the electrospray behavior. Because nanoDESI has low flow rates and is self-aspirating, it makes it more sensitive to loss of flow by these factors. Clogging in the transfer capillary tube due to surface roughness is also more common during nanoDESI sampling. When this happens, the user will need to replace the capillary tube. Frequent capillary replacements and subsequent setup re-alignment makes the implementation of nanoDESI to untrained users more difficult at this time. For these reasons, a more effective operational approach to molecular information from microbes could, through increased robustness and automation, better deal with the demand for the analysis of the plethora of specialized metabolites produced by the diverse array of microbes that inhabit

our planet. Additional methods that complement nanoDESI to directly characterize the molecules of microbes grown on Petri-dishes need to be developed.

3.3 Flowprobe Instruments

Toward this end, we herein utilize a continuous flowprobe system, based on the coaxial tube geometry liquid microjunction surface sampling probe (LMJ-SSP), for continuous *in situ* extraction of an assortment of analytes, as it has previously been demonstrated for various qualitative and quantitative analysis of sample surfaces including glass slides, TLC plates, skin and tissues.[13-17] LMJ-SSP differs from nanoDESI in key operational aspects. LMJ-SSP mainly uses a pneumatic nebulizer instead of the self-aspirated nanospray capillary to extract analytes from samples (Figure 1a). LMJ-SSP has a co-axial geometry enabling analysis near the edges of the Petri-dishes. When clogging occurs in LMJ-SSP, this often can be remedied by a temporarily closing the nebulizer valve, resulting in a reversal of the solvent and nebulizer gas to flush the transfer tubes. Finally, LMJ-SSP uses higher flow rates than nanoDESI. As shown in Figure 3.1a, cultured microbial colony plates were sequentially placed onto an x-y stage (Figure 3.1b) below a z-axis translated probe body. As with all liquid extraction methods, the classes of molecules observed depends on the solvent used. In order to extract a broad range of microbially-secreted compounds, a 65/35 acetonitrile/0.1% formic acid aqueous solution (vol/vol) was used for all of the experiments, pumped at a rate of 5 μL/min through the probe to the surface and continuously aspirated away by the nebulizer (80 psi) operating at a high voltage (2 kV) for electrospray at a Thermo LTQ-FTICR MS inlet.

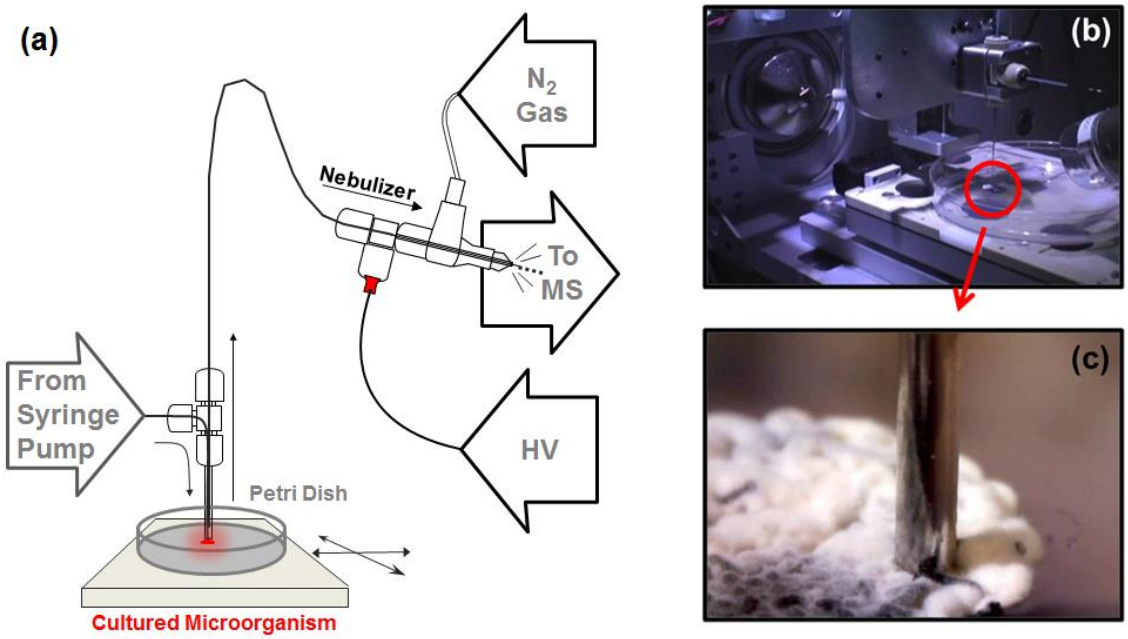

Figure 3.1 An overview of flowprobe based mass spectrometric analysis of living microorganisms on Petri dish. (a) Schematic diagram of MS analysis of microbial colonies using a coaxial LMJ-SSP method. Solvent is continuously pumped to the surface via the outer capillary tube to extract and mobilize the molecules on the colony and aspirated into the inner capillary tube by the Venturi force generated at the nebulizer where ions are electrosprayed at the MS inlet. (b) Photograph of the flowprobe prototype platform including the x-y stage. (c) Snapshot of the flowprobe desorbing metabolites from a colony of *S. coelicolor* A3(2).

3.4 Result and Discussion

3.4.1 Streptomyces coelicolor

Most microbes form biofilms (Figure 3.1c) making colony surfaces more heterogeneous than flat, evenly-deposited glass slides. Consequently computer controlled x-y, and z axes, respectively, were adjusted to move various colonies into the path of extraction, and maintain sufficient distance between the probe and surface at various plate locations, preserving colony morphologies. Supplemental movie (see online site here: https://www.youtube.com/watch?v=7vw1NOOyBxU) demonstrates the operation of the flowprobe when it contacts a Petri dish bearing colonies of the soil bacterium

Streptomyces coelicolor A3 (2) (Supplemental movie, bottom screen), and the mass spectrometer readout displays the instantaneous instrumental response. As shown in Supplemental movie (top screen) and Figure 3.2, the red-pigmented antibiotics prodiginines (*m/z* 392 and 394, cyclic and open forms) are detected upon flowprobe liquid junction contact with the colony and are further confirmed by MS/MS as Figure 3.3 and previous reports.[11]

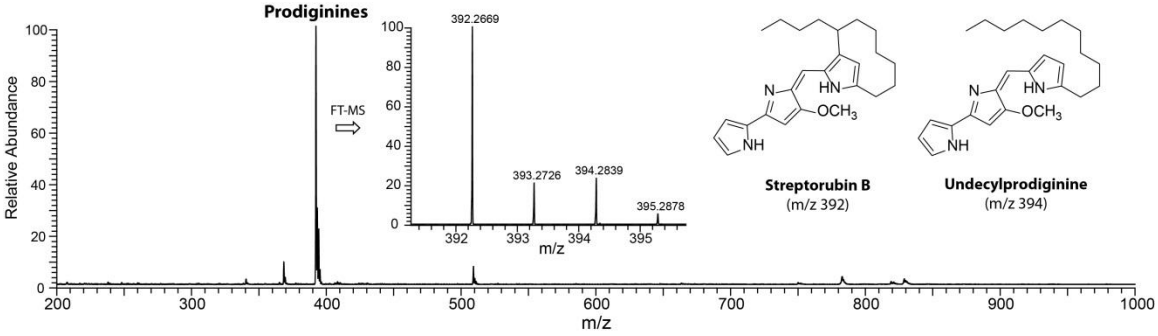

Figure 3.2 Mass spectrum acquired from the extract of the surface of *S. coelicolor* A3(2) colony. The peaks at *m/z* 392 and 394 are prodiginines as confirmed by fragmentation shown in the supporting information. *Inset*: expanded high-resolution FT-MS spectrum; mass errors: -7 ppm (streptorubin B) and -4 ppm (undecylprodigine). *Right*: molecular structures of cyclic and open ring prodiginines secreted by *S. coelicolor* A3(2).

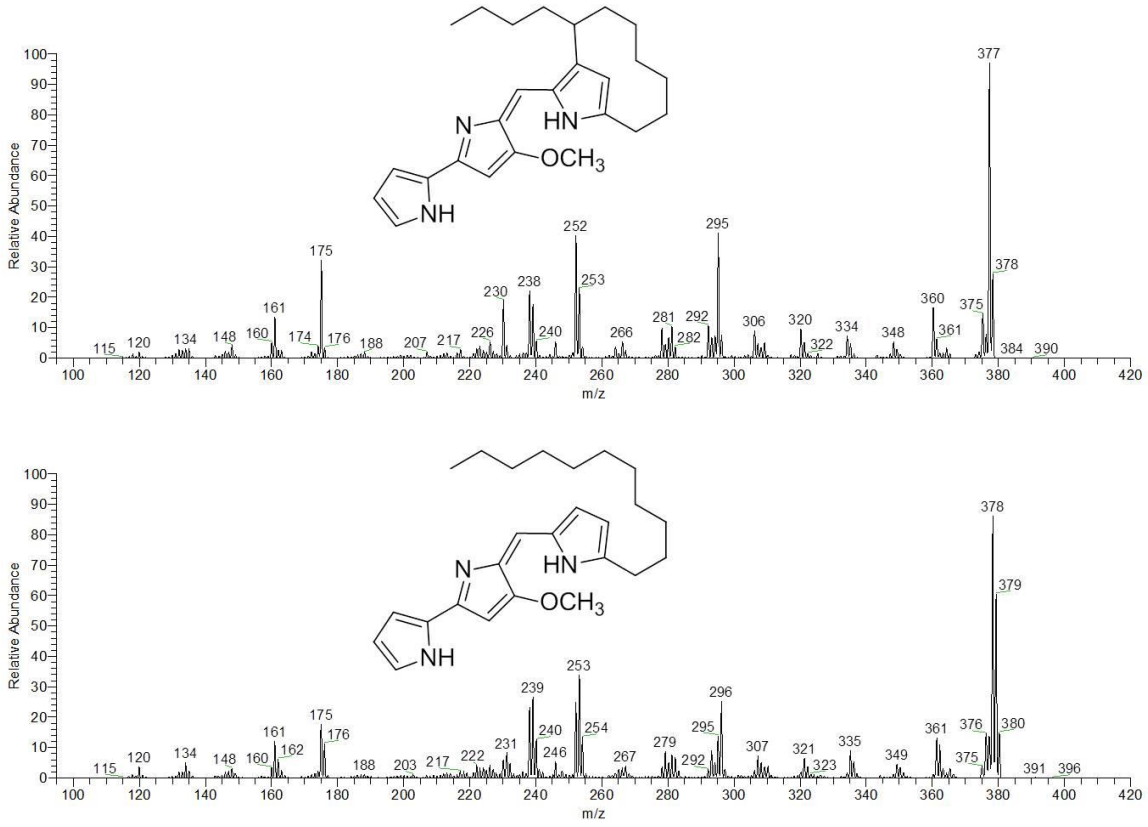

Figure 3.3 MS/MS validation of prodiginines (*m/z* 392 and 394) produced by *S. coelicolor* A3(2) using LMJ-SSP. The fragmentation products are consistent with the previous report published by Watrous et al.[11]

3.4.2 Bacillus subtilis

Specialized metabolites can be crucial for the survival of microorganisms subjected to harsh environmental conditions.[18] One such molecule is the nonribosomal peptide synthetase-derived surfactin, a lipopeptide antibiotic produced in 20 laboratory characterized strains of *B. subtilis* and found to possess antibacterial, antifungal, antiviral, and antimycoplasmic activity.[19,20] We cultured two *B. subtilis* strains: 3610 and PY79. *B. subtilis* PY79 is a laboratory domesticated strain of *B. subtilis* 3610 and most of the polyketide synthases and nonribosomal peptide synthetases have been silenced,[21] and

interrogated them using the flowprobe prototype. Surfactin analogs with different lipid chain lengths were identified from the colony surface of *B. subtilis* 3610 as shown in Figure 3.4 but, as expected, were not observed on *B. subtilis* PY79. These metabolomic results are consistent with reports in which mass spectrometry was used to highlight differences at the nucleotide level.[8,9,22,23]

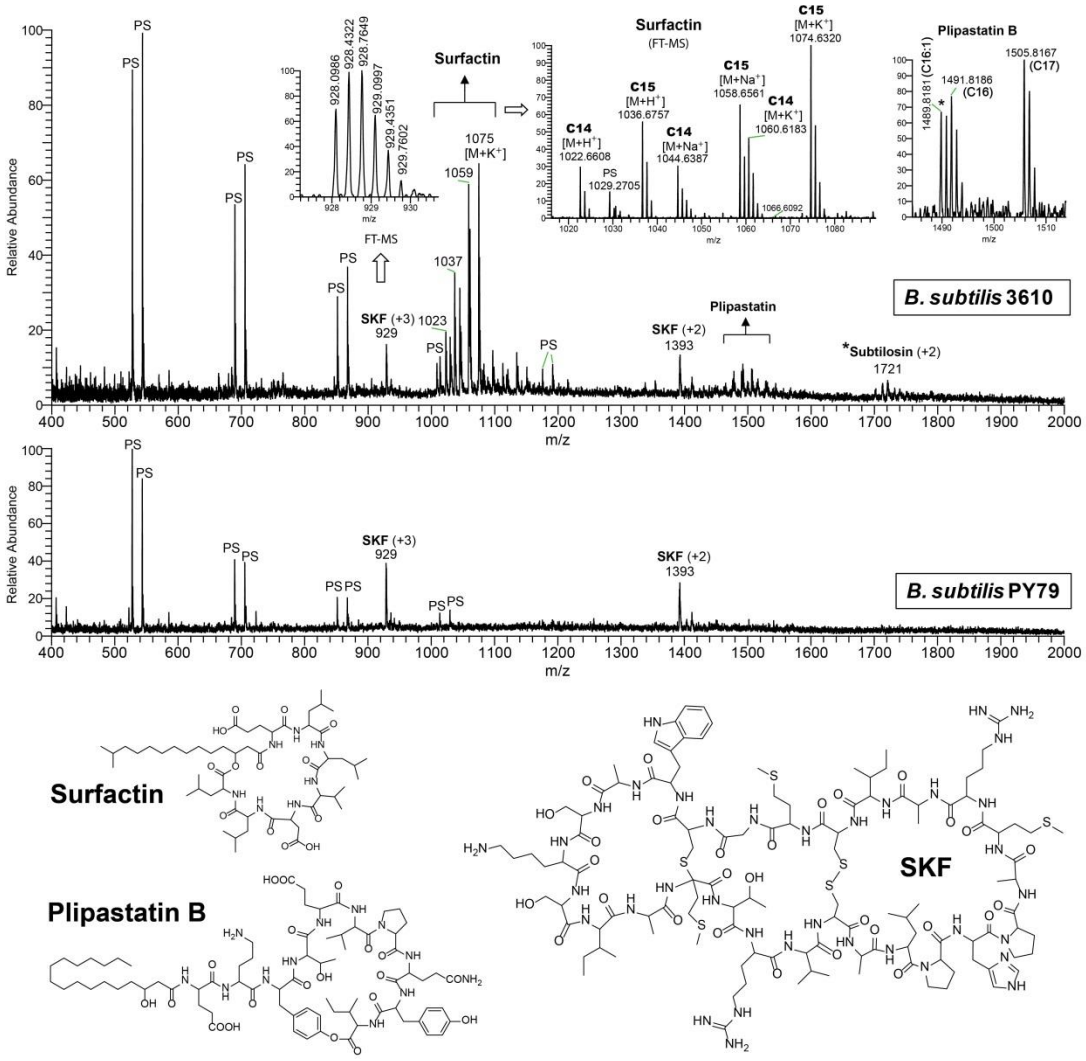

Figure 3.4 Analysis of *B. subtilis* wild-type and domesticated strains with flowprobe prototype. *Top*: Mass spectrum acquired on the surface of *B. subtilis* 3610 and PY79 biofilm. *Inset*: high resolution expanded FT-MS spectra of annotated metabolites secreted by *B. subtilis* 3610. The peaks for surfactin, plipastatin and SKF are confirmed by MS/MS as shown in the supporting information. Putative annotations are denoted with an asterisk. Ions of polysaccharides are labeled (PS). *Bottom*: structures of the found metabolites.

In addition to surfactin, other cyclic peptides such as plipastatin[24] and subtilosin were observed from *B. subtilis* 3610 but not *B. subtilis* PY79 (Figure 3.4). At different stages during the growth of a *B. subtilis* colony, bacterial cells differentiate in order to carry out multiple functions that enable adaptation to environmental changes. Individual cell fate in *B. subtilis* is coordinated by many biosynthesized chemical agents. Recently, a sporulation killing factor (SKF) that determines cannibalistic behavior was identified on the colonies of *B. subtilis* strains using MALDI-TOF-IMS.[9] These ribosomal peptides were also observed in the 2+ and 3+ charge states on both *B. subtilis* analyzed strains, as shown in Figure 3.3. Polysaccharide derived signals, possibly from degraded agarose, were also abundant on both colonies. The comparison of MS performance using LMJ-SSP and nanoDESI are also shown in Figure 3.5.

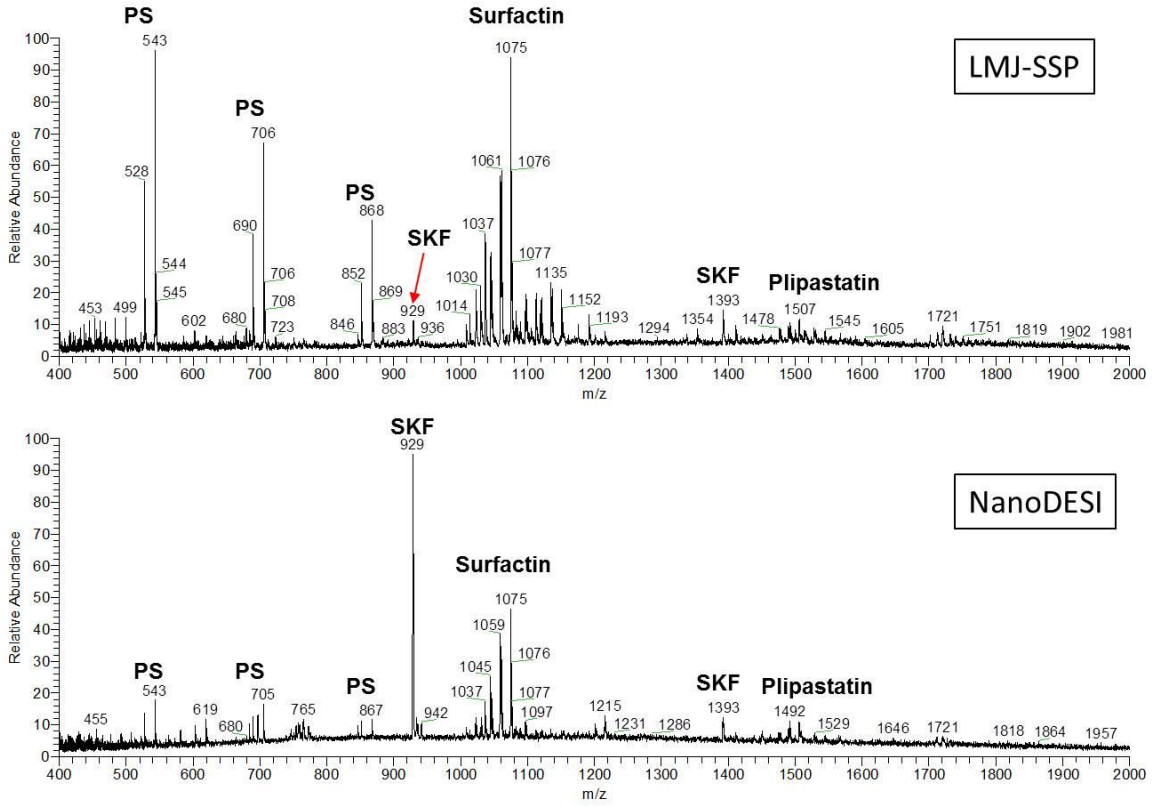

Figure 3.5 Mass spectra acquired on the surface of *B. subtilis* 3610 biofilm using LMJ-SSP and nanoDESI. The result shows that all of the cyclic peptides produced by *B. subtilus* 3610 measured via LMJ-SSP are also found via nanoDESI. PS = polysaccharide from the agar. MS spectra of *B. subtilus* 3610 measure by MALDI have published elsewhere.[8,9]

3.4.3 Pseudomonas aeruginosa

Metabolic exchange is not unique to microbial communities and is also observed in the context of commensal, mutualistic, competitive, and antagonistic microbe-eukaryote systems and microbe-host interactions. Alteration of metabolic signaling agents has been demonstrated to correspond with disease progression. The opportunistic pathogen *Pseudomonas aeruginosa*,[25] which is commonly isolated from the lungs of cystic fibrosis (CF) patients,[26] secretes several virulence factors including pyocyanine (PYO).[27] Furthermore, the capacity for fungal inhibition by *P. aeruginosa* is also

associated with its secondary metabolites. To further illustrate the utility of this technique in pathogen analysis, we describe the metabolomic profiling of a cultured *P. aeruginosa* PA14 colony. As shown in Figure 3.6, both virulence factor ions (PYO with H^+ and Na^+ adducts) as well as its biosynthetic precursor phenazine-1-carboxylic acid (PCA) were identified. The elongated conjugated system of the PYO cation stabilizes the ESI product and explains the higher PYO intensity relative to PCA signal at *m/z* 225.[28] Within the same fingerprint range of *m/z* 240-320, a diverse array of quinolone molecules, including *Pseudomonas* quinolone signaling molecule 2-heptyl-3-hydroxy-4-quinolone (PQS) and related molecules with different carbon chain lengths were obtained. These molecules play a crucial role as signaling molecules in the quorum sensing network of *Pseudomonas aeruginosa*.[29,30] Above *m/z* 500, extensive rhamnolipid production was identified, exemplified by the sodiated mono-and di-rhamnolipid congeners, seen at *m/z* 527 and 673, respectively. These glycolipidic biosurfactants assist in the biodegradation of insoluble media; are associated with biofilm formation and swarming behavior; and act as virulence factors against a variety of microorganisms, such as the fungus *Candida albicans*.[31,32]

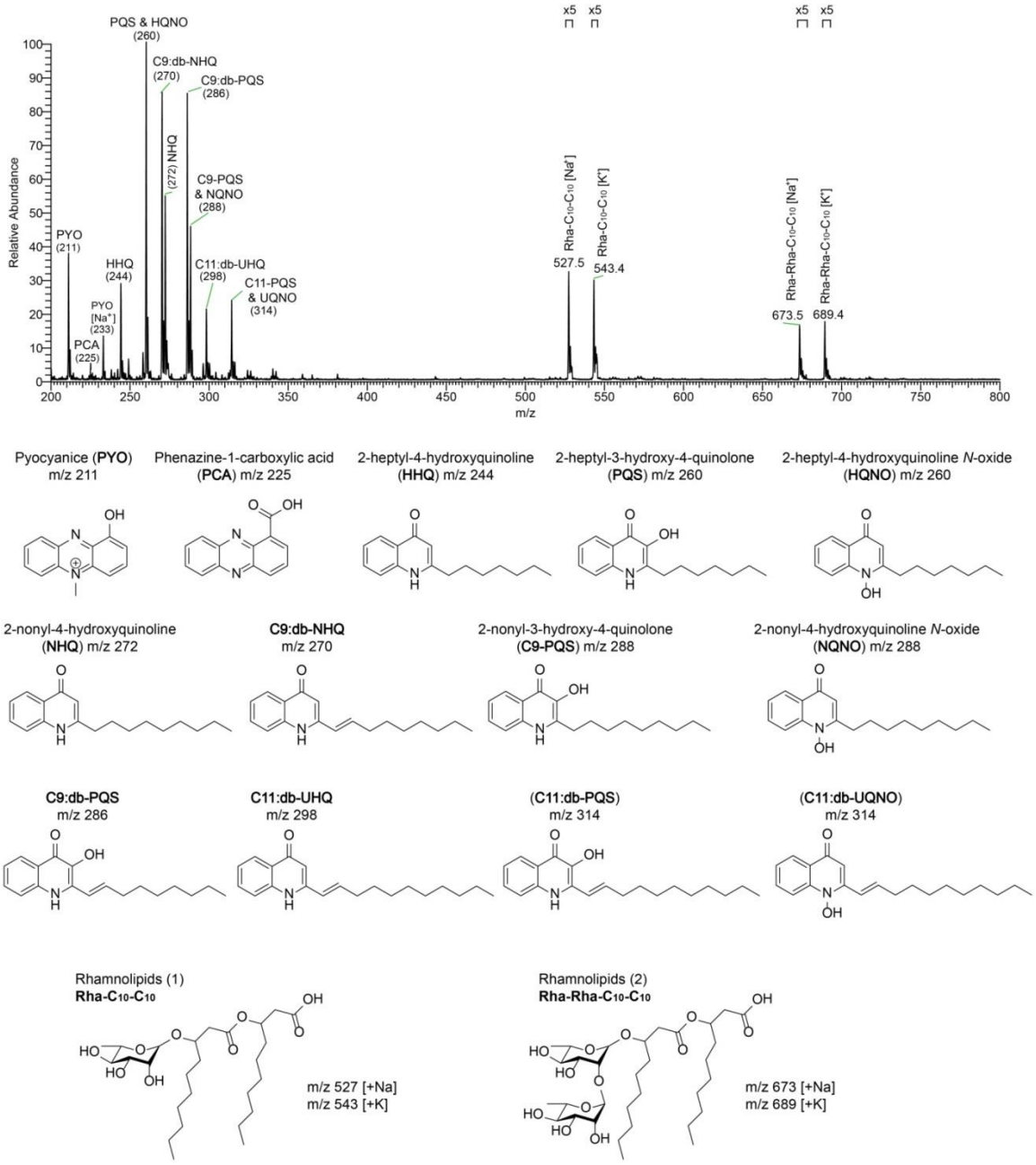

Figure 3.6 Analysis of pathogen *P. aeruginosa* PA14 biofilm using the flowprobe system. *Top*: Mass spectrum acquired during continuous extraction of surface of *P. aeruginosa* PA14 colony showing phenazines, quinolones and rhamnolipids that are secreted by *P. aeruginosa* PA14. *Bottom*: molecular structures of the metabolites identified.

3.4.4 Metabolomics of Microorganisms: Global Investigation

Utilizing the flowprobe system for direct colony extraction and ionization, diverse classes of natural products, ranging from small redox compounds,[33] quorum sensing signaling molecules,[29,30] glycolipidic antifungal[31,32] and red-pigmented anticancer agents,[34] to nonribosomal peptidic antibiotics[19,20] and ribosomally-encoded peptidic cell differentiation inducers,[9,35,36] were identified. Early success with various bacterial genera encouraged exploring a wider scope of microbial diversity. Thirty four bacterial and fungal strains isolated from worldwide sources including CF patients (San Diego, USA), bats (caves and abysses in the Czech Republic),[37] cheese,[38] marine habitats (distinct geographical areas from Solomon Islands to South China Sea),[39-41] and symbiotic lichens (Canada) were cultured and investigated using this approach. As elaborated in Figure 3.7, flowprobe mass spectra from each strain were acquired up to *m/z* 2000 showing multiplex spectral features that illustrate sharp diversity of metabolomic profiles. Polysaccharide ions (with characteristic 162 Da repeating units) are commonly found among some of these colonies as well as *B. subtilis* (Figure 3.4), possibly as a result of agar biodegradation. These media-derived molecules contribute to the cross-genera background (mutual) ions. However, molecules detected exclusively within the same genera, such as ion clusters at *m/z* 564, 692 and 1400 in *Serratia*, enable discernment of spectral patterns of genetically related species.

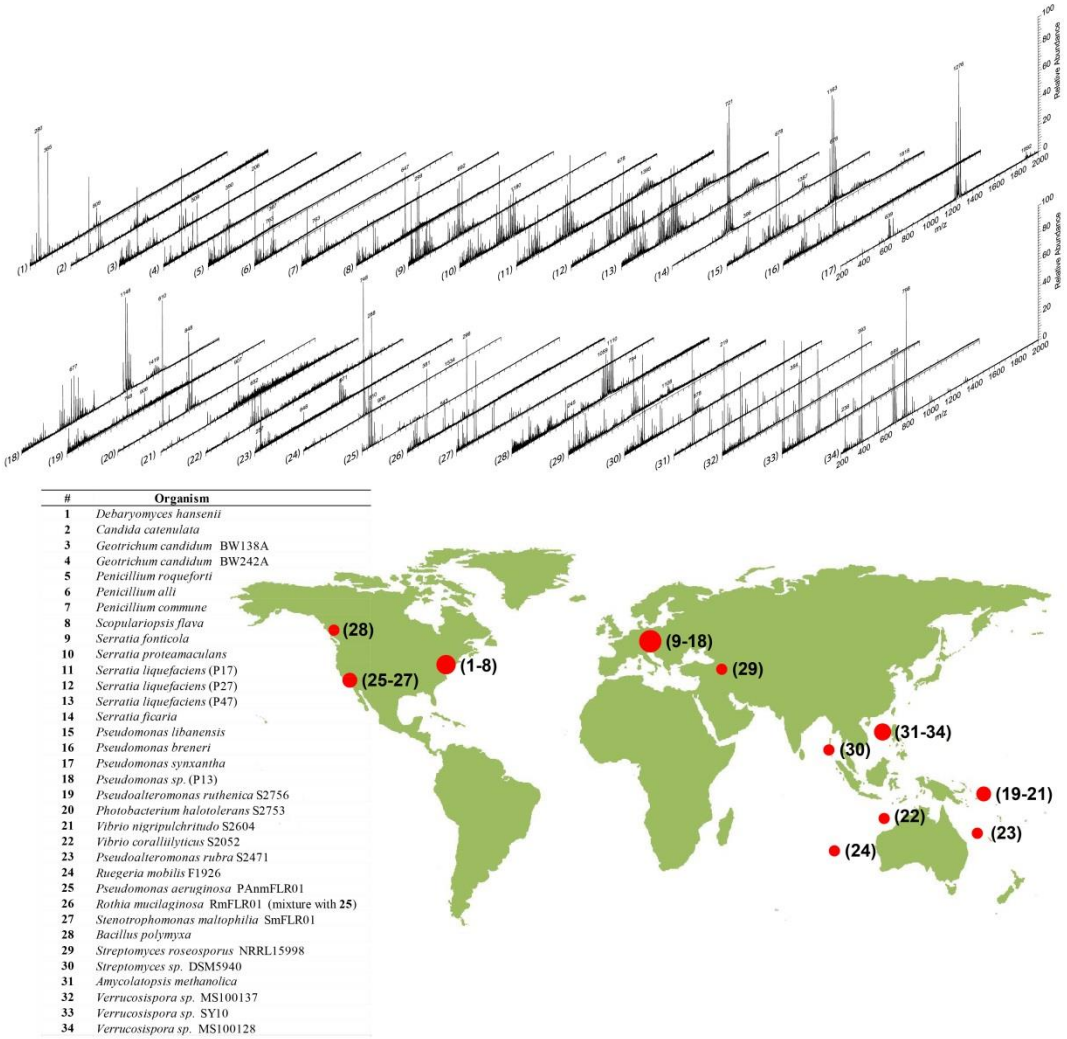

#	Organism
1	*Debaryomyces hansenii*
2	*Candida catenulata*
3	*Geotrichum candidum* BW138A
4	*Geotrichum candidum* BW242A
5	*Penicillium roqueforti*
6	*Penicillium alli*
7	*Penicillium commune*
8	*Scopulariopsis flava*
9	*Serratia fonticola*
10	*Serratia proteamaculans*
11	*Serratia liquefaciens* (P17)
12	*Serratia liquefaciens* (P27)
13	*Serratia liquefaciens* (P47)
14	*Serratia ficaria*
15	*Pseudomonas libanensis*
16	*Pseudomonas breneri*
17	*Pseudomonas synxantha*
18	*Pseudomonas sp.* (P13)
19	*Pseudoalteromonas ruthenica* S2756
20	*Photobacterium halotolerans* S2753
21	*Vibrio nigripulchritudo* S2604
22	*Vibrio coralliilyticus* S2052
23	*Pseudoalteromonas rubra* S2471
24	*Ruegeria mobilis* F1926
25	*Pseudomonas aeruginosa* PAnmFLR01
26	*Rothia mucilaginosa* RmFLR01 (mixture with **25**)
27	*Stenotrophomonas maltophilia* SmFLR01
28	*Bacillus polymyxa*
29	*Streptomyces roseosporus* NRRL15998
30	*Streptomyces sp.* DSM5940
31	*Amycolatopsis methanolica*
32	*Verrucosispora sp.* MS100137
33	*Verrucosispora sp.* SY10
34	*Verrucosispora sp.* MS100128

Figure 3.7 Real-time mass spectra acquired on the surfaces of diverse microbial colonies. *Bottom*: List of microorganisms and original locations of the strain isolations. Note that the numbers in the parentheses of strain #11-13 and 18 are referential numbers for mass spectrometry analysis not formal strain names.

3.5 Perspective

The resulting MS fingerprints from this initial multi-species dataset generated by the flowprobe suggest the feasibility of the conceptual microbiology scheme for rapid identification of microbial species based on chemical output similarity. This workflow has been nicely implemented on a small scale, mostly with pathogenic microbes, via MALDI or DESI-MS using individual algorithms.[42-45]

Of utmost interest, is the high efficiency real-time microbial metabolite screening afforded by the development of the technique. Previously, Watrous et al. demonstrated a new method of viewing secreted microbial products by deconvoluting the mass spectrometry fragmentation features of parent ions mobilized from the colony surface.[11] Via this approach, structurally related molecules, presented as nodes, are mapped based on corresponding spectral similarity. This powerful tool provides system-wide molecular information and represents a new frontier in metabolomic methodology. As more extensive MS/MS datasets are collected and mapped, a novel molecule or metabolite with a characterized fragmentation pattern can be located in the "pseudospace" of a broader molecular network that is progressively increasing in strain coverage and scale.

However, one of the biggest obstacles of the molecular identification using tandem MS-based databases is instrument-dependent fragmentation mismatching. Variations between each laboratory and ionization method create imprecision in MS databases and subsequently, ambiguity during spectral comparisons. Identical molecules could possibly have very different fragmentation spectra in terms of product ions and intensities simply due to a minor change in operating parameters.[46-48] Establishing an universal standard protocol for all natural product MS analysis will improve instrument-

dependent data ambiguity and, more importantly, will make spectral comparison processing more efficient and convincing. **The ease of the flowprobe system provides a solution to standardize the MS acquisition step on microbial colonies directly from Petri-dishes.** Most importantly, the capability of rapid surface profiling in real-time circumvents the need for labor-intensive and time-consuming procedures to improve the speed with which microbial samples from the clinic or biotechnological applications can be screened, perhaps for genus identification, fundamental biofilm studies but certainly for the discovery of specialized metabolites.

3.6 Methods and Experiments

3.6.1 Instrumental

The experimental parameters of LMJ-SSP have been described in Section 3.3. The nanoDESI setup was described in Chapter 2. The solvent system for both setups were both 65/35 acetonitrile/0.1% formic acid aqueous solution, solvent choices were based on extractive procedures already used with other extractive based techniques to microbial metabolomics studies.[11,49] Both ionization sources were coupled to a 6.4 T Finnigan LTQ-FT-ICR MS (Thermo-Electron Corporation, San Jose, CA) that is capable of collision-induced dissociation. All analyses were performed in positive ion mode in the mass range of *m/z* from 200 to 2,000. The instrument scan cycle consisted of two segments. The first segment had two profile mode MS scans: one full scan in the IT mode with 200 ms max fill time as the dependent scan; one full scan in the FT cell (50,000 resolution) with 2 sec max inject time. The second segment followed by a data-dependent tandem mass acquisition consisted of 8 scans in a cycle with a $\Delta m/z$ = 3 isolation

window. These data-dependent scans (IT mode, profile spectra) consisted of a maximum 1000 ms fill time, 35% normalized collision energy, 0.25 activation Q, and 0.05 s activation time. Data were acquired for 15 minutes for each microbial plate.

3.6.2 Preparation of Microbial Colonies

Bacillus subtilis and *Streptomyces coelicolor*

B. subtilis 3610/PY79 and *S. coelicolor* A3(2) colonies were prepared by inoculating 1 μL of liquid cultures (*B. subtilis*) and harvested spores (*S. coelicolor*) onto ISP2 nutrient agar (7.5 g agar, 5 g malt extract, 2 g yeast extract, and 2 g dextrose in 500 mL milli-Q water) and allowed to grow for 54 hours at the 30 ℃ incubator. *B. subtilis* 3610/PY79 liquid cultures were first prepared by inoculating 1 μL of cell stock into 4 mL of LB broth and incubated at 30 ℃ until an OD_{600} of 0.4 was reached. *B. subtilis* 3610 was originally acquired from Bacillus Genetic Stock Center (BGSC) (Ohio State Univ., Columbus), collected as Marburg strain by Robert S. Breed, chief bacteriologist at the Geneva station.[21] *B. subtilis* PY79 was first isolated when the auxotrophic markers of strain CU1769 (*glnA100* and *metB5*) were removed by two cycles of PBS1-mediated transduction, using lysates grown on strain 168.[21,50] *Streptomyces coelicolor* A3(2) is the model representative of a group of soil-dwelling organism with a complex lifecycle involving mycelial growth and spore formation.

Pseudomonas aeruginosa PA14

Pseudomonas aeruginosa PA14 came from the D. Hung lab (Harvard Medical School, USA) and originated from F.M. Ausubel's lab (Massachusetts General Hospital,

USA). *P. aeruginosa* PA14 was inoculated on ISP2 agar (10 mL) in Petri dish. The sample was incubated for 48 hours at 30 ^{o}C.

Yeasts and Filamentous Fungi

Yeasts (**1**-**4**) and filamentous fungi (**5**-**8**) strains were isolated from variant cheese sources that were made by Jasper Hill Farm in Greensboro, Vermont. The strains were identified using the ribosomal internal transcribed spacer (ITS) region. Purified fungal colonies were grown and maintained on PCAMS agar plates (5 g tryptone, 2.5 g yeast, 1 g dextrose, 1 g whole milk powder, 10 g NaCl, 15 g agar) at 25 ^{o}C for 3 weeks before mass spectrometry analysis.

Bat-associated strains (Serratia and Pseudomonas)

Serratia (**9**-**14**) and *Pseudomonas* (**15**-**18**) strains were isolated from several bat species collected from caves in Czech Republic by swabbing and were identified by 16S rRNA gene sequence analysis. Strains were prepared by inoculation onto ISP2 nutrient agar and allowed to grow for 28 days at 10 ℃.

Marine bacterial strains

Marine strains **19**-**24** were acquired from the Galathea 3 expedition strain collection.[39] *Pseudoalteromonas ruthenica* S2756 (**19**) and *Photobacterium halotolerans* S2753 (**20**) were isolated from swabs of mussel collected near the Solomon Islands. *Vibrio nigripulchritudo* S2604 (**21**) was isolated from the Solomon Sea. *Vibrio coralliilyticus* S2052 (**22**) was isolated from the sediment in the Indian Ocean northwest to Australia. *Pseudoalteromonas rubra* S2471 (**23**) was isolated near Coral sea. *Ruegeria mobilis* F1926 (**24**) was isolated from the Indian Sea. Strains were grown on Marine Agar

2216 (MA, BD DifcoTM) for 48 hours at room temperature. Then cultured in agitated Marine Broth 2216 (MB, BD DifcoTM) before spotting 20 μL on an MA plate, which was inoculated for 24 hours at room temperature.

Marine strains **31-34** were isolated using oatmeal agar from a sediment sample collected in April 2010 from the South China Sea (20° 9.795′ N, 118° 18.124′ E) at 2733 m below sea level and were identified as *Amycolatopsis methanolica* (**31**) and *Verrucosispora* spp. (**32**-**34**), respectively, using 16S rRNA gene sequence analysis. These strains were cultivated on ISP2 agar medium at 28℃ for 7 days before mass spectrometry analysis.

Cystic Fibrosis related strains

Bacterial isolates PAnmFLR01 (**25**) and SmFLR01 (**27**) were obtained by culturing on various selective media at the UCSD adult CF clinic clinical lab, La Jolla, CA. The isolates were identified as *Psuedomonas aeruginosa* and *Stenotrophomonas maltophilia* by phenotypic methods and then sent to the Rohwer lab at San Diego State University for culturing. *Rothia mucilaginosa* strain RmFLR01 (**26**) was obtained by initial culturing of a patient's sputum on the gram-positive selective media CN agar. Single colonies were verified as *R. mucilaginosa* by 16S rRNA gene sequence analysis. Isolates were maintained on Todd Hewitt agar at 37℃ after initial isolation. Prior to the mass spectrometry analysis the bacteria were grown on ISP2 media for 48 hours.

Streptomyces roseosporus and Streptomyces sp. DSM5940

Streptomyces roseosporus NRRL 15998 (**29**) was acquired from the Broad institute, MIT/Harvard, MA, USA, whose parent strain *S. roseosporus* NRRL 11379 was

isolated from soil from Mount Ararat in Turkey. *Streptomyces sp.* DSM5940 (**30**) was originally isolated from a soil sample collected from the Andaman Islands, India.[51] Both strains were maintained and grown on ISP2 nutrient agar medium. The cultures were incubated for 4 days at 30 ℃ before mass spectrometry analysis.

Bacillus polymyxa

Bacillus polymyxa (**28**) obtained from Davies lab (The University of British Columbia). The strain were grown and maintained on ISP2 agar medium at room temperature for 25 days before mass spectrometry analysis.

3.7 Supporting Information

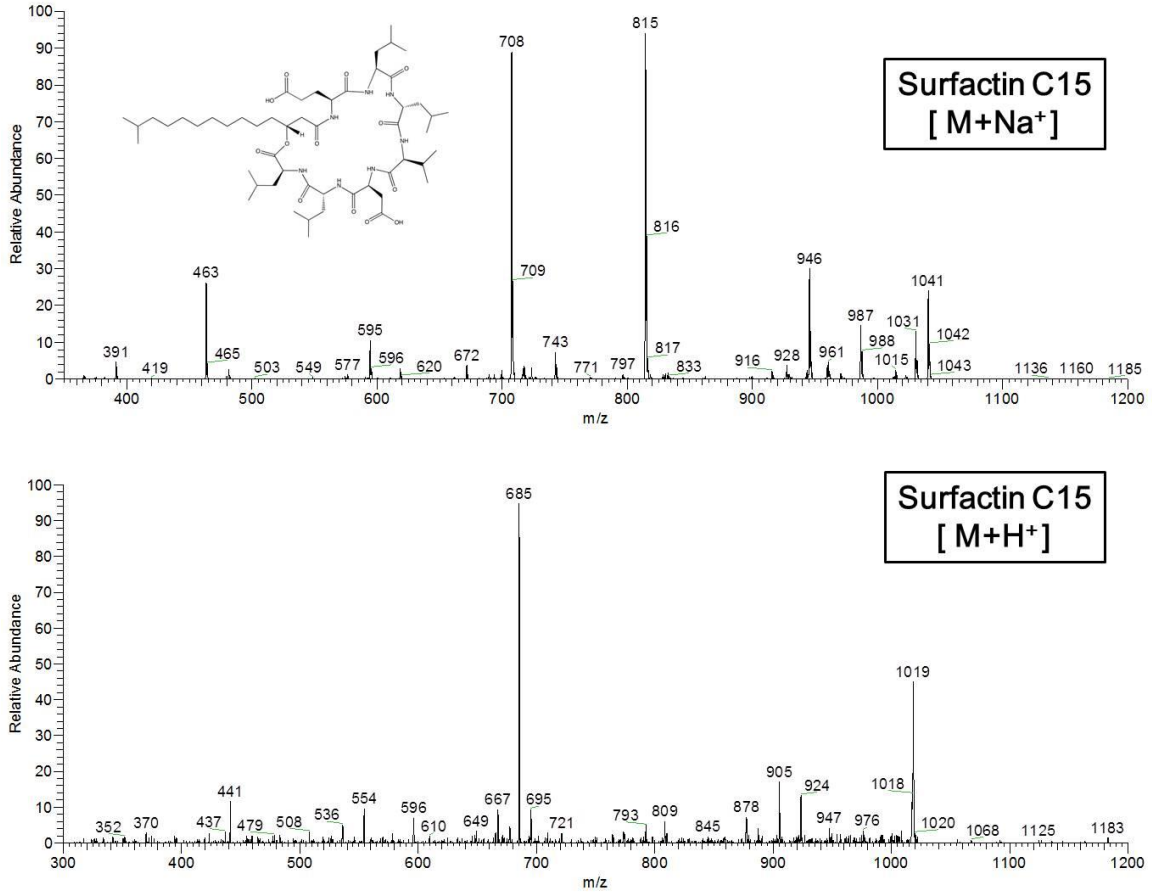

Figure 3.8 MS/MS validation of surfactin (*m/z* 1037 and 1059, H^+ and Na^+ adducts respectively) secreted by *B. subtilis* 3610 using LMJ-SSP. The fragmentation products are consistent with the previous report published by Watrous et al. (H^+) and Song et al. (Na^+).[11,22]

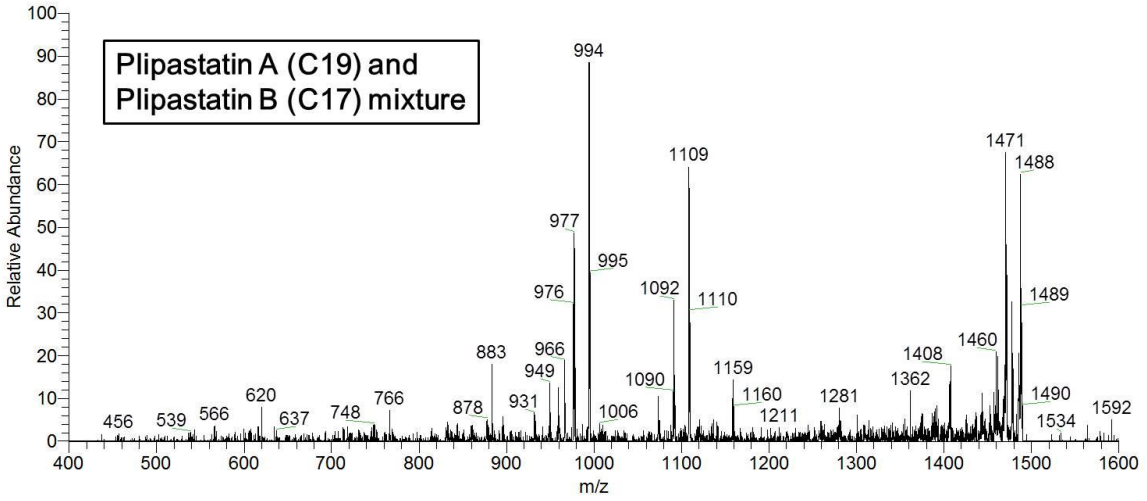

Figure 3.9 MS/MS validation of plipastatin mixture (*m/z* 1506) produced by *B. subtilis* 3610 using LMJ-SSP. The fragmentation products are consistent with the previous report published by Watrous et al.[11]

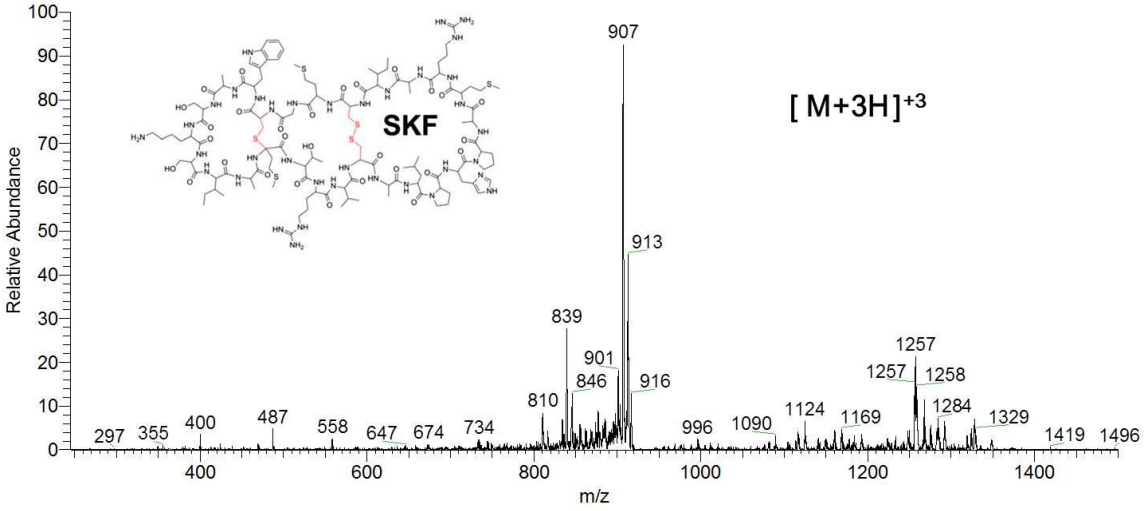

Figure 3.10 MS/MS validation of SKF (*m/z* 928) produced by *B. subtilis* PY79 using LMJ-SSP. The fragmentation products are consistent with the previous report published by Watrous et al. and Liu et al. using purified SKF.[11,9]

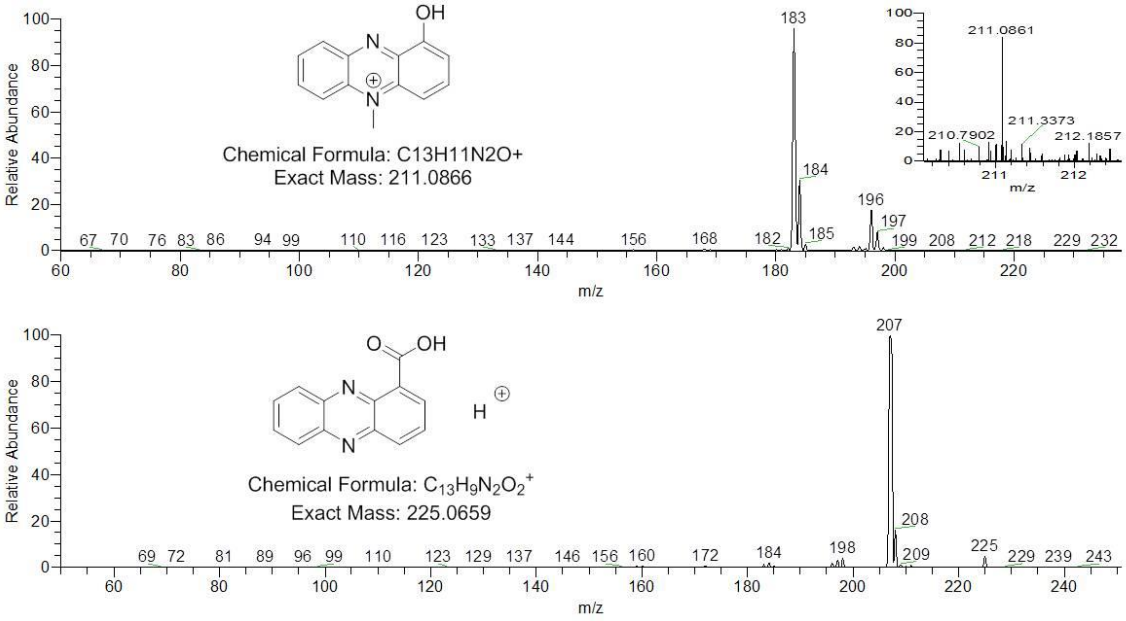

Figure 3.11 MS/MS validation of two phenazines, PYO (*m/z* 211) and PCA (*m/z* 225) produced by *P. aeruginosa* PA14 using LMJ-SSP. The fragmentation products are consistent with the previous report published by Moree et al. using purified compounds.[10] *Inset*: high-resolution FT-MS spectrum of PYO parent ion. Mass error: -2 ppm.

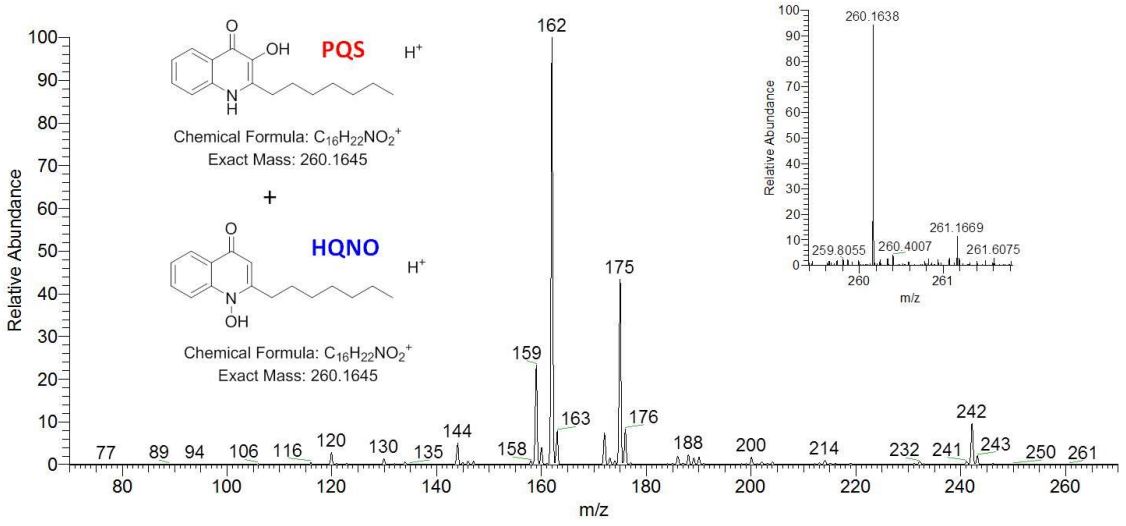

Figure 3.12 MS/MS validation of PQS and HQNO mixture (*m/z* 260) produced by *P. aeruginosa* PA14 using LMJ-SSP. The fragmentation products are consistent with the previous report published by Moree et al.[10] *Inset*: high-resolution FT-MS spectrum of parent ion. Mass error: -2 ppm.

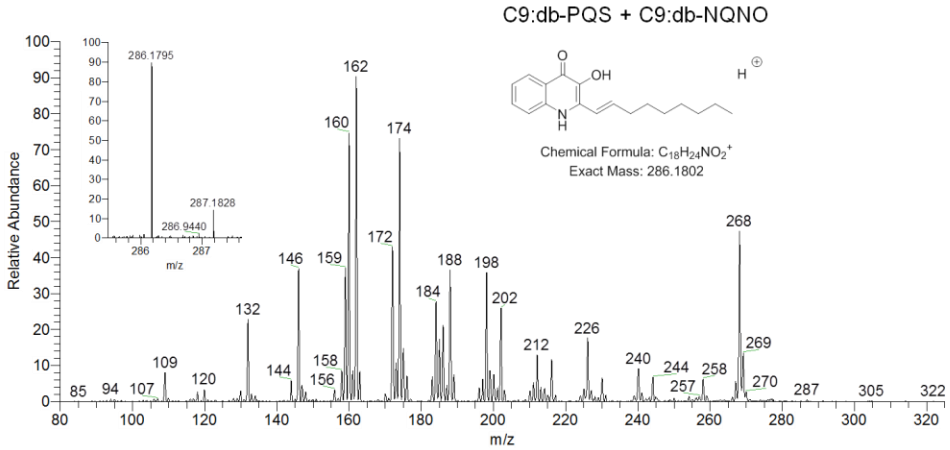

Figure 3.13 MS/MS validation of C9:db-PQS and C9:db-HQNO (structure not shown) mixture (*m/z* 286) produced by *P. aeruginosa* PA14 using LMJ-SSP. The fragmentation products are consistent with the previous report published by Moree et al.[10] *Inset*: high-resolution FT-MS spectrum of parent ion. Mass error: -2 ppm.

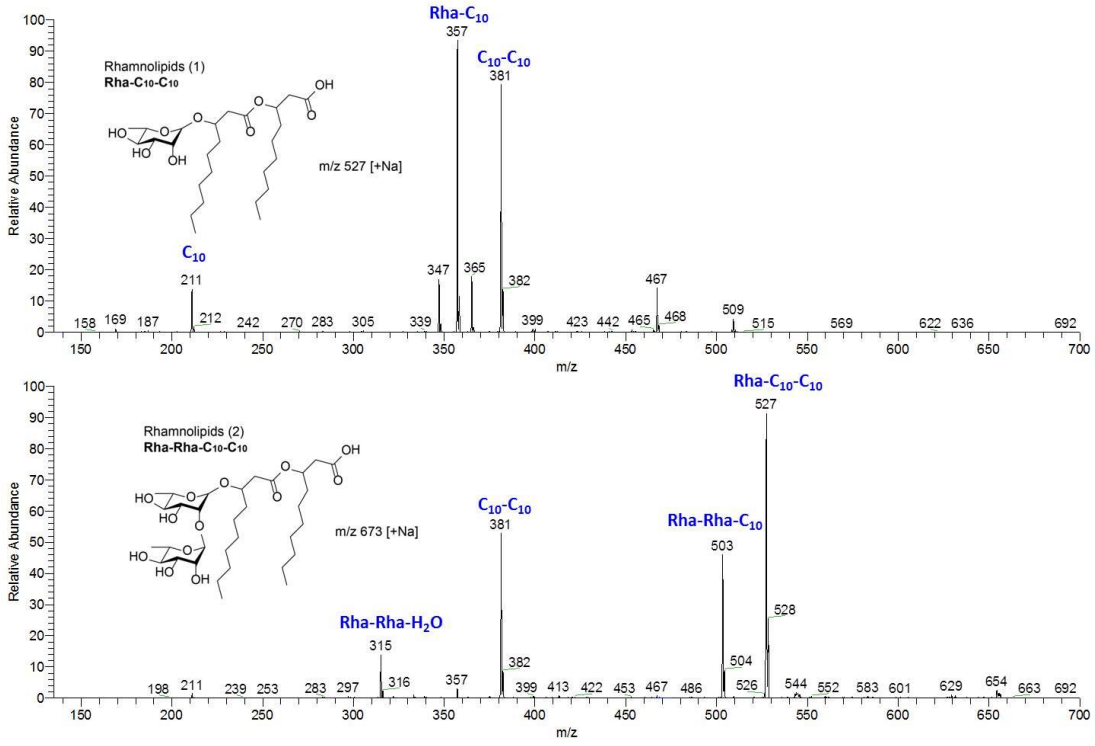

Figure 3.14 MS/MS validation of rhamnolipids produced by *P. aeruginosa* PA14 using LMJ-SSP. The fragmentation products are consistent with the previous reports for rhamnolipids.[10,32]

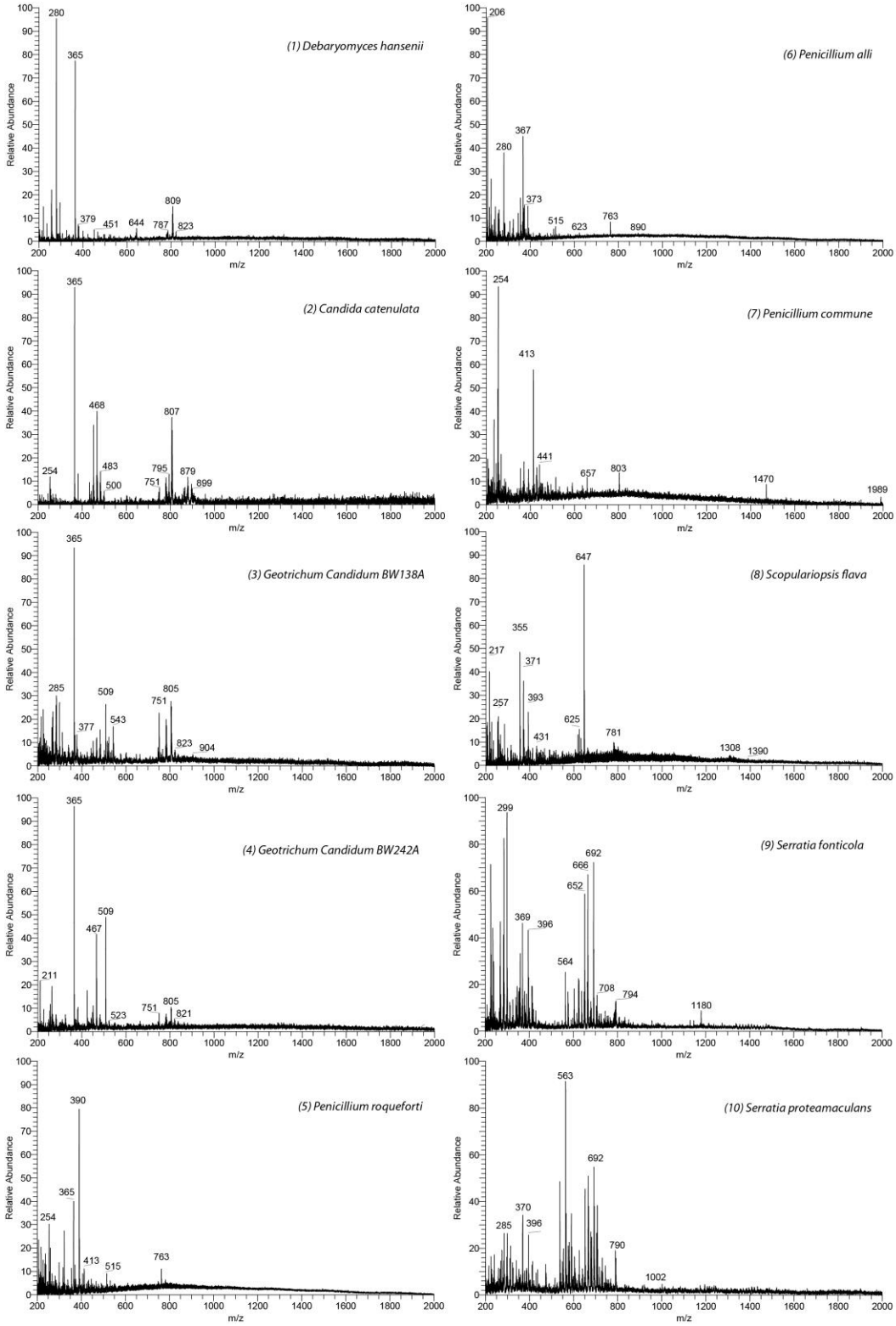

Figure 3.15 Real-time mass spectra acquired on the surfaces of diverse microbial colonies 1-34.

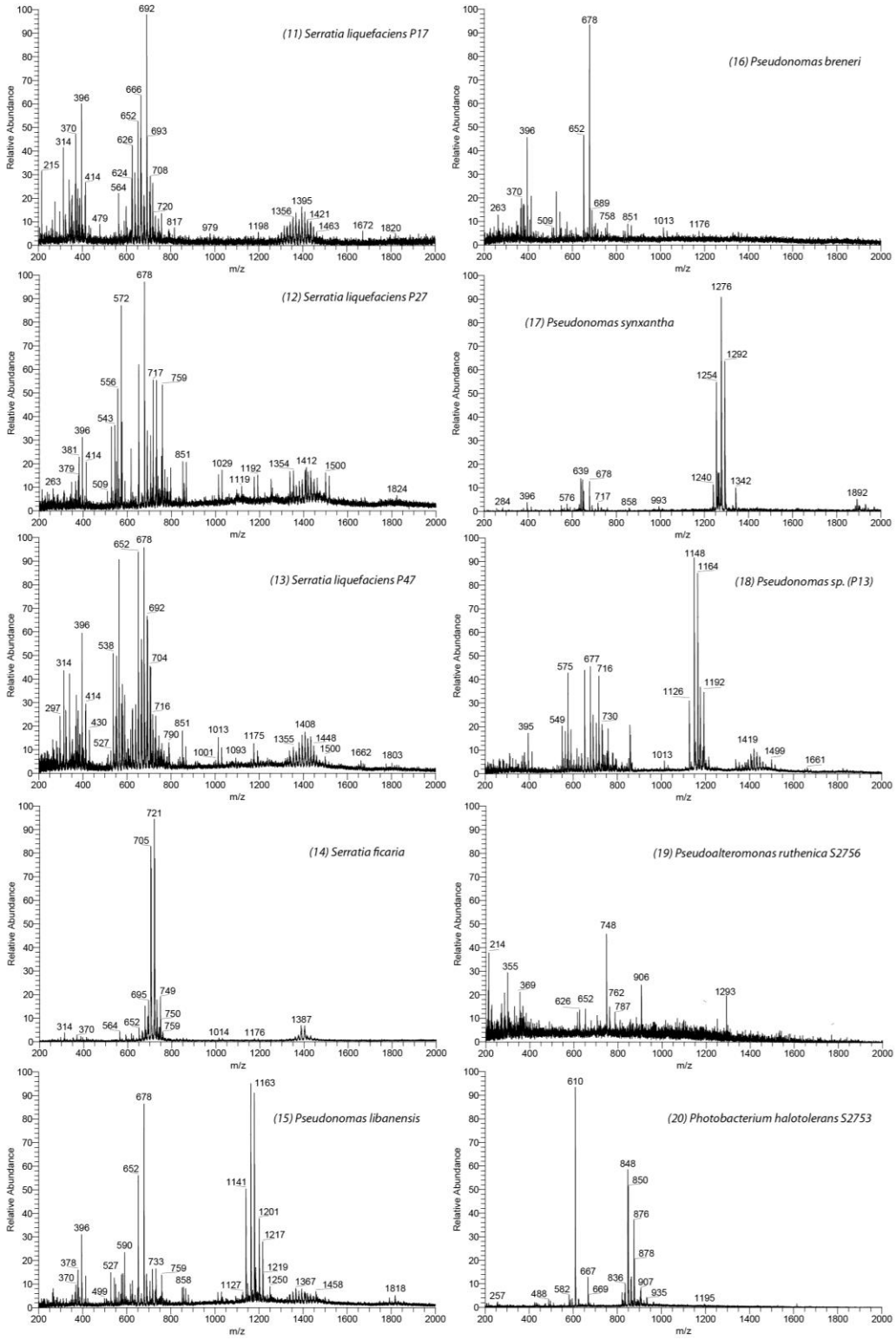

Figure 3.15 Real-time mass spectra acquired on the surfaces of diverse microbial colonies 1-34. (*Continued*)

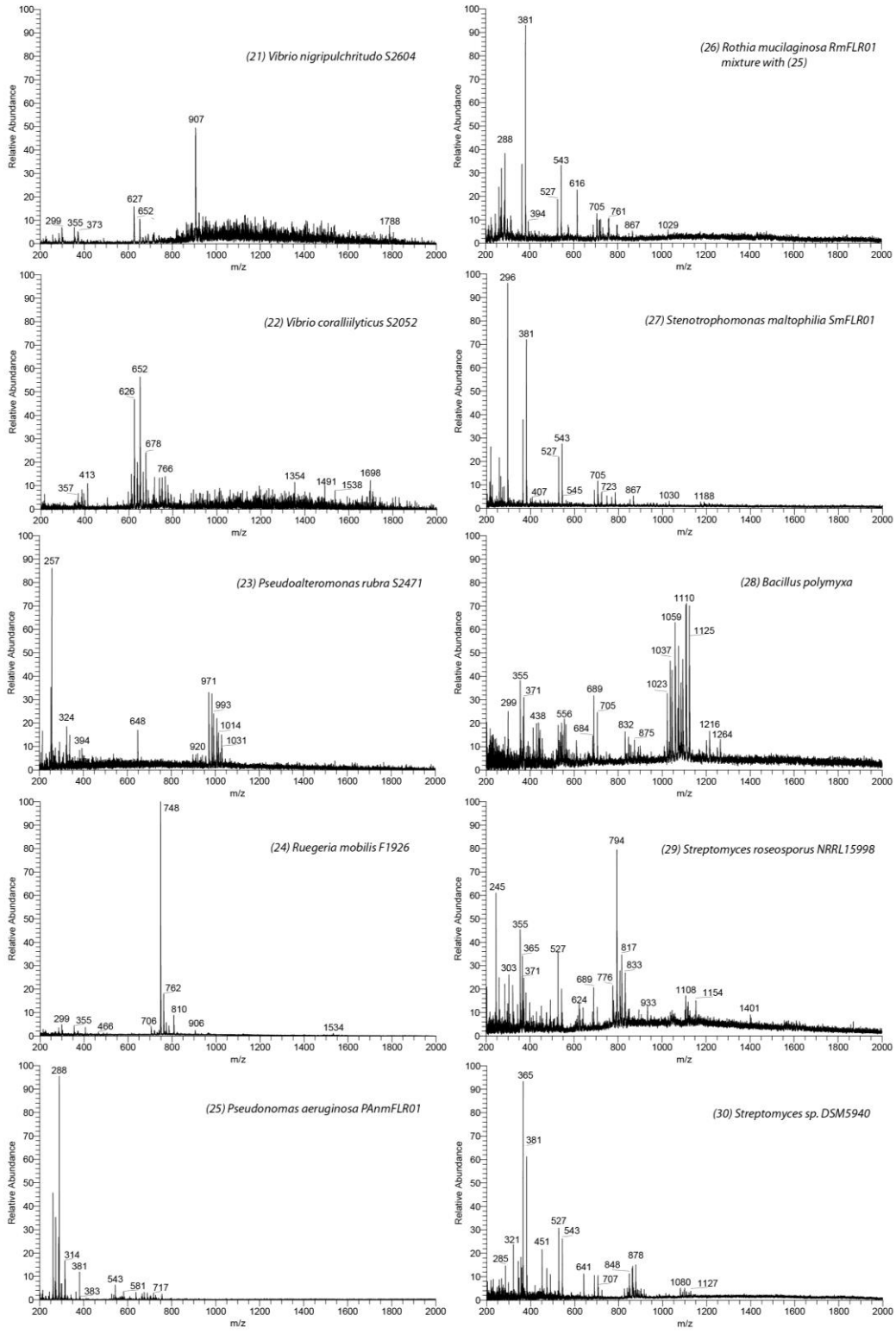

Figure 3.15 Real-time mass spectra acquired on the surfaces of diverse microbial colonies 1-34. (*Continued*)

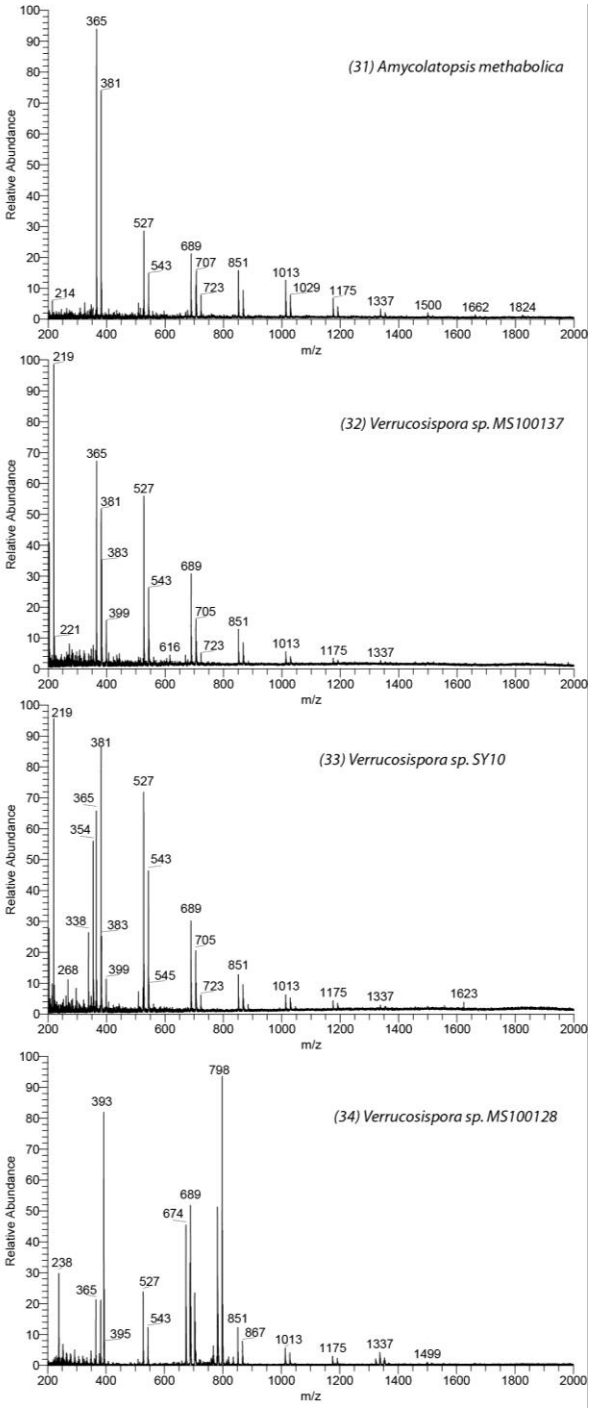

Figure 3.15 Real-time mass spectra acquired on the surfaces of diverse microbial colonies 1-34. (*Continued*)

3.8 References

(1) Phelan, V. V.; Liu, W.-T.; Pogliano, K.; Dorrestein, P. C. Microbial metabolic exchange: the chemotype-to-phenotype link. *Nat. Chem. Biol.* **2012**, *8*, 26–35.

(2) Rappe, M. S.; Giovannoni, S. J. The uncultured microbial majority. *Annu. Rev. Microbiol*. **2003**, *57*, 369–394.

(3) Schloss, P. D.; Handelsman, J. Status of the microbial census. *Microbiol. Mol. Biol. Rev*. **2004**, *68*, 686–691.

(4) Curtis, T. P.; W. T. Sloan; J. W. Scannell. Estimating prokaryotic diversity and its limits. *Proc. Natl. Acad. Sci. U.S.A.* **2002**, *99*, 10494–10499.

(5) Human Microbiome Project Consortium. Structure, function and diversity of the healthy human microbiome. *Nature* **2012**, *486*, 207–214.

(6) Sekirov, I.; Russell, S. L.; Antunes, L. C. M.; Finlay, B. B. Gut microbiota in health and disease. *Physiol. Rev.* **2010**, *90*, 859–904.

(7) Markle, J. G. M.; Frank, D. N.; Mortin-Toth, S.; Robertson, C. E.; Feazel, L. M.; Rolle-Kampczyk, U.; von Bergen, M.; McCoy, K. D.; Macpherson, A. J.; Danska, J. S. Sex differences in the gut microbiome drive hormone-dependent regulation of autoimmunity. *Science* **2013**, *339*, 1084–1088.

(8) Yang, Y.-L.; Xu, Y.; Straight, P.; Dorrestein, P. C. Translating metabolic exchange with imaging mass spectrometry. *Nat. Chem. Bio.* **2009**, *5*, 885–887.

(9) Liu, W.-T.; Yang, Y.-L.; Xu, Y.; Lamsa, A.; Haste, N. M.; Yang, J. Y.; Ng, J.; Gonzalez, D.; Ellermeier, C. D.; Straight, P. D.; Pevzner, P. A.; Pogliano, J.; Nizet, V.; Pogliano, K.; Dorrestein, P. C. Imaging mass spectrometry of intraspecies metabolic exchange revealed the cannibalistic factors of *Bacillus subtilis*. *Proc. Natl. Acad. Sci. U.S.A.* **2010**, *107*, 16286–16290.

(10) Moree, W.J.; Phelan, V.V.; Wu, C. H.; Bandeira, N.; Cornett, D. S.; Duggan, B. M.; Dorrestein, P. C. Interkingdom metabolic transformations captured by microbial imaging mass spectrometry. *Proc. Natl. Acad. Sci. U.S.A.* **2012**, *109*, 13811-13816.

(11) Watrous, J.; Roach, P.; Alexandrov, T.; Heath, B. S.; Yang, J. Y.; Kersten, R. D.; van der Voort, M.; Pogliano, K.; Gross, H.; Raaijmakers, J. M.; Moore, B. S.; Laskin, J.; Bandeira, N.; Dorrestein, P. C. Mass spectral molecular networking of living microbial colonies. *Proc. Natl. Acad. Sci. U.S.A.* **2012**, *109*, E1743–E752.

(12) Roach, P. J.; Laskin, J.; Laskin, A. Nanospray desorption electrospray ionization: an ambient method for liquid-extraction surface sampling in mass spectrometry. *Analyst*, **2010**, *135*, 2233–2236.

(13) ElNaggar, M. S.; Barbier, C.; Van Berkel, G. J. Liquid Microjunction surface sampling probe fluid dynamics: computational and experimental analysis of coaxial intercapillary positioning effects on sample manipulation. *J. Am. Soc. Mass Spectrom*. **2011** *22*, 1157–1166.

(14) Kertesz, V.; Van Berkel, G. J. Liquid microjunction surface sampling coupled with HPLC for analysis of drugs and metabolites in whole-body thin tissue sections. *Anal. Chem.* **2010**, *82*, 5917–5921.

(15) Van Berkel, G. J.; Sanchez, A. D.; Quirke, J. M. E. Thin-layer chromatography and electrospray mass spectrometry coupled using a surface sampling probe. *Anal. Chem*. **2002**, *74*, 6216–6223.

(16) Walworth, M. J.; ElNaggar, M. S.; Stankovich, J. J.; Witkowski, C.; Norris, J. L.; Van Berkel, G. J. Direct sampling and analysis from solid phase extraction cards using an automated liquid extraction surface analysis nanoelectrospray mass spectrometry system. *Rapid Commun. Mass Spectrom.* **2011**, *25*, 2389–2396.

(17) ElNaggar M. S.; Van Berkel, G. J. Liquid microjunction surface sampling probe fluid dynamics: characterization and application of an analyte plug formation operational mode *J. Am. Soc. Mass. Spectrom.* **2011**, *22*, 1737-1743.

(18) Vlamakis, H.; Chai, Y.; Beauregard, P.; Losick, R.; Kolter, R. Sticking together: building a biofilm the Bacillus subtilis way. *Nat. Rev. Microbiol.* **2013**, *11*, 157–168.

(19) Arima, K.; Kakinuma, A.; Tamura, G. Surfactin, a crystalline peptidelipid surfactant produced by Bacillus subtilis: isolation, characterization and its inhibition of fibrin clot formation. *Bioch. Biophys. Res. Comm.* **1968**, *31*, 488–494.

(20) Peypoux, F.; Bonmatin, J. M.; Wallach, J. Recent trends in the biochemistry of surfactin. *Appl. Microbiol. Biotechnol.* **1999**, *51*. 553–563.

(21) Zeigler, D. R.; Prágai, Z.; Rodriguez, S.; Chevreux, B.; Muffler, A.; Albert, T.; Bai, R.; Wyss, M.; Perkins, J. B. The origins of 168, W23, and other Bacillus subtilis legacy strains. *J. Bacteriol.* **2008**, 190, 6983–6995.

(22) Song, Y.; Talaty, N.; Datsenko, K.; Wanner, B. L.; Cooks, R. G. In vivo recognition of Bacillus subtilis by desorption electrospray ionization mass spectrometry (DESI-MS). *Analyst*, **2009**, *134*, 838–841.

(23) Watrous, J.; Hendricks, N.; Meehan, M.; Dorrestein, P. C. Capturing bacterial metabolic exchange using thin film desorption electrospray ionization-imaging mass spectrometry. *Anal. Chem*. **2010**, *82*, 1598–1600.

(24) Tsuge, K.; Matsui, K.; Itaya, M. Production of the non-ribosomal peptide plipastatin in Bacillus subtilis regulated by three relevant gene blocks assembled in a single movable DNA segment. *J. Biotechnol.* **2007**, *129*, 592–603.

(25) Rahme, L. G.; Stevens, E. J.; Wolfort, S. F.; Shao, J.; Tompkins, R. G.; Ausubel, F. M. Common virulence factors for bacterial pathogenicity in plants and animals. *Science* **1995**, *268*, 1899–1902.

(26) Conrad, D.; Haynes, M.; Salamon, P.; Rainey, P. B. Youle, M.; Rohwer, F. Cystic fibrosis therapy: a community ecology perspective. *Am. J. Respir. Cell Mol. Biol.* **2013**, 48, 150–156.

(27) Dietrich, L. E. P.; Price-Whelan, A.; Petersen, A.; Whiteley, M.; Newman, D. K. The phenazine pyocyanin is a terminal signalling factor in the quorum sensing network of *Pseudomonas aeruginosa*. *Mol. Microbiol.* **2006**, *61*, 1308–1321.

(28) Lau, G. W.; Hassett, D. J.; Ran, H. M.; Kong, F. S. The role of pyocyanin in Pseudomonas aeruginosa infection. *Trends Mol. Med.* **2004**, *10*, 599–606.

(29) Venturi, V. Regulation of quorum sensing in Pseudomonas. *FEMS Microbiol. Rev.* **2006**, *30*, 274–291.

(30) Heeb, S.; Fletcher, M. P.; Chhabra, S. R.; Diggle, S. P.; Williams, P.; Camara, M. Quinolones: from antibiotics to autoinducers. *FEMS Microbiol. Rev.* **2011**, *35*, 247–274.

(31) Soberón-Chávez, G.; Lépine, F.; Déziel, E. Production of rhamnolipids by Pseudomonas aeruginosa. *Appl. Microbiol. Biotechnol.* **2005**, *68*, 718–725.

(32) Watrous, J. D.; Phelan, V. V.; Hsu, C.-C.; Moree, W. J.; Duggan, B. M.; Alexandrov, T.; Dorrestein, P. C. Microbial metabolic exchange in 3D. *ISME J*. **2013**, *7*, 770–780.

(33) Hassan, H. M.; Fridovich, I. Mechanism of the antibiotic action pyocyanine. *J. Bacteriol*. **1980**, *141*, 156–163.

(34) Williamson, N. R.; Fineran, P. C.; Leeper, F. J.; Salmond, G. P. C. The biosynthesis and regulation of bacterial prodiginines. *Nat. Rev. Microbiol.* **2006**, *4*, 887–899.

(35) González-Pastor, J. E.; Hobbs, E. C.; Losick, R. Cannibalism by sporulating bacteria. *Science* **2003**, *301*, 510–513.

(36) Ellermeier, C. D.; Hobbs, E. C.; González-Pastor, J. E.; Losick, R. A three-protein signaling pathway governing immunity to a bacterial cannibalism toxin. *Cell* **2006**, *124*, 549–559.

(37) Pikula, J.; Bandouchova1, H.; Novotný, L.; Meteyer, C. U.; Zukal, J.; Irwin, N. R.; Zima, J.; Martínková, N. Histopathology confirms white-nose syndrome in bats in Europe. *J. Wildl. Dis.* **2012**, *48*, 207–211.

(38) Button, J. E.; Dutton, R. J. Cheese microbes. *Curr. Bio*. **2012**, *22*, R587–589.

(39) Gram, L.; Melchiorsen, J.; Bruhn, J. B. Antibacterial activity of marine culturable bacteria collected from a global sampling of ocean surface waters and surface swabs of marine organisms. *Mar. Biotechnol*. **2010**, *12*, 439-451.

(40) Wang, Q.; Song F, Xiao X, Huang P, Li L, Monte A, Abdel-Mageed WM, Wang J, Guo H, He W, Xie F, Dai H, Liu M, Chen C, Xu H, Liu M, Piggott AM, Liu X, Capon RJ, Zhang L. Abyssomicins from the South China Sea deep-sea sediment Verrucosispora sp.: natural thioether Michael addition adducts as antitubercular prodrugs. *Angew. Chem. Int. Ed*. **2012**, *51*, 1–5.

(41) Nielsen, A.; Månsson, M.; Wietz, M. Varming, A. N.; Phipps, R. K.; Larsen, T. O.; Gram, L.; Ingmer, H. Nigribactin, a novel siderophore from *vibrio nigripulchritudo*, modulates *staphylococcus aureus* virulence gene expression. *Mar. Drugs* **2012**, *10*, 2584–2595.

(42) Zhang, J. I.; Talaty, N.; Costa, A. B.; Xia, Y.; Tao, W. A.; Bell, R.; Callahan, J. H.; Cooks, R. G. Rapid direct lipid profiling of bacteria using desorption electrospray ionization mass spectrometry. *Int. J. Mass Spectrom.* **2011**, *301*, 37–44.

(43) Song, Y.; Talaty, N.; Tao, W. A.; Pan, Z.; Cooks, R. G. Rapid ambient mass spectrometic profiling of intact, untreated bacteria using desorption electrospray ionization. *Chem. Commun.* **2007**, 61–63.

(44) Dubois, D.; Leyssene, D.; Chacornac, J. P.; Kostrzewa, M.; Schmit, P. O.; Talon, R.; Bonnet, R.; Delmas, J. Identification of a variety of Staphylococcus species by matrix-assisted laser desorption ionization-time of flight mass spectrometry. *J. Clin. Microbiol.* **2010**, *48*, 941–945.

(45) Benagli, C.; Rossi, V.; Dolina, M.; Tonolla, M.; Petrini, O. Matrix-assisted laser desorption ionization-time of flight mass spectrometry for the identification of clinically relevant bacteria. *Plos One* **2011**, *6*. e16424.

(46) Weinmann, W.; Wiedemann, A.; Eppinger, B.; Renz, M.; Svoboda, M. Screening for drugs in serum by electrospray ionization/collision-induced dissociation and library searching. *J. Am. Soc. Mass Spectrom.* **1999**, *10*, 1028–1037.

(47) Campbell, J. M.; Collings, B. A.; Douglas, D. J. A new linear ion trap time-of-flight system with tandem mass spectrometry capabilities. *Rapid Commun. Mass Spectrom.* **1998**, *12*, 1463–1474.

(48) Schneider, B. S.; Douglas, D. J.; Chan, D. D. Y. Ion fragmentation in an electrospray ionization mass spectrometer interface with different gases. *Rapid Commun. Mass Spectrom.* **2001**, *15*, 249–257.

(49) Rath, C. M.; Alexandrov, T.; Higginbottom, S. K.; Song, J.; Milla, M. E.; Fischbach, M. A.; Sonnenburg, J. L.; Dorrestein, P. C. Molecular analysis of model gut microbiotas by imaging mass spectrometry and nanodesorption electrospray ionization reveals dietary metabolite transformations. *Anal. Chem*. **2012**, *84*, 9259-9267.

(50) Youngman, P.; Perkins, J.; Losick, R. Construction of a cloning site near one end of Tn917 into which foreign DNA may be inserted without affecting transposition in Bacillus subtilis or expression of the transposon-borne erm gene. *Plasmid* **1984**, *12*, 1–9.

(51) Chatterjee, S.; Nadkarni, S. R.; Vijayakumar, E. K. S.; Patel, M. V.; Ganguli; B. N. J. Napsamycins, new Pseudomonas active antibiotics of the mureidomycin family from Streptomyces sp. HIL Y-82,11372. *Antibiot*. **1994**, *47*, 595–598.

Chapter 3 is a full reprint of the material as it appears in the published article of Analytical Chemistry 2013, vol. 85, pp.7014-7018 by Cheng-Chih Hsu, Mariam S. ElNaggar, Yao Peng, Jinshu Fang, Laura M. Sanchez, Samantha J. Mascuch, Kirsten A. Møller, Emad K. Alazzeh, Jiri Pikula, Robert A. Quinn, Yi Zeng, Benjamin E. Wolfe, Rachel J. Dutton, Lena Gerwick, Lixin Zhang, Xueting Liu, Maria Månsson, and Pieter C. Dorrestein. The thesis author was the primary author and investigator.

Chapter 4

Direct Profiling of Microbial-host Interaction using Microscopy Ambient Mass Spectrometry: White-nose Syndrome Bats

4.1 Abstract

In Chapter 2 and 3, mass spectrometry analysis using ambient ionization is used to study mammalian embryonic development and microbial natural metabolites. This chapter we extend the study to the interaction between host-microbial interactions. The first case studied is bats with white-nose syndrome (WNS). WNS caused by the pathogenic fungus *Pseudogymnoascus destructans* is decimating populations of several hibernating North American bat species. Little is known about the molecular interplay between pathogen and host in this disease. Fluorescence microscopy ambient ionization mass spectrometry was used to generate metabolic profiles from the wings of both healthy and diseased bats in the genus *Myotis*. The fungal siderophores, molecules that are used to scavenge iron from their surroundings, were detected on the wings of bats with WNS, but not on healthy bats. This work is among the first examples in which microbial molecules are directly detected from an infected host and highlights the ability

of atmospheric ionization methodologies to provide direct molecular insight into infection.

4.2 Introduction

Fungal diseases of animals and plants have long been a feature of natural ecosystems, but evidence suggests that incidences of mycoses are increasing in frequency and severity and that these emerging infectious diseases pose a threat in terms of loss of biodiversity and food security.[1] Fungal infections, in particular, have garnered a large amount of attention recently due to their detrimental impacts on populations of organisms as varied as sea fans, turtles, bees, corals, frogs, crayfish, and bats.[1-7] The fungal infection affecting hibernating North American bats, white-nose syndrome (WNS), is one example of such a devastating fungal outbreak.[8,9] Since it was first described in New York in 2006, WNS has spread to 20 states and has killed about 6 million bats.[10-11] The fungus identified as the causative agent of WNS, *Pseudogymnoascus destructans*, is believed to be an exotic organism of European origin that was introduced to the U.S.[10-18]

The mechanism through which WNS induces mortality remains to be fully elucidated.[19-27] It is hypothesized that cutaneous infection of bat wing skin with *P. destructans* disrupts electrolyte balance.[19-20] This imbalance or some other mechanism causes increases in the frequency at which infected bats arouse from torpor during winter.[20] Frequent arousals may in turn deplete fat stores and lead to death by starvation.[20] Identifying the molecules that fungal pathogens use to interact with a host provides insight into the mechanism of their pathogenicity. Better understanding these mechanisms may lead to improved management strategies that account for the biology of

the pathogen. We therefore set out to determine if we could detect any fungal metabolites and define the metabolic milieu directly from the wings of diseased bats. We used fluorescent microscopy guided ambient mass spectrometry to metabolically profile the wings of bats of the genus *Myotis* that were healthy (n = 5) or showed signs of WNS infection (n = 11).

4.3 Methods and Materials

4.3.1 Animal Collection & Tissue Sample Preparation

Five healthy *Myotis lucifugus*, 10 M. *lucifugus* with WNS, and one *Myotis septentrionalis* with WNS were included in the analysis. All bats were found deceased during routine monitoring of maternity or hibernation roosts being conducted by state agency biologists. In Pennsylvania, personnel of the Pennsylvania Game Commission collected the specimens in compliance with Pennsylvania Statute Title 34, Section 322. Deceased bats collected in West Virginia were collected by personnel of the West Virginia Department of Natural Resources and no permits were required. All but one of these bats were collected prior to the emergence of WNS in North America. The remaining bat had no obvious signs of *P. destructans* infection (e.g. cupping erosions) when evaluated microscopically. WNS bats were collected in 2011 in Pennsylvania and in West Virginia during a WNS-associated mass mortality event. No bats were euthanized for this study. Two 6 mm tissue punches were collected from the wings of each of the deceased bats, affixed to 1x3 inch microscope glass slides, and stored at -80 ^{o}C prior to mass spectrometric analysis.

4.3.2 Microscopy Ambient Ionization Mass Spectrometry of Bat Wings

The mass spectrometric interrogation of bat wing skin was performed using a hybrid microcroscopy/ionization technique which combines an ambient nanospray desorption electrospray ionization (nanoDESI) source and an inverted microscope as described.[28] The only addition from the prior usage of this tool was the analysis with fluorescence. This allowed us to illuminate the wings with UV light and visualize areas of fluorescence that correlate with the development of cupping erosions due to infection with *P. destructans* (Figure 4.1).[29] We could then directly target these areas with the nanoDESI probe for MS analysis (Figure 4.1). The sample slide with wing punches was placed on the stage of a Nikon DIAPHOT 300 microscope and bright field and fluorescent images of the tissue were captured using a CCD camera (Nikon D40 DSLR) to confirm the presence or absence of fungal infection. The stage was then manipulated to move the tissue sample to the desired position under the micrometer-sized liquid junction formed by the two flame-pulled fused silica capillaries of the nanoDESI. The capillary tubes were flamed-pulled from original 150/50 μm (O.D./I.D.) to ~60 μm O.D. and a voltage of 2.2 kV was applied to them throughout the experiment. The capillaries were aligned in a "V" configuration so that they abutted one another at the bottom of the "V" and then angled 45° away from the point of contact in either direction. A syringe pump was used to continuously deliver the solvent (either acetonitrile in water (65/35, vol/vol) with 0.2 % formic acid, methanol in water (50/50, vol/vol) with 0.2 % formic acid, or methanol, acetonitrile, and toluene (50/35/15, vol/vol/vol) with 0.2 % formic acid) at a rate of ~1.0 μL/min through 300/100 μm (O.D./I.D.) fused silica capillary tubing to the primary flame-pulled capillary. This solvent was then aspirated by the secondary

capillary resulting in the formation of a dynamic liquid droplet of approximately 100 μm in diameter at the junction of the two capillaries. The sample stage was raised until the tissue contacted the liquid droplet and a continuous stream of solvent containing analytes desorbed from the tissue was delivered to the inlet of the mass spectrometer (hybrid 6.4-T LTQ-FT; Thermo Electron, North America) via electrospray ionization generated at the terminal end of the secondary capillary. Multiple spots were sampled along each tissue slide.

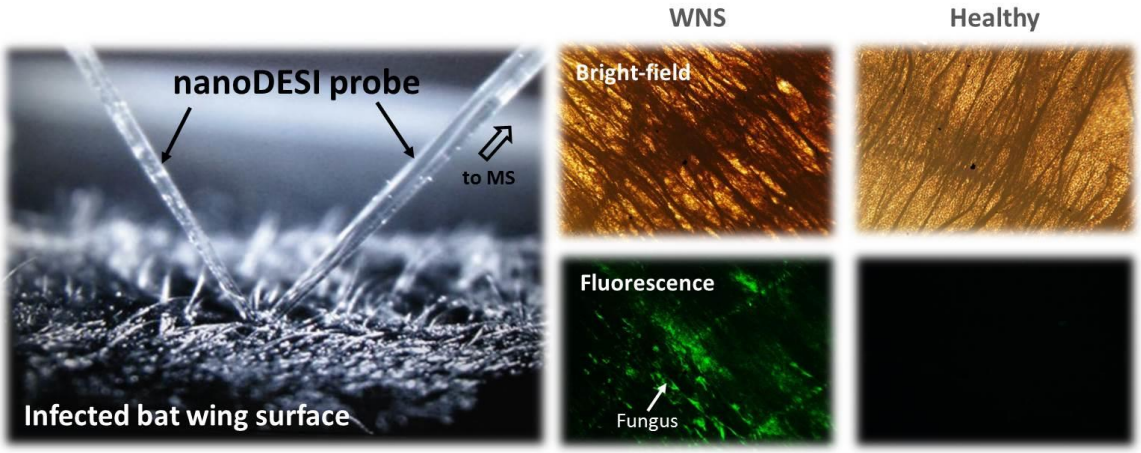

Figure 4.1 Fluorescence microscopy ambient ionization mass spectrometry of the bat wings. Tissue samples from the wings of healthy bats and individuals with white-nose syndrome were subjected to microscopy ambient ionization mass spectrometry. *Pseudogymnoascus destructans* infection was confirmed by the presence of fluorescent lesions when the tissue was excited with UV light (right and middle). Left: A nanoDESI source was used to desorb analytes from fluorescent tissue regions for MS analysis (capillary junction making contact with the tissue surface).

4.3.3 Molecular Networking

The structural relationships between different masses in MS^1 scans (precursor ions) were mapped in Cytoscape based on the similarity of their tandem MS fragmentation patterns as assessed through molecular networking using the web-based Global Natural Products Social Molecular Networking tool (GnPS, publicly online server

at http://gnps.ucsd.edu/).[30-32] A cosine cutoff of 0.6 was selected for generation of the network. Background signals arising from solvents or agar were subtracted during the network processing stage. The network was then imported into Cytoscape for visualization. Precursor ions were represented by nodes and the similarity between two precursor ions as determined by comparison of their fragments/cosine score was represented as an edge between two nodes. The magnitude of the cosine score was represented by edge thickness with pairs of compounds with high scores having thicker lines. A search of the publicly curated GNPS standards library was also performed to determine if any of the masses represented in the network matched to known compounds that we had not considered in our analysis. All data files used in the generation of the network were deposited in the GNPS massIVE data repository and are publicly available (MassIVE ID MSV000078620).

Iron-free ferrichrome (Santa Cruz Biotechnology), ferrichrome (Iron-free ferrichrome with the addition of iron (III) chloride hexahydrate), and triacetylfusarinine C (EMC microcollections GmbH) were used as standards to verify the molecular assignment of the siderophores in the tissue samples through a process known as dereplication.[32] The solubilized standards were introduced directly into the MS inlet with a Triversa nanomate-electrospray ionization source and analyzed using the data-dependent method described above. A molecular network was then generated using the data files from the standards, fungal extracts, and tissue samples. The nodes correlated with the standard data files were examined to establish if they clustered with experimental nodes or were incorporated into consensus nodes that also included experimental files. Following this neighborhood analysis, the spectra were manually

examined and the fragmentation of the raw spectra evaluated for similarity. Through this analysis it was possible to definitively determine whether or not desferrichrome, ferrichrome and triacetylfusarinine C were detected from the wing surfaces and/or from fungal cultures.

4.3.4 Fungal Extraction for MS Analysis

Replicates of *P. destructans* were grown on ISP2 agar plates (4 g/liter yeast extract, 10 g/liter malt extract, 4 g/liter dextrose, and 1.5 to 2% agar). Small plugs of agar and fungal biomass were collected and combined with 100 µl of *n*-butanol in microcentrifuge tubes. Extractions were allowed to proceed at room temperature for one hour. The organic layers were centrifuged and the supernatant was subsequently analyzed. A Triversa nanomate-electrospray ionization source was used to introduce the extracts (diluted in methanol in water (50:50) with 1% formic acid) directly into the MS inlet. This was accomplished using a spray voltage setting of 1.3-1.45 kV and a pressure of 0.35-0.5 psi as set with Chipsoft software version 7.2.0. Data were collected using Xcalibur software version 1.4 SR1 running the data-dependent method described below.

4.4 Results and Discussions

Microscopy ambient mass spectrometry of wings from infected, healthy bats as well as mass spectrometry of extracts from *P. descructans* grown on agar resulted in the generation of a large number of MS/MS spectra. The MS/MS spectra were subjected to molecular networking of samples resulting in a network comprised of 1,503 nodes representing precursor ions derived from intact chemical compounds and 2,463 edges

(Figures 4.2 & 4.3). Each node is then colored with respect to healthy wings, WNS wings, *P. destructans* colony and standards. The resulting molecular network provides a visual picture of the diversity and the origin of MS/MS spectra that were collected.

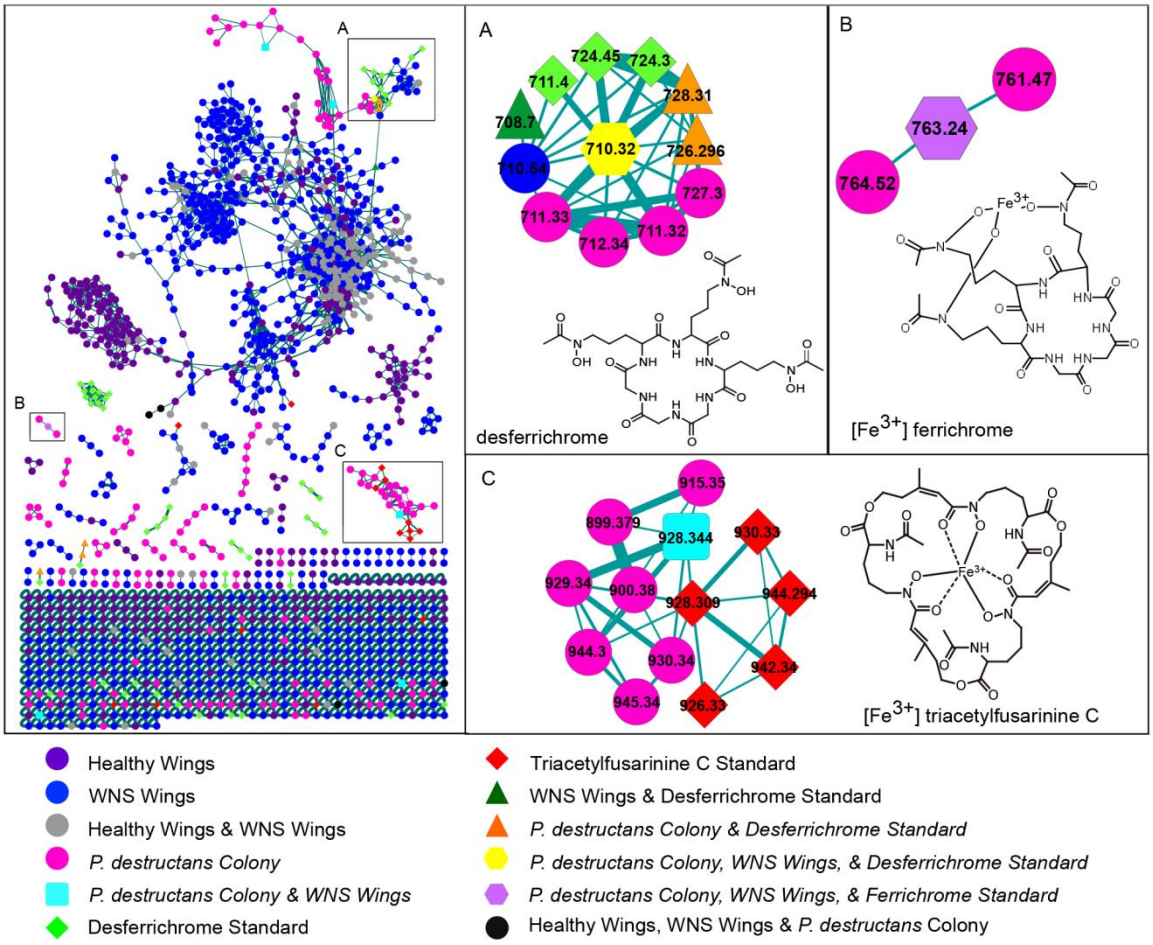

Figure 4.2 Detection of siderophores on the wings of bats with white-nose syndrome via molecular networking. Molecular networking of the MS/MS data was used to determine the structural relationships between the metabolites detected from wing surfaces, cultured *Pseudogymnoascus destructans*, and commercial siderophore standards. The siderophores desferrichrome and ferrichrome were observed from the wings of bats with white-nose syndrome and from cultured *P. destructans* and formed consensus nodes with commercial standards (A,B). Triacetylfusarinine C was also present on WNS wings and in the *P. destructans* colony (C). None of the three siderophores were detected on the wings of healthy bats.

The molecular network in Figure 4.2 highlights a large number of molecules that are present on the wings of WNS bats and not detected on the healthy ones. At this point it is not clear if most represent fungal metabolites that are produced on the wings or if they represent the host response. Likely it is a combination of both fungal metabolites and host metabolites and dissapearence of metabolites that contribute to infection. Based on matches to MS/MS spectra of known fungal metabolites, a family of fungus-derived iron scavenger molecules were largely expressed and inspected in further detail.

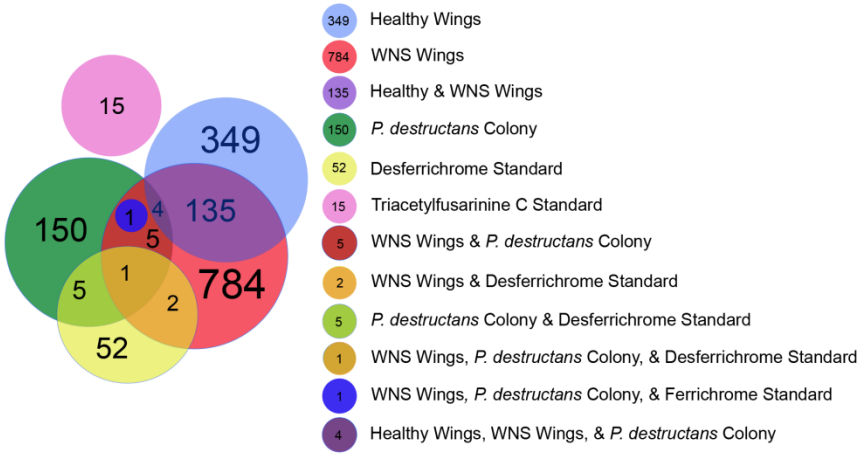

Figure 4.3 Molecular networking entity compositional analysis. The molecular network was composed of nodes that incorporated MS/MS scans from only a single sample type as well as consensus nodes that incorporated spectra from different experimental sample types. The number of nodes of each category and their relationships to each other are conveyed in a Venn diagram.

The node, as labeled in Figure 5.2A with *m/z* 710.32, combined scans from a WNS wing, the *P. destructans* colony, and the desferrichrome standard; scans from the wings of healthy bats are not a part of this node. Manual inspection of the MS/MS fragmentation data for these precursors confirmed that the pattern observed from the WNS wing and the fungal colony matched that of the commercial desferrichrome standard (Figure 4.4). The signal for the siderophore was analyzed in a targeted fashion,

by performing MS/MS directly on the parent ion during microscopy nanoDESI analysis, and detected desferrichrome in 10 of the 11 WNS bats and was virtually undetectable in all the wing samples from healthy bats (Figure 4.5).

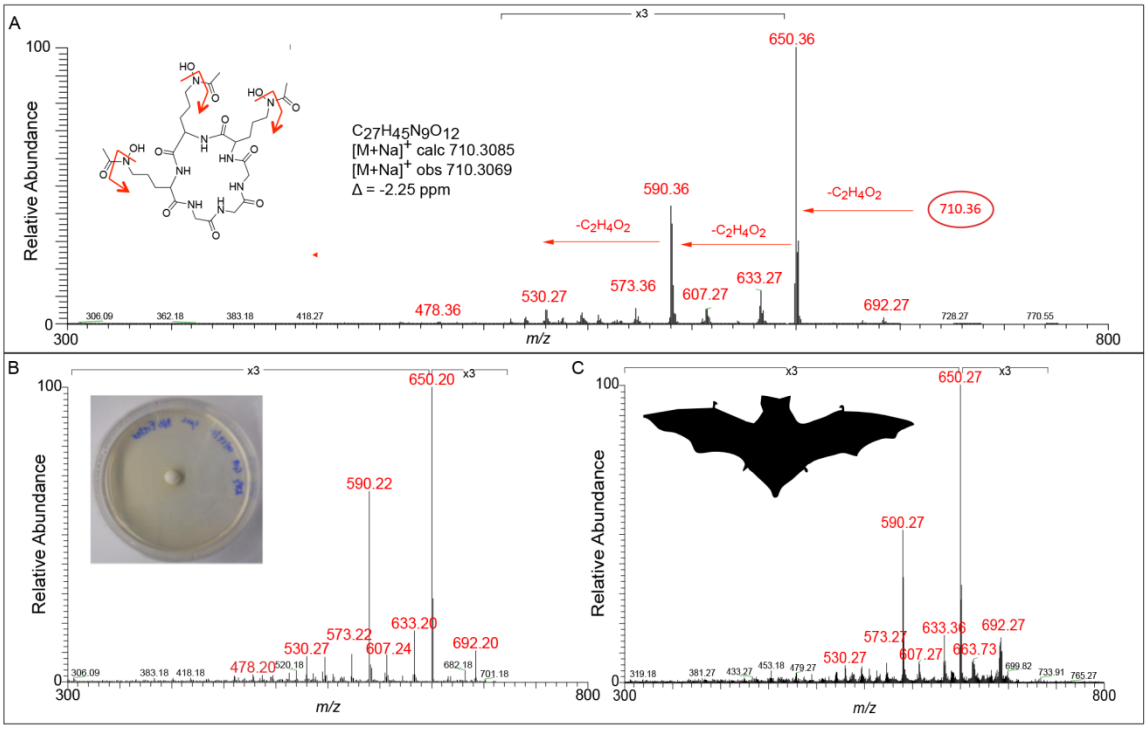

Figure 4.4 Comparison of desferrichrome fragmentation among standards and samples. (A) MS/MS of the desferrichrome standard. The MS/MS fragmentation patterns from the *P. destructans* colony (B) and WNS wing (C) matched the fragmentation of the standard precursor.

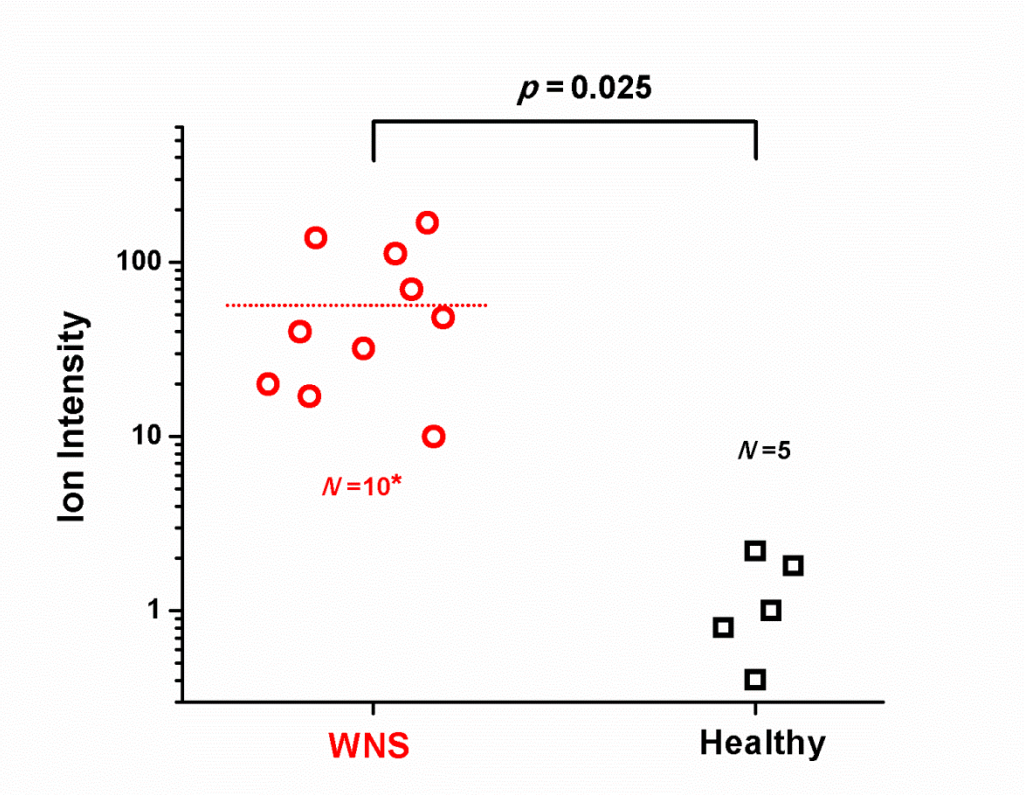

Figure 4.5 Statistical analysis of desferrichrome daughter ion intensity among healthy and diseased bat wings. Analysis of variance (ANOVA) of the absolute intensities of the desferrichrome daughter ion, *m/z* 650 (neutral loss of $C_2H_4O_2$), observed on WNS and healthy bat wings (see Figure 4.6). A ± 3 *m/z* ion window was allowed when selecting the precursor, *m/z* 710. Differences in the absolute intensities of the daughter ions among 10 of the 11 WNS wings and 5 healthy wings were statistically significant (p = 0.025). On the eleventh WNS wing, no ions within the *m/z* 710 ± 3 *m/z* range was selected for fragmentation by the automatic data-dependent method due to low ion intensity and the sample could therefore not be included in the plot.

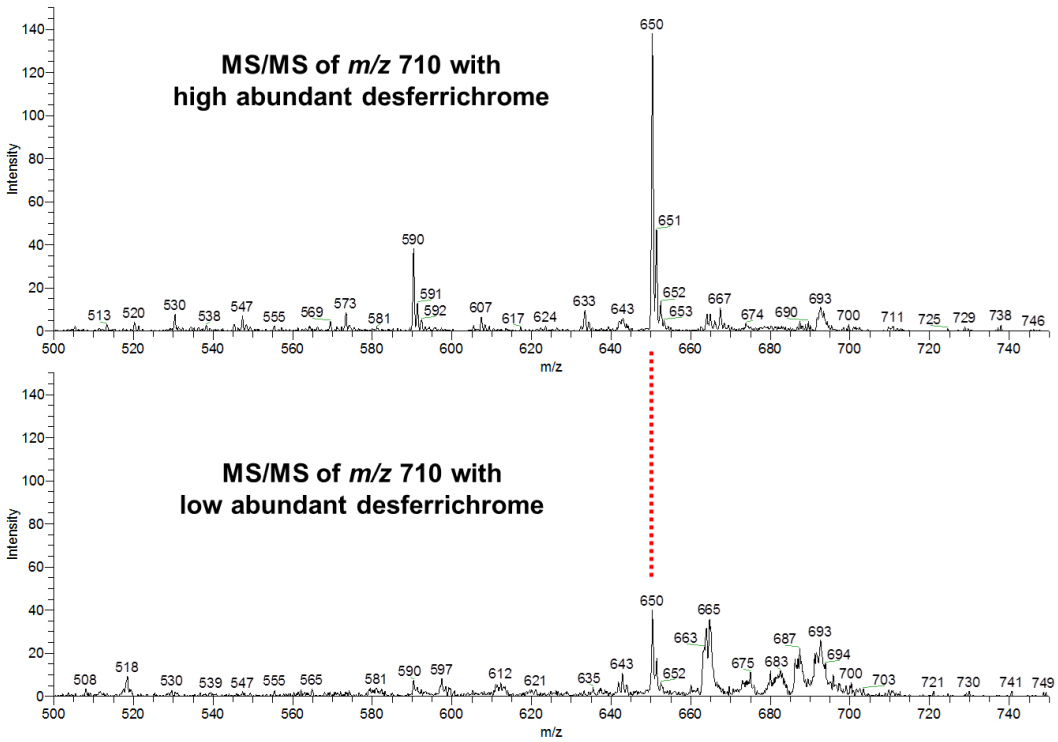

Figure 4.6 Variation in the intensity of desferrichrome daughter ion *m/z* 650 detected from white-nose syndrome wing samples. In cases where desferrichrome precursor ions display high intensities relative to other metabolites, their fragmentation patterns will be less complicated and they will have a greater cosine correlation with the standard (A). When the intensities of the desferrichrome ions are less intense, background noise or peaks from other compounds of similar mass may be fragmented along with it resulting in more complicated MS/MS spectra and a lower cosine correlation with the standard even though the molecule is present (B).

Not only was the desferrichrome found but the iron chelated form (*m/z* 763.230). This indicates that on the bats of wings there is sufficient iron present to be chelated by the siderophore (Figures 4.2 & Figure 4.7 for MS/MS validation). Suprisingly not only one fungal siderophore was detected but also the triacylfuseranine was detected (Figure 4.2, *m/z* 928.340). Manual inspection of the tandem mass spectra showed that all of these nodes derived from the fragmentation of triacetylfusarinine C (Figure 4.8).

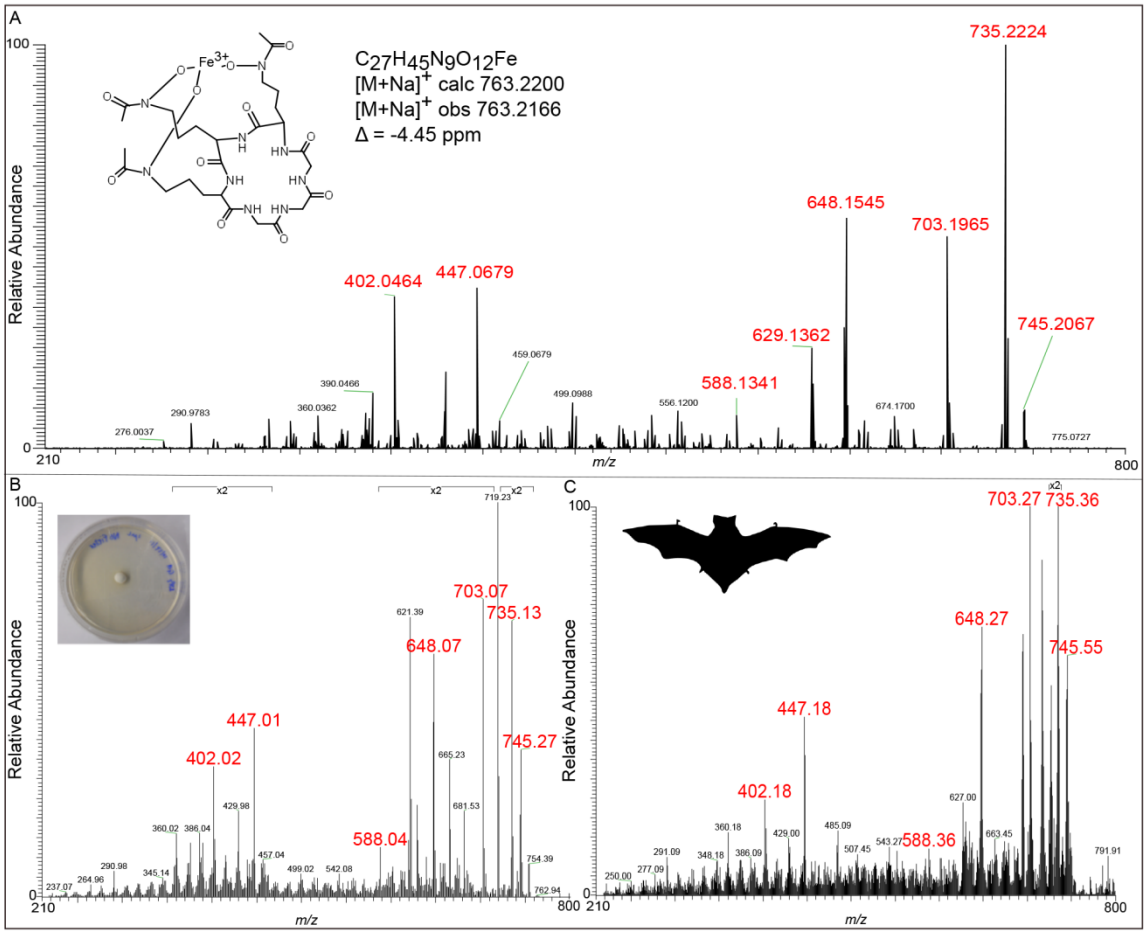

Figure 4.7 Comparison of ferrichrome fragmentation among standards and samples. (A) MS/MS of ferrichrome $Fe3^{+}$ complex standard *m/z* 763. MS/MS fragmentation patterns for *m/z* 763 from the *P. destructans* colony (B) and WNS wings (C) matched the fragmentation of the standard precursor.

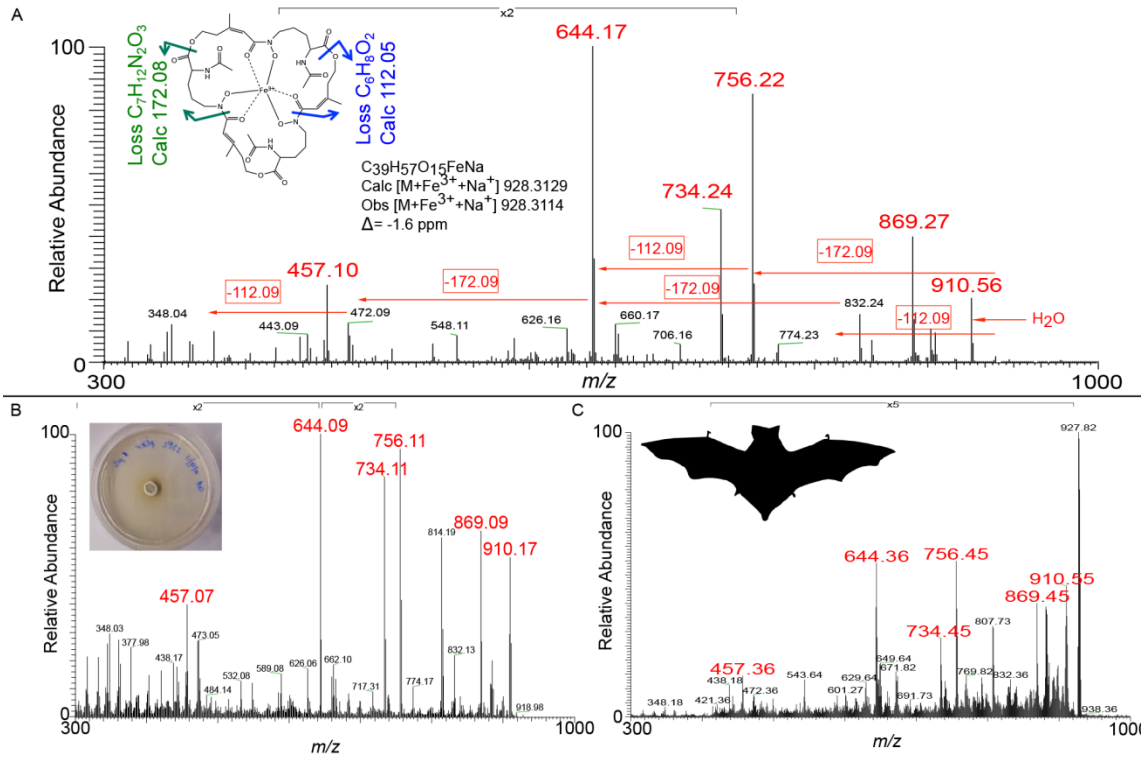

Figure 4.8 Comparison of triacetylfusarinine C fragmentation among standards and samples. (A) MS/MS of triacetylfusarinine C Fe^{3+} complex standard *m/z* 928. The MS/MS fragmentation patterns for *m/z* 928 from the *P. destructans* colony (B) and WNS wings (C) matched the fragmentation of the standard precursor.

Genomic analysis and imaging mass spectrometry further revealed that *P.destructans* makes both siderophores (data not shown due to copyright issues). Without infecting healthy bats with WNS and sacrificing them, one cannot confirm if these fungal metabolites are coming from *P.destructans.* It is our interpretation and hypothesis based on these results that *P. destructans* is in need for iron for its infection and thereby producing these siderophores during its colonization of bats. However, the results nicely demonstrate that microscopy-based mass spectrometry can be used to detect microbial derived metabolites on the skin surface.

Iron plays an important role in infections. In the vertebrate host iron is tightly bound by proteins including ferriportin, lactoferrin, ferritin, and transferrin.[33] Upon inflammation, macrophages sequester iron even further.[33,34] In general, the amount of iron available to invading microbes is sub-optimal for growth given host defenses.[33,35] Fungi such as *Aspergilli*, *C. Albicans*, *Microsporum* and *Trichophyton*, have been demonstrated to use siderophores to compete with the host for iron through secretion of siderophores. Our detection of fungal siderophores on wings of WNS bats and not healthy ones suggest that iron competition might play a key role in WNS infections as well. Because iron is critical in microbial, including fungal infections, a number of antifungal strategies that target siderophores have recently emerged. These include efforts that link antifungals to siderophores to mediate their uptake, inundation with irrelevant siderophores that the organism cannot use or analogues that cannot bind iron, addition of iron chelators such as EDTA, and disruption of endogenous siderophore pathways through the blocking of biosynthetic enzymes or transporters.[36-38] In addition to increasing iron in the diets of the bats, an iron competition strategy should be assessed as possible WNS management methods in addition to other emerging strategies such as bacterial biocontrol.[39]

4.5 Conclusion

Here we used fluorescence microscopy ambient mass spectrometry in combination with molecular networking to detect microbial metabolites directly from the skin of WNS infected bats. The approach highlighted that fungal siderophores and other microbial molecules are present on the WNS infected bats. Siderophores are a common

strategy for competition for iron with hosts and may represent an avenue for coming up with strategies for WNS management.

4.6 References

(1) Fisher, M.C.; Henk, D. A.; Briggs, C. J.; Brownstein, J. S.; Madoff, L. C.; Gurr, S. J. Emerging fungal threats to animal, plant and ecosystem health. *Nature* **2012**, *484*, 186-194.

(2) Kim, K.; Harvell, C. D. The rise and fall of a six-year coral-fungal epizootic. *Am. Nat.* **2004**, *164*, S52-S63.

(3) Sarmiento-Ramirez. J. M.; Abella, E.; Martin, M. P.; Telleria, M. T.; Lopez-Jurado, L. F.; Marco, A.; Diéguez-Uribeondo, J. *Fusarium solani* is responsible for mass mortalities in nests of loggerhead sea turtle, *Caretta caretta*, in Boavista, Cape Verde. *FEMS Microbiol. Lett.* **2010**, *312*, 192-200.

(4) Cameron, S. A.; Lozier, J. D.; Strange, J. P.; Koch, J. B.; Cordes, N.; Solterd, L. F.; Griswoldb, T. L. Patterns of widespread decline in North American bumble bees. *Proc. Natl. Acad. Sci. USA* **2011**, *108*, 662-667.

(5) Harvell, C. D.; Kim, K.; Burkholder, J. M.; Colwell, R. R.; Epstein, P. R.; Grimes, D. J.; Hofmann, E. E.; Lipp, E. K.; Osterhaus, A. D.; Overstreet, R. M.; Porter, J. W.; Smith, G. W.; Vasta, G. R. Emerging marine diseases - Climate links and anthropogenic factors. *Science* **1999**, *285*, 1505-1510.

(6) Holdich, D. M.; Reynolds, J. D.; Souty-Grosset, C.; Sibley, P. J. A review of the ever increasing threat to European crayfish from non-indigenous crayfish species. *Knowl. Manag. Aquat. Ec.* **2009**, *11*, 394-395.

(7) Blehert, D. S.; Hicks, A. C.; Behr, M.; Meteyer, C. U.; Berlowski-Zier, B. M.; Buckles, E. L.; Coleman, J. T. H.; Darling, S. R.; Gargas, A.; Niver, R.; Okoniewski, J. C.; Rudd, R. J.; Stone. W. B. Bat White-Nose Syndrome: An Emerging Fungal Pathogen? *Science* **2009**, *323*, 227-227.

(8) Frick, W. F.; Pollock, J. F.; Hicks, A. C.; Langwig, K. E.; Reynolds, D. S.; Turner, G. G.; Butchkoski, C. M.; Kunz1, T. H.;. An emerging disease causes regional population collapse of a common north american bat species. *Science* **2010**, *329*, 679-682.

(9) Langwig, K. E.; Frick, W. F.; Bried, J. T.; Hicks, A. C.; Kunz, T. H.; Kilpatrick, A. M. Sociality, density-dependence and microclimates determine the persistence of populations suffering from a novel fungal disease, white-nose syndrome. *Ecology Letters* **2012**, *15*, 1050-1057.

(10) *Whitenosesyndrome.org* **2014**, News Release: Where is it now? Available: http://www.whitenosesyndrome.org/about/where-is-it-now Accessed 15 April 2014

(11) *United States Fish and Wildlife Service* **2012**, News Release: North American bat death toll exceeds 5.5 million from white-nose syndrome. Available: http://www.fws.gov/northeast/feature_archive/Feature.cfm?id=794592078.

(12) Gargas, A.; Trest, M. T.; Christensen, M.; Volk, T. J.; Blehert, D. *Geomyces destructans* sp. nov., associated with Bat White-Nose Syndrome. *Mycotaxon* **2009**, *108*, 147-154.

(13) Minnis, A. M.; Lindner, D. L. Phylogenetic evaluation of *Geomyces* and allies reveals no close relatives of *Pseudogymnoascus destructans*, comb. nov., in bat hibernacula of eastern North America. *Fungal Biol.* **2013**, *117*, 638-649.

(14) Lorch, J. M.; Meteyer, C. U.; Behr, M. J.; Boyles, J. G.; Cryan, P. M.; Hicks, A. C.; Ballmann, A. E.; Coleman, J. T.; Redell, D. N.; Reeder, D. M.; Blehert, D. S. Experimental infection of bats with *Geomyces destructans* causes white-nose syndrome. *Nature* **2011**, *480*, 376-378.

(15) Puechmaille, S. J.; Frick, W. F.; Kunz, T. H.; Racey, P. A.; Voigt, C. C.; Wibbelt, G.; Teeling, E. C. White-nose syndrome: is this emerging disease a threat to European bats? *Trends. Ecol. Evol.* **2011**, *26*, 570-576.

(16) Puechmaille, S. J.; Wibbelt, G.; Korn, V.; Fuller, H.; Forget, F.; Mühldorfer, K.; Kurth, A.; Bogdanowicz, W.; Borel, C.; Bosch, T.; Cherezy, T.; Drebet, M.; Görföl, T.; Haarsma, A. J.; Herhaus, F.; Hallart, G.; Hammer, M.; Jungmann, C.; Le Bris, Y.; Lutsar, L.; Masing, M.; Mulkens, B.; Passior, K.; Starrach, M.; Wojtaszewski, A.; Zöphel, U.; Teeling, E. C. Pan-European distribution of white-nose syndrome fungus (*Geomyces destructans*) not associated with mass mortality. *PLoS ONE* **2011**, *6*, e19167.

(17) Warnecke, L.; Turner, J. M.; Bollinger, T. K.; Lorch, J. M.; Misra, V.; Cryanf, P. M.; Wibbeltg, G.; Blehertd, D. S.; Willis, C. K. R. Inoculation of bats with European *Geomyces destructans* supports the novel pathogen hypothesis for the origin of white-nose syndrome. *Proc. Natl. Acad. Sci. USA* **2012**, *109*, 6999-7003.

(18) Turner, G. G.; Reeder, D. M.; Coleman, J. T. H. A five-year assessment of mortality and geographic spread of white-nose syndrome in North American bats and a look to the future. *Bat Research News* **2011**, *52*, 13-27.

(19) Meteyer, C. U.; Buckles, E. L.; Blehert, D. S.; Hicks, A. C.; Green, D. E.; Shearn-Bochsler, V.; Thomas, N. J.; Gargas, A.; Behr M. J. Histopathologic criteria to confirm white-nose syndrome in bats. *J. Vet. Diagn. Inves.* **2009**, *21*, 411-414.

(20) Cryan, P. M.; Meteyer, C. U.; Blehert, D. S.; Lorch, J. M.; Reeder, D. M.; Turner, G. G.; Webb, J.; Behr, M.; Verant, M.; Russell, R. E.; Castle, K. T. Electrolyte depletion in white-nose syndrome bats. *J. Wildl. Dis.* **2013**, *49*, 398-402.

(21) Reeder, D. M.; Frank, C. L.; Turner, G. G.; Meteyer, C. U.; Kurta, A.; Britzke, E. R.; Vodzak, M. E.; Darling, S. R.; Stihler, C. W.; Hicks, A. C.; Jacob, R.; Grieneisen, L. E.; Brownlee, S. A.; Muller, L. K.;

(22) Meteyer, C. U.; Barber, D.; Mandl, J. N. Pathology in euthermic bats with white nose syndrome suggests a natural manifestation of immune reconstitution inflammatory syndrome. *Virulence* **2012**, *3*, 583-588.

(23) Maher, S. P.; Kramer, A. M.; Pulliam, J. T.; Zokan, M. A.; Bowden, S. E.; Barton, H. D.; Magori, K.; Drake, J. M. Spread of white-nose syndrome on a network regulated by geography and climate. *Nat. Comm.* **2012**, *3*, 1306.

(24) Raudabaugh, D. B.; Miller, A. N. Nutritional capability of and substrate suitability for *Pseudogymnoascus destructans*, the causal agent of bat white-nose syndrome. *PLoS ONE* **2013**, *8*, e78300.

(25) Moore, M. S.; Reichard, J. D.; Murtha, T. D.; Nabhan, M. L.; Pian, R. E.; Ferreira, J. S.; Kunz, T. H. Hibernating little brown Myotis (*Myotis lucifugus*) show variable immunological responses to white-nose syndrome. *PLoS ONE* **2013**, *8*, e58976.

(26) Moore, M. S.; Reichard, J. D.; Murtha, T. D.; Zahedi, B.; Fallier, R. M.; Kunz, T. H. Specific alterations in complement protein activity of little brown Myotis (*Myotis lucifugus*) hibernating in white-nose syndrome affected sites. *PLoS ONE* **2011**, *6*, e27430.

(27) de Groot, P. W. J.; Bader, O.; de Boer, A. D.; Weig, M.; Chauhan, N. Adhesins in human fungal pathogens: glue with plenty of stick. *Eukaryotic Cell* **2013**, *12*, 470-481.

(28) Hsu, C.-C.; White, N. M.; Hayashi, M.; Lin, E. C.; Poon. T.; Banerjee, I.; Chen, J.; Pfaff, S. L.; Macagno, E. R.; Dorrestein, P. C. Microscopy ambient ionization top-down mass spectrometry reveals developmental patterning. *Proc. Natl. Acad. Sci. USA* **2013**, *110*, 14855-14860.

(29) Turner, G. G.; Meteyer, C. U.; Barton, H.; Gumbs, J. F.; Reeder, D. M. Non-lethal screening of bat wing skin using UV fluorescence to detect lesions indicative of white-nose syndrome. *J. Wildl. Dis.* **2014**, *50*, doi: http://dx.doi.org/10.7589/2014-03-058

(30) Smoot, M. E.; Ono, K.; Ruscheinski, J.; Wang, P. L.; Ideker, T. Cytoscape 2.8: new features for data integration and network visualization. *Bioinformatics* **2011**, *27*, 431-432.

(31) Watrous, J.; Roach, P.; Alexandrov, T.; Heath, B. S.; Yang, J. Y.; Kersten, R. D.; van der Voort, M.; Pogliano, K.; Gross, H.; Raaijmakers, J. M.; Moore, B. S.; Laskin, J.; Bandeira, N.; Dorrestein, P. C. Mass spectral molecular networking of living microbial colonies. *Proc. Natl. Acad. Sci. USA* **2012**, *109*, E1743-E1752.

(32) Yang, J. Y.; Sanchez, L. M.; Rath, C. M.; Liu, X.; Boudreau, P. D.; Bruns, N.; Glukhov, E.; Wodtke, A.; de Felicio, R.; Fenner, A.; Wong, W. R.; Linington, R. G.; Zhang,

L.; Debonsi, H. M.; Gerwick, W. H.; Dorrestein, P. C. Molecular networking as a dereplication strategy. *J. Nat. Prod.* **2013**, *76*, 1686-1699.

(33) Parrow, N. L.; Fleming, R. E.; Minnick, M. F. Sequestration and scavenging of iron in infection. *Infect. Immun.* **2013**, *81*, 3503-3514.

(34) Theurl, I.; Fritsche, G.; Ludwiczek, S.; Garimorth, K.; Bellmann-Weiler, R.; Weiss. G. The macrophage: a cellular factory at the interphase between iron and immunity for the control of infections. *Biometals.* **2005**, *18*, 359-367.

(35) Miethke, M.; Marahiel, M. A. Siderophore-based iron acquisition and pathogen control. *Microbiol. Mol. Biol. Rev.* **2007**, *71*, 413-451.

(36) Haas, H.; Eisendle, M.; Turgeon, B. G. Siderophores in fungal physiology and virulence. *Annu. Rev. Phytopathol.* **2008**, *46*, 149-187.

(37) Schrettl, M,; Haas, H. Iron homeostasis-Achilles' heel of *Aspergillus fumigatus*? *Curr. Opin. Microbiol.* **2011**, *14*, 400-405.

(38) Miller, M. J.; Zhu, H.; Xu, Y.; Wu, C.; Walz, A. J.; Vergne, A.; Roosenberg, J. M.; Moraski, G.; Minnick, A. A.; McKee-Dolence, J.; Hu, J.; Fennell, K.; Kurt Dolence E.; Dong, L.; Franzblau, S.; Malouin, F.; Möllmann, U. Utilization of microbial iron assimilation processes for the development of new antibiotics and inspiration for the design of new anticancer agents. *Biometals.* **2009**, *22*, 61-75.

(39) Shen, H. Microbial warfare: fighting a bat epidemic with bacteria. *Vimeo, SciCom Slugs, UC Santa Cruz* **2013**, Available: http://vimeo.com/44914276.

Chapter 4 is a modified reprint of the material as it appears in the manuscript prepared to submitted to PLOS ONE 2014 by Samantha J. Mascuch, Wilna J. Moree, Cheng-Chih Hsu, Gregory G. Turner, Tina L. Cheng, David S. Blehert, A. Marm Kilpatrick, Winifred F. Frick, Michael J. Meehan, Lena Gerwick, and Pieter C. Dorrestein. The thesis author is the primary investigator and author of the experimental aspects of this manuscript.

Chapter 5

Future Direction – A Proposal:

Prognostic Molecular Signatures of Cancer Immunotherapy Using Mass Spectrometry Imaging

5.1 Synopsis

The development of monoclonal antibodies for cancer immunotherapy has achieved a considerable success in recent decades. Since the first cancer antibody Rituximab (trade name Rituxan) was released in 1997, more than a dozen of cancer antibodies have been approved by FDA. Science magazine recently selected cancer immunotherapy as the 2013 breakthrough of year.[1] The cancer antibody works like a guided missile: it finds a target cancer cell, and then it boosts your own immune system to destroy the cancer cell. Not like chemotherapy, the rest parts of your body remain healthy. This smart approach looks promising, and it really does. But one thing is missing--what is the chemistry in it that makes it works so efficiently? Or I might rephrase the question this way: can we look on the chemical history of the cells and determined if they are getting better after cancer immunotherapy?

This is what I am trying to work on in the proposed project. Using the advanced mass spectrometry imaging techniques, we are able to measure the shift of chemistry in the normal cells when they turn into cancers. This shift of chemical profiles provides a powerful approach for clinical uses. Now, we are proposing that this chemical shift can be used to cancer diagnosis at therapeutic stages. By measuring the molecular profile directly on the lymphoma tissue sections, and monitoring its changes after treating with rituximab, which targets on an antigen specific to lymphoma, we will be able to find out the most significant molecular patterns that could possibly reflect the disease state and the extent of therapeutic treatments. This chemical information will not only provide a detailed understanding of cellular responses that leads to the collapse of cancer cells, but more importantly could possibly help to the discovery of safer and more effective treatments.

5.2 Abstract

Various kinds of immunotherapeutic agents targeting cancers have been approved by FDA; however, detailed molecular mechanisms on the disruption of cancer phenotypes remain elusive. In this project, we provide an innovative approach incorporating mass spectrometry imaging and statistical analysis to obtain the metabolic and proteomic patterning of cancerous B cells undertaken rituximab (anti-CD20 monoclonal antibody) treatment. We will utilize MYC-Induced transgenic mouse models of lymphoma in which rituximab and its mouse equivalent are administered for this study. Using the advanced mass spectrometry techniques, desorption electrospray ionization mass spectrometry (DESI-MS) imaging and nanospray desorption electrospray ionization

mass spectrometry (NanoDESI-MS), a broad range of endogenous biomolecules in the cells including peptides and proteins, as well as metabolites such as lipids and carbohydrates will be revealed directly on the lymphoma tissue sections. To classify the imaging results, mass spectrometric data will be further processed by statistical analysis using significance analysis of microarrays (SAM) and least absolute shrinkage and selection operator (Lasso) method. The resulting molecular signature enables an alternative pathological evaluation to prognosticate the extent of cancer immunotherapy treatment at therapeutic stage, and will give an insight into the molecular mechanism that underlies the collapse of cancer phenotype via immunotherapy.

5.3 Background and Significance

Cancer immunotherapy provides a highly specific anticancer approach by harnessing patient's immune system to fight against malignant cells.[2] It was recently selected as Science's 2013 breakthrough of the year for its profound potential as a treatment against cancers.[1] Various kinds of immunotherapeutic agents targeting cancer have been approved by the Food and Drug Administration (FDA); however, detailed mechanisms on the disruption of cancer phenotypes remain elusive.[3] For example, rituximab (IDEC-C2B8) is a chimeric monoclonal antibody targeted against antigen CD20, which is highly expressed on the surface of immune system B-cells as well as B-cell lymphomas, and depletes targeted B cells.[4-6] Rituximab are known to potentially trigger programmed cell death and activation of immune cells to mediate antibody-dependent cellular cytotoxicity (ADCC).[7-9] A recent study shows that rituximab causes a polarization of B cells so that its therapeutic ability in triggering ADCC is enhanced.[10]

However, the mechanism of rituximab-mediated B-cell depletion is not yet fully understood, hindering the development of more precise immunotherapeutic approaches such as the prevention of "pan-B-cell" disruption. A large portion of the incompleteness of our knowledge is the lack of molecular and chemical scopes for this process.

A remarkable feature of tumorigenesis at the prognostic stage is the global shift in metabolism.[11-13] However, investigations on how and to what extent does this molecular features divert at the immunotherapeutic stage are to be determined. It is known that the activation of the immune system is intricately linked to the metabolic reprogramming in lymphocytes.[14] A recent study also shows that rituximab resistance is related to altered metabolism.[15] The ability to measure metabolism *in situ* could provide a powerful strategy for the early detection of cancers, and a better way to prognosticate cancers based on the detection of certain molecular signatures related to specific oncogene expression. Furthermore, this ability could also provide an extraordinary tool for the evaluation of effectiveness of cancer treatments, as well as a potential probe to investigate the distinct molecular profile associated to specific cancer treatment and finally could uncover detailed molecular underpinnings of cancer immunology that could serve as a better therapeutic strategy. With the ongoing advances in mass spectrometry (MS) imaging technologies, computational methods, as well as proteomic and metabolic analyses, a more complete understanding of the chemistry that underlies tumorgenesis and mass spectrometry-based cancer diagnosis are now possible.[16-19] In this proposal, we will use mass spectrometry imaging as a tool for identifying molecular signatures associated with rituximab immunotherapy in lymphomas directly on the tissue sections, and decipher the molecular mechanism by which rituximab efficiently depletes cancers.

We hypothesize that rituximab regulates a specific metabolic and proteomic signature that promotes a specific cellular behavior associated with lymphoma depletion. We will determine if the identified distinctive molecular signature is directly caused by rituximab; and evaluate if this can be used for diagnosis and prognostication of lymphoma immunotherapy (**Figure 5.1**). To address this hypothesis, we aim to develop new methodologies that incorporate advanced mass spectrometry techniques, statistical modelings, and pharmacology practices. The mass spectrometry techniques that will be used are: (i) Desorption Electrospray Ionization Mass Spectrometry Imaging (DESI-MSI),[20-22] and (ii) Nanospray desorption electrospray ionization (or NanoDESI) MS.[23,24] These mass spectrometry techniques allow high sensitive *in situ* molecular analysis and characterization directly on biological surfaces. We will utilize *in vivo* tissues of MYC-Induced transgenic mouse models of lymphoma tissues in which rituximab and its mouse equivalent are administered and *in vitro* lymphoma cell lines for mass spectrometry interrogation. Statistical approaches of significance analysis of microarrays (SAM) and least absolute shrinkage and selection operator (Lasso) method will be applied to classify the imaging results and further used to prognosticate the disease states at therapeutic stage.

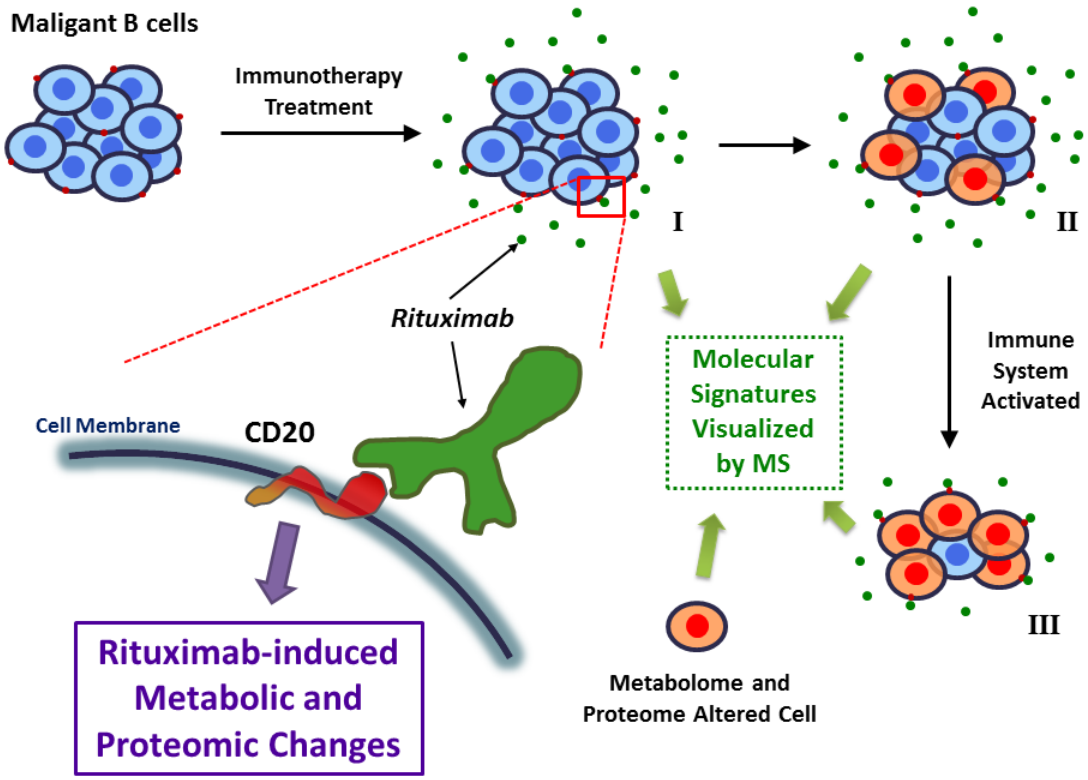

Figure 5.1 Outline of the hypothesized model for rituximab-triggered molecular shift in lymphomas. Rituximab binds to CD20, which is widely expressed on the surfaces of malignant B cells (lymphomas), and activate the immune response of the host to destroy rituximab-attached B cells. Anti-CD20 rituximab may possibly change the cell state through the regulation on some particular metabolites and proteins of B cells. After rituximab is administered, the molecular profiles of lymphomas start to evolve. Mass spectrometry analysis will be implemented at different therapeutic stages (I, II, and III) to obtain the prognostic molecular signatures of lymphomas.

5.4 Specific Aims

In order to determine where the extent lymphoma immunotherapy can be accessed, as well as to gain more mechanistic understanding of rituximab-induced immune response, we seek to develop imaging mass spectrometry-based approaches for *in situ* metabolic and proteomic profiling directly on tissue sections. Toward this end, we

will observe molecular signatures of MYC-induced lymphomas before and during immunotherapeutic treatment. Three specific aims are delineated as follows:

Aim 1: Define the molecular signatures in MYC-Induced lymphomas. The ability to identify molecular signatures strictly related to the expression of MYC oncogene and the prognostic value for lymphomas will be investigated in specific Aim 1. Our approach involved generating transgenic mice in which we can conditionally express MYC cDNA and as models for lymphomas. Advanced mass spectrometry techniques, including DESI and NanoDESI, will be used to image the biological samples and investigate the changes in molecular profiles that occur in MYC-Induced cancer, in comparison to control samples in which MYC is observed at low expression levels.

1a. Determine the metabolic and proteomic signatures directly from tissue sections. Sequential MYC-ON mouse sections will be collected and introduced to different ionization sources, including DESI and NanoDESI to evaluate the performances of each technique.

1b. Compare the molecular signatures of MYC-ON and MYC-OFF tissue sections that have different lymphoma phenotypes. Wild-type, MYC activated for 2 months (MYC ON/2), and MYC activated for 2 months and then deactivated for 1 months (MYC ON/2-OFF/1) lymphomas sections as well as healthy lymph nodes will be collected and analyzed by the mass spectrometry techniques in Aim 1a.

Aim 2: Determine if a prognostic molecular signature in lymphomas is specifically associated with immunotherapy using IDEC-C2B8 (Chimeric mouse/human monoclonal anti-CD20 antibody) **and IDEC-2B8** (murine monoclonal anti-CD20

antibody). The ability to identify molecular signature associated with administration of rituximab (IDEC-C2B8, ADCC inactive in mouse model) and rituximab mouse equivalent (IDEC-2B8, ADCC active in mouse model) on MYC-induced lymphomas will be evaluate in specific Aim 2. Imaging mass spectrometry techniques, which performance are evaluated in Aim 1, will be used to obtain the metabolic and proteomic signatures. SAM and Lasso method will be applied to classify the imaging results.

2a. Obtain the molecular signatures of post-immunotherapy lymphomas in a timely basis. Lymphomas of 0, 0.2, 1, 5, 30, 60 days after administration of anti-CD20 antibodies will be collected and perform mass spectrometry imaging.

2b. Develop the dynamical molecular profiles of post-immunotherapy lymphomas. Data from 2a will be analyzed using statistical analysis (SAM and Lasso method) to classify tissues as cancerous or healthy based on the molecular information obtain from the tissues. The processed data of mass-spectral features will be compared with pathologic evaluation to determine the indicative molecular features of disease at therapeutic states.

Aim 3: Determine if immunotherapeutic treatment regulates cellular metabolisms and protein expressions to disrupt cancer phenotype. Based on the MSI and statistical results from Aim 1 and Aim 2, molecules of interest will be characterized using *in situ* top-down tandem mass analysis. Cell lines isolated from MYC-induced lymphoma models will be subject to rituximab and harvested at multiple time points. Endogenous metabolites and proteins of cell samples and tissue will be identify and characterized with high resolution mass spectrometer. In Aim 3 we will determine the causal connection

between anti-CD20 monoclonal antibodies and expression of specific metabolites and proteins in lymphoma models.

3a. Identify key molecules that is significantly associated with immunotherapy. Tandem mass analysis will be performed directly on the lymphoma tissues and cell cultures using the mass spectrometry ionization methods in Aim 1 and 2. To resolve isotopic isoforms of large compounds, high spectral resolution mass spectrometry analyzer (LTQ-Orbitrap XL, Thermo Scientific) will be used. This will incorporate database (METLIN, LIPID MAPS, PDB, etc.) searching.

3b. Determine if generation or breakdown of metabolic and proteomic profiles are specific to immunotherapy. By quantitative mass spectral comparison between samples at different stages, we will be able to determine the global shift of molecular signatures as well as regulation of specific compounds in the cancer cell under immunotherapy.

5.5 Research Strategies

The overall goal of this proposal is to identify molecular signatures, including metabolites and proteins, which are indicative to the immunotherapy treatment of anti-CD20 monoclonal antibodies to lymphomas. There are three key steps in this project. Firstly, transgenic mice model of MYC-induced lymphomas will be analyzed by DESI and NanoDESI for mass spectrometric investigation. Molecular signatures of lymphomas and the capability of each technique will be obtained and evaluated. Secondly, lymphoma tissues will be collected and exercised with imaging mass spectrometry over multiple time points relative to anti-CD20 monoclonal antibodies treatment. Thirdly, with the aid

of temporal information revealed in step 2 and statistical analysis, molecules of interest will be correlated to disease states and extends of immunotherapy on the basis of pathological diagnosis. Identification of candidate key compounds will allow subsequent rituximab-triggered molecular model with finer details.

5.5.1 Mass Spectrometry Imaging Methods

DESI-MS Imaging

DESI is one of a recently developed group of ambient ionization techniques in mass spectrometry in which samples are examined at the ambient environment with minimal pretreatment.[20] DESI imaging has the outstanding capability of providing spatial information on the distribution of a multitude of molecules from a tissue section with the specificity and the sensitivity that are characteristic of MS analysis.[21,22] DESI imaging has been especially useful in the analysis of small molecules, such as metabolites and lipids from different biological samples.[21,22] The tissue section experiments involve spraying a stream of charged solvent onto the tissue allowing chemicals to be lifted from the tissue surface and transferred into a mass spectrometer, where the mass-to-charge ratios (*m/z* values) of the molecular ions are measured and species are identified based high mass accuracy measurements and tandem mass spectrometry. The experiment takes less than a second per pixel and gives a large amount of information on the tissue (**Figure 5.2**). DESI-MS allows the characterization and imaging of many lipids including fatty acyls, prostaglandins, glycerol-phospholipids, and sphingolipids, and small molecules involved in energy metabolism. DESI-MSI has useful applications to cancer diagnosis, and been used to evaluate the chemical composition of human kidney,[29] bladder,[30]

prostate[31] and brain[18] cancerous tissues. In a pilot study, Zare laboratory applied DESI-MS imaging to provide an *in situ* lipidomic profile from a MYC-induced hepatocellular carcinoma.[16]

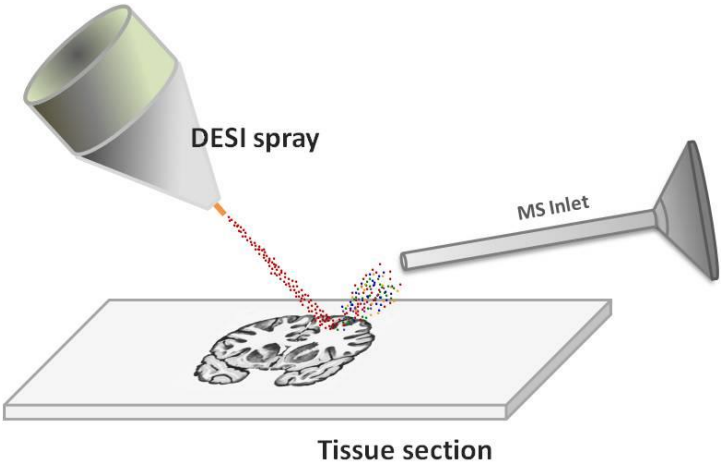

Figure 5.2 DESI-MS Imaging Setup. The DESI-MSI spray delivers a continuous stream of charged droplets, which impact the sample surface. The primary droplets impact the tissue section and form a layer of solvent that extract the molecules from the tissue, such as metabolites and lipids. The splash of secondary solvent microdroplets containing the dissolved molecules is captured by the mass spectrometer inlet. Mass analysis is performed and a mass spectrum is obtained. The sample surface continuously moves so that the process described occurs for each pixel, and a 2D chemical map of the tissue section can be made. This process, which occurs in less than one second per pixel, is performed in open air and ambient conditions, without requiring additional sample preparation.

NanoDESI-MS Imaging

NanoDESI is the improved version of DESI, which replaces the primary stream of microdroplets into a micrometer-size fused silica capillary tube with continuous solvent flow. Another capillary tube is used to pick up the analytes from the tissue surface via the microextraction by a tiny liquid junction sustained on the tissue surface between the two capillary tubes.[32] NanoDESI-MS imaging has applied to various kinds of biological samples as an imaging tool for lipids, small metabolites and drug metabolism.[23,32,33] As the splash of secondary solvent microdroplets in DESI is substituted with a capillary tube

analyte carrier in NanoDESI, the sensitivity of NanoDESI is greatly improved. The work led by the applicant (Hsu, C-C et al.) demonstrates that proteins associated with embryogenesis can be visualized by NanoDESI-MS.[24] As the microextration spot of is visible, NanoDESI can be integrated with a light microscope for a better targeted MS analysis (**Figure 5.3**).

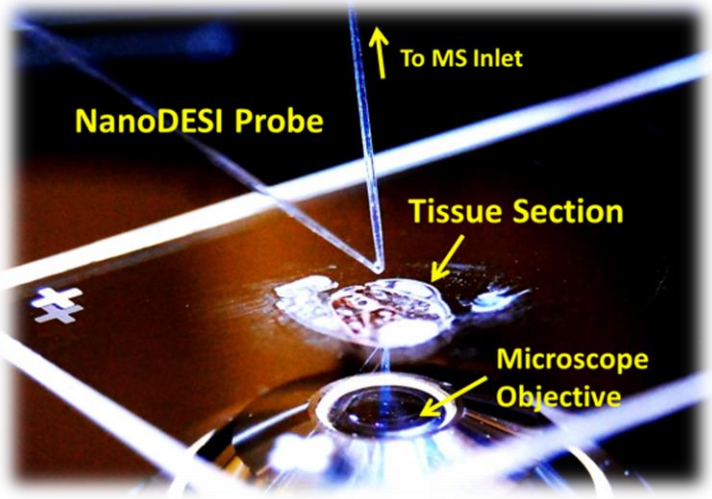

Figure 5.3 NanoDESI-MS Setup. Solvent was delivered by a syringe pump (not shown) through the primary capillary tube (left) in which the terminal end joint with the secondary capillary (right). The analytes are desorbed from the sample surface at the liquid bridge and transferred into the self-aspirating secondary capillary tube. A continuous stream of electrospray occurs at the end of secondary capillary and the subsequent ions are captured and then transferred into MS inlet. An inverted light microscope is interfaced with NanoDESI to improve targeted molecular characterization.

5.5.2 Biostatistical Methods

Significance analysis of microarrays (SAM) is a statistical technique using measurements from DNA microarrays, which estimate the expression of thousands of genes in a single experiment.[26,27] SAM determines whether changes in gene expression are statistically significant between different phenotypes or experimental conditions.

Similarly, in DESI-MS imaging data, hundreds of molecules in a single imaging experiment are detected. As the data generated is very large and complex, a method for sorting out what is significant and what is not is essential for defining molecular signatures. For DESI-MS imaging data, SAM identifies statistically significant molecules by computing a T statistic (score) "dj" for each molecule "j" that measures the average change in the peak height for that molecule between different phenotypes. Repeated permutations of the data are used to determine if the expression of any molecule is significantly related to a phenotype.

Now, we will develop this method to identify which molecules contribute to anti-CD20 monoclonal antibody treatment-specific molecular signatures in lymphomas. This will be the first time that SAM is used to treat the complex metabolic data obtained using mass spectrometry imaging. However, SAM is not able to generate a predictive model, or a classifier. Thus, by using the Lasso Method, we can perform logistic regression using an absolute value penalty to estimate parsimonious sets of features for discriminating between different outcome classes.[28] This approach has been applied to gastric cancer diagnosis using DESI-MS imaging.[17] Thereby, we will be able to define the classes of lymphomas that are at different time points in therapeutic stages under rituximab treatment. This work will develop novel methods for mass spectrometry Imaging and metabolomic/proteomic data analysis.

5.5.3 Approaches and Preliminary Results

Aim 1. Define the molecular signatures in MYC-Induced lymphomas. Within this aim, we will collect mouse models of lymphomas that are MYC-ON and MYC-OFF.

The lymphoma tissues will be cryosectioned and introduced to MS imaging on both positive and negative modes in the range *m/z* 100-1500 without other pretreatments. The preliminary results by DESI-MS imaging show a very informative molecular signature at *m/z* 700-900 that were putatively assigned as lipids.

Aim 2: Determine if a prognostic molecular signature in lymphomas is specifically associated with immunotherapy using IDEC-C2B8 and IDEC-2B8. From the same MYC-induced mouse models of lymphomas in Aim 1 we will administer IDEC-C2B8 (rituximab) and IDEC-2B8. IDEC-2B8 has high effect on cancer cell depletion in mouse model due to the activation of the immune system, thus we expect to observe different phenotypes of it than rituximab treated models. MS imaging at multiple time points will be obtained. Cell lines isolated from MYC-induced lymphoma models will be cultured and treated with rituximab. Monolayer cell culture will be investigated by MS analysis (**Figure 5.4**), in which molecular signatures will be compared with tissue sections.

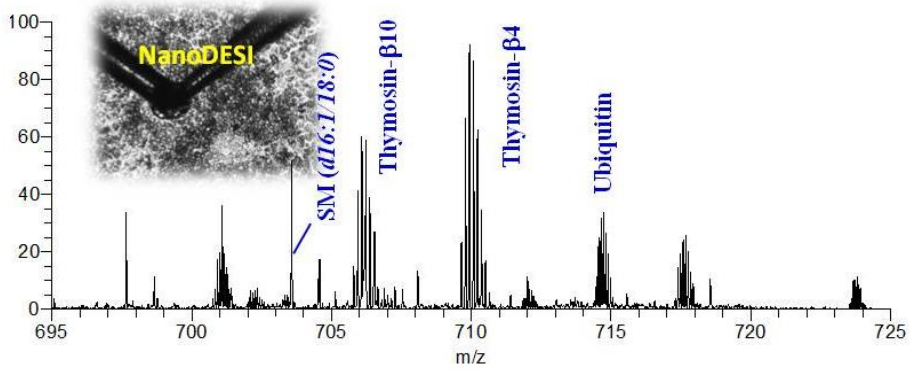

Figure 5.4 NanoDESI mass spectra acquired directly on a monolayer cell line culture. Proteins and lipids are observed in the given *m/z* range. *Inset*: microscopic photograph of NanoDESI on the cell culture surface. *****The contents in Figure 5 are for conceptual demonstrations, not the results of the proposed experiments.

Aim 3: Determine if immunotherapeutic treatment regulates cellular metabolisms and protein expressions to disrupt cancer phenotype. In this aim, we will adopt an innovative approach that connects the molecular signatures, by which statistical significances are determined by SAM, to chemical features of the molecule of interest, as revealed from MS/MS (tandem mass spectrometry) and high mass accuracy ($\Delta m/z$ < 1 ppm). For example, the MS/MS fragmentation patterns of peptides reveal fragments that correspond to the loss of specific amino acids, while MS/MS of compounds containing sugars typically give losses of 164 or 178 Da; and the loss of phosphate typically results in a loss of 80 Da, whereas phospholipids give phosphorylcholine loss of 59 and 183 Da. To identify if the changes in molecular expression were statistically significant between different sample sets, we will applied SAM to the set of mass spectral data. Results the hundreds of ions found will be displayed as box plots in **Figure 5.5** and then analyzed by Lasso.

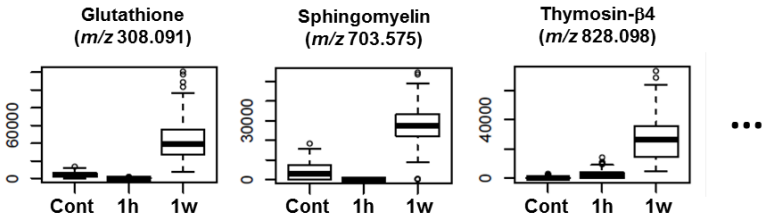

Figure 5.5 SAM identifies specific metabolite and protein species which are expressed differentially in lymphomas treated with anti-CD20 antibody for various periods of time.

5.6 Perspective

From the preliminary data and previously published results, it is clear that the innovative strategy incorporating both ambient mass spectrometry imaging and statistical analysis will provide prognostic insight into the molecular mechanisms of cancer

immunotherapy. Currently, no other study is underway aiming to address the post-immunotherapeutic molecular perturbation in cancer cells. This insight will lead to the identification of previously unknown regulatory pathways that play important roles to maintain or disrupt cancer phenotypes. While this project focus on anti-CD20 antibodies deployed against lymphomas, similar approaches could be implemented to investigate other types of cancer. We believe that using lymphoma immunotherapy as the starting point many more other immunoreaction of cancers will be studied. The establishment of pathological knowledge of cancer immunotherapy at molecular level will not only provide a detailed understanding of cellular responses that leads to the collapse of cancer cells, but more importantly will help to the discovery of safer and more effective treatments.

5.7 References

(1) Couzin-Frankel, J. Cancer immunotherapy. *Science* **2013**, *342*, 1432-1433.

(2) Vanneman, M.; Dranoff, G. Combining immunotherapy and targeted therapies in cancer treatment. *Nat. Rev. Cancer* **2012**, *12*, 237-251.

(3) Scott, A. M.; Wolchok, J. D.; Old, L. J. Antibody therapy of cancer. *Nat. Rev. Cancer* **2012**, *12*, 278-287.

(4) Reff, M. E.; Carner, K.; Chambers, K. S.; Chinn, P. C.; Leonard, J. E.; Raab, R.; Newman, R. A.; Hanna, N.; Anderson, D. R. Depletion of B cells in vivo by a chimeric mouse human monoclonal antibody to CD20. *Blood* **1994**, *83*, 435-445.

(5) Maloney, D. G.; Grillo-López, A. J.; White, C. A.; Bodkin, D.; Schilder, R. J.; Neidhart, J. A.; Janakiraman, N.; Foon, K. A.; Liles, T. M.; Dallaire, B. K.; Wey, K.; Royston, I.; Davis, T.; Levy, R. IDEC-C2B8 (Rituximab) anti-CD20 monoclonal antibody therapy in patients with relapsed low-grade non-Hodgkin's lymphoma. *Blood* **1997**, *90*, 2188-2195.

(6) Keating, G. M. Rituximab: a review of its use in chronic lymphocytic Leukaemia, low-grade or follicular lymphoma and diffuse large B-cell lymphoma. *Drugs* **2010**, *70*, 1445-1476.

(7) Mathas, S.; Rickers, A.; Bommert, K.; Dörken, B.; Mapara, M. Y. Anti-CD20- and B-cell receptor-mediated apoptosis: evidence for shared intracellular signaling pathways. *Cancer Res.* **2000**, *60*, 7170-7176.

(8) Clynes, R. A.; Towers, T. L.; Presta, L. G.; Ravetch, J. V. Inhibitory Fc receptors modulate *in vivo* cytotoxicity against tumor targets. *Nat. Med.* **2000**, *6*, 443-446.

(9) Cartron, G.; Dacheux, L.; Salles, G.; Solal-Celigny, P.; Bardos, P.; Colombat, P.; Watier, H. Therapeutic activity of humanized anti-CD20 monoclonal antibody and polymorphism in IgG Fc receptor FcgammaRIIIa gene. *Blood* **2002**, *99*, 754-758.

(10) Rudnicka, D.; Oszmiana, A.; Finch, D. K.; Strickland, I.; Schofield, D. J.; Lowe, D. C.; Sleeman, M. A.; Davis, D. M. Rituximab causes a polarisation of B cells which augments its therapeutic function in NK cell-mediated antibody-dependent cellular cytotoxicity. *Blood* **2013**, *121*, 4694-4702.

(11) Soga, T. Cancer metabolism: key players in metabolic reprogramming. *Cancer science* **2013**, *104*, 275-281.

(12) Ward, P. S.; Thompson, C. B. Metabolic reprogramming: a cancer hallmark even Warburg did not anticipate. *Cancer cell* **2012**, *21*, 297-308.

(13) Wu, W.; Zhao, S. Metabolic changes in cancer: beyond the Warburg effect. *Acta biochimica et biophysica Sinica* **2013**, *45*, 18-26.

(14) Pearce, E. L.; Poffenberger, M. C.; Chang, C.-H.; Jones, R. G. Fueling immunity: insights into metabolism and lymphocyte function. *Science* **2013**, *342*, 1242454.

(15) Gu, J.; Yanamadala, V.; Mavis, C.; Hernandez, F.; Czuczman, M. S. Altered glucose metabolism in Rituximab-chemotherapy resistant cells is a potential target for future therapeutic development." *Blood* **2013**, *112*, 4413.

(16) Perry, R. H.; Bellovin, D. I.; Shroff, E. H.; Ismail, A. I.; Zabuawala, T.; Felsher, D. W.; Zare, R. N. Characterization of MYC-induced tumorigenesis by in situ lipid profiling. *Anal. Chem.* **2013**, *85*, 4259-4262.

(17) Eberlin, L. S.; Tibshirani, R. J.; Zhang, J.; Longacre, T. A.; Berry, G. J.; Bingham, D. B.; Norton, J. A.; Zare, R. N.; Poultsides, G. A. Molecular assessment of surgical-resection margins of gastric cancer by mass-spectrometric imaging. *Proc. Natl. Acad. Sci. USA* **2014**, *111*, 2436-2441.

(18) Eberlin, L. S.; Norton, I.; Orringer, D.; Dunn, I. F.; Liu, X.; Ide, J. L.; Jarmusch, A. K.; Ligon, K. L.; Jolesz, F. A.; Golby, A. J.; Santagata, S.; Agar, N. Y. R.; Cooks R. G. Ambient mass spectrometry for the intraoperative molecular diagnosis of human brain tumors. *Proc. Natl. Acad. Sci. USA* **2013**, *110*, 1611-1616.

(19) Veselkov, K. A.; Mirnezami, R.; Strittmatter, N.; Goldin, R. D.; Kinross, J.; Speller, A. V. M.; Abramov, T.; Jones, E. A.; Darzi, A.; Holmes, E.; Nicholson, J. K.; Takats, Z. Chemo-informatic strategy for imaging mass spectrometry-based hyperspectral profiling of lipid signatures in colorectal cancer. *Proc. Natl. Acad. Sci. USA* **2014**, *111*, 1216-1221.

(20) Takats, Z.; Wiseman, J. M.; Gologan, B.; Cooks, R. G. Mass spectrometry sampling under ambient conditions with desorption electrospray ionization. *Science* **2004**, *306*, 471-473.

(21) Wiseman, J. M.; Ifa, D. R.; Song, Q.; Cooks, R. G. Tissue imaging at atmospheric pressure using desorption electrospray ionization (DESI) mass spectrometry. *Angew. Chem. Int. Ed.* **2006**, *45*, 7188-7192.

(22) Wiseman, J. M.; Ifa, D. R.; Zhu, Y.; Kissinger, C. B.; Manicke, N. E.; Kissinger, P. T.; Cooks, R. G. Desorption electrospray ionization mass spectrometry: imaging drugs and metabolites in tissues. *Proc. Natl. Acad. Sci. USA* **2008**, *105*, 18120-18125.

(23) Lanekoff, I.; Burnum-Johnson, K.; Thomas, M.; Short, J.; Carson, J. P.; Cha, J.; Dey, S. K.; Yang, P.; Conaway, M. C. P.; Laskin, J. High-speed tandem mass spectrometric in situ imaging by nanospray desorption electrospray ionization mass spectrometry. *Anal. Chem.* **2013**, *85*, 9596-9603.

(24) Hsu, C.-C.; White, N. M.; Hayashi, M.; Lin, E. C.; Poon, T.; Banerjee, I.; Chen, J.; Pfaff, S. L.; Macagno, E. R.; Dorrestein, P. C. Microscopy ambient ionization top-down mass spectrometry reveals developmental patterning. *Proc. Natl. Acad. Sci. USA* **2013**, *110*, 14855-14860.

(25) Felsher, D. W.; Bishop, J. M. Reversible tumorigenesis by MYC in hematopoietic lineages. *Molecular Cell.* **1999**, *4*, 199-207.

(26) Tusher, V. G.; Tibshirani, R.; Chu, G. Significance analysis of microarrays applied to the ionizing radiation response. *Proc. Natl. Acad. Sci. USA* **2001**, *98*, 5116-5121.

(27) Tibshirani, R.; Hastie, T.; Narasimhan, B.; Chu, G. Diagnosis of multiple cancer types by shrunken centroids of gene expression. *Proc. Natl. Acad. Sci. USA* **2002**, *99*, 656765-72.

(28) Tibshirani, R. Regression shrinkage and selection via the Lasso. *J R. Statist. Soc. B.* **1996**, *58*, 267-288.

(29) Dill, A. L.; Eberlin, L. S.; Zheng, C.; Costa, A. B.; Ifa, D. R.; Cheng, L. A; Masterson, T. A.; Koch, M. O.; Vitek, O.; Cooks, R. G. Multivariate statistical differentiation of renal

cell carcinomas based on lipidomic analysis by ambient ionization imaging mass spectrometry. *Anal Chem*. **2010**, *398*, 2969-78.

(30) Dill, A.; Eberlin, L. S.; Costa, A. B.; Zheng, C.; Ifa, D. R.; Cheng, L.; Masterson, T. A.; Koch, M. O.; Vitek, O.; Cooks, R. G. Multivariate statistical identification of human bladder carcinomas using ambient ionization imaging mass spectrometry. *Chem.-A Eur. J.* **2011**, *17*, 2897-2902.

(31) Eberlin, L. S.; Dill, A. L.; Costa, A. B.; Ifa, D. R.; Cheng, L.; Masterson, T.; Koch, M.; Ratliff, T. L.; Cooks, R. G. Cholesterol sulfate imaging in human prostate cancer tissue by desorption electrospray ionization mass spectrometry. *Anal. Chem.* **2010**, *82*, 3430-3434.

(32) Roach, P. J.; Laskin, J.; Laskin, A. Nanospray desorption electrospray ionization. An ambient method for liquid-extraction surface sampling in mass spectrometry. *Analyst* **2010**, *135*, 2233-2236.

(33) Lanekoff, I.; Thomas, M.; Carson, J. P.; Smith, J. N.; Timchalk, C.; Laskin, J. Imaging nicotine in rat brain tissue by use of nanospray desorption electrospray ionization mass spectrometry. *Anal. Chem.* **2013**, *85*, 882-889.